Faraday Discussions

Cite this: DOI: 10.1039/c9fd00148d

PAPER

The micromechanical model to computationally investigate cooperative and correlated phenomena in metal–organic frameworks†

Sven M. J. Rogge *

Received 30th December 2019, Accepted 15th January 2020
DOI: 10.1039/c9fd00148d

Computational insight into the impact of cooperative phenomena and correlated spatial disorder on the macroscopic behaviour of metal–organic frameworks (MOFs) is essential in order to consciously engineer these phenomena for targeted applications. However, the spatial extent of these effects, ranging over hundreds of nanometres, limits the applicability of current state-of-the-art computational tools in this field. To obtain a fundamental understanding of these long-range effects, the micromechanical model is introduced here. This model overcomes the challenges associated with conventional coarse-graining techniques by exploiting the natural partitioning of a MOF material into unit cells. By adopting the elastic deformation energy as the central quantity, the micromechanical model hierarchically builds on experimentally accessible input parameters that are obtained from atomistic quantum mechanical or force field simulations. As a result, the here derived micromechanical equations of motion can be adopted to shed light on the effect of long-range cooperative phenomena and correlated spatial disorder on the performance of mesoscale MOF materials.

1 Introduction

Thanks to the peculiar and highly porous structures of metal–organic frameworks (MOFs),[1–3] composed of organic and inorganic building blocks,[4] these materials often exhibit 'anomalous' and highly cooperative responses to external stimuli.[5] These peculiar phenomena, such as negative gas adsorption,[6] exceptionally high elastic anisotropy,[7] or even the emergence of multiple metastable phases and large-amplitude structural flexibility,[8–10] arise from the large diversity of interaction strengths in MOFs.[11] Computational research provides an essential tool to understand how these fundamental interactions at the atomic scale, varying from

Center for Molecular Modeling, Ghent University, Technologiepark 46, Zwijnaarde, 9052, Belgium. E-mail: Sven.Rogge@UGent.be

† Electronic supplementary information (ESI) available: Derivation of the micromechanical equations of motion for unistable and bistable nanocells. See DOI: 10.1039/c9fd00148d

strong covalent bonds to weaker coordination bonds to weak but long-range dispersion interactions, ultimately combine to result in the observed macroscopic behaviour of MOFs.[12,13] Two competing ingredients are essential to accurately model the macroscopic behaviour of these materials.[14] On the one hand, the adopted model needs to capture the diversity of interactions that give rise to the MOF's macroscopic response to external stimuli. On the other hand, the adopted model should also be able to cover sufficiently large regions of the MOF material, so that possible cooperative behaviour can be adequately represented. For instance, to shed light on the experimental observation that flexible MOFs tend to become more rigid upon decreasing the crystallite size to the submicrometre regime,[15–20] computer models need to capture the long-range phenomena that occur on length scales on the order of the crystal size.

In this respect, quantum mechanical methods are most accurate but are often too computationally expensive to dynamically simulate MOF systems larger than a few nanometres.[21,22] By approximating the atomic interactions by analytical functions, system-specific force fields can dynamically model much larger systems at the expense of a reduction in accuracy.[23–26] Recently, MOF models with dimensions of up to 10–20 nm and containing up to a few tens of thousands of atoms were investigated using these force fields, revealing that flexible MOFs can exhibit phase coexistence under external stimuli.[27,28] This phase coexistence, a type of correlated spatial disorder in which multiple (meta)stable phases coexist in the material at the same time, provides a possible explanation for the experimentally observed size effect as it decreases the barrier for the switchable behaviour of flexible MOFs, but can only be observed when considering sufficiently large models.[28] However, even system-specific force fields, either at the atomic or the coarse-grained level,[29] are unable to directly model systems at length scales corresponding to the experimental crystal size and investigate cooperative phenomena that extend over the whole crystal. Therefore, the micromechanical model is introduced in this article as a hierarchical coarse-grained model that goes beyond system-specific force fields to capture these long-range cooperative effects while still approximating sufficiently well the variety of interactions present in MOFs.

The need for computational models capable of describing larger MOF structures is not only inspired by the aim to understand their cooperative macroscopic responses to external stimuli. In recent years, awareness has grown that MOFs are not the perfectly crystalline materials once envisioned, but that they exhibit inherent spatial disorder that strongly impacts their macroscopic behaviour. As indicated in Fig. 1, inherent spatial disorder in MOFs may be classified according to its spatial extent, ranging from short-range isolated disorder up to a few nanometres, to mid-range correlated disorder up to a few tens of nanometres, to long-range correlated disorder on even larger length scales and involving up to several millions of atoms. The most prominent examples of short-range disorder in MOFs are point defects, such as the linker and node vacancies in UiO-66 and HKUST-1,[30–33] shown in Fig. 1(a), and the under-coordinated metal sites in MIL-53(Al,V).[34] In larger concentrations, these defects are observed to conglomerate into correlated nanoregions, such as in UiO-66,[32,35] or to form mesopores, as in HKUST-1,[36,37] giving rise to mid-range spatial disorder extending over several nanometres (Fig. 1(b)). Finally, MOFs may also exhibit long-range correlated disorder, in which large parts of the crystal cooperatively undergo phase

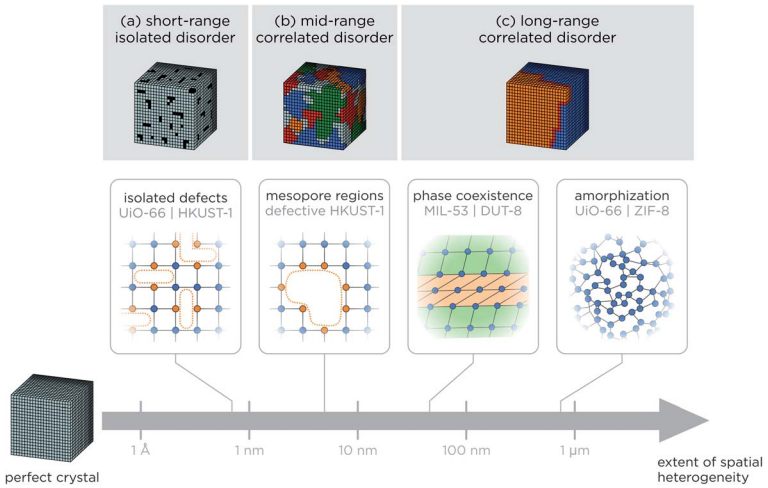

Fig. 1 Classification of the different types of spatial disorder observed in MOFs and related materials, varying from (a) short-range isolated disorder (< *ca.* 1 nm), to (b) mid-range correlated disorder (*ca.* 1–20 nm), to (c) long-range correlated disorder (> *ca.* 20 nm) with selected examples for each of the different types of spatial disorder.

transitions between different metastable phases, potentially giving rise to phase coexistence (Fig. 1(c)).[27,28] These transitions may be triggered not only between two crystalline phases, such as for MIL-53 or DUT-8,[38,39] but also from a crystalline to an amorphous phase. The latter phenomenon, termed amorphization, has been observed in UiO-66 and various zeolitic imidazolate frameworks (ZIFs),[40,41] among others, and results in the formation of amorphous MOFs (aMOFs) or liquid MOFs that retain the connectivity of the parent material while exhibiting strongly altered properties.[42–44]

As spatial disorder profoundly affects the MOF's macroscopic behaviour, the intentional creation of defects—so-called defect engineering—has emerged as a promising concept to synthesise spatially disordered MOFs with improved performance in, *e.g.*, heterogeneous catalysis and gas adsorption.[22,45–47] Although defect engineering mainly focuses on the targeted creation of isolated defects, correlated spatial disorder has an even vaster potential to revolutionise the design of MOFs as functional devices.[48] However, a fundamental understanding of the impact of correlated spatial disorder on the performance of MOFs requires computational techniques that can model these spatially extended systems with sizes of up to a few hundreds of nanometres.[14]

To investigate these mid- and long-range cooperative phenomena that fall beyond the reach of current computational models, the micromechanical model is introduced in this work. By combining a substantial reduction in the degrees of freedom of the MOF material with specific interaction terms that capture the MOF's flexibility, this model enables the direct simulation of long-range cooperative effects and correlated spatial disorder. As the micromechanical model builds on experimentally verifiable quantities that can be extracted from system-specific force fields or *ab initio* data, it can be adopted as an integrated and hierarchical approach connecting higher-level simulations with experiments. As

ART ■ C9FD00148D

a result, the here introduced micromechanical model forms a computational framework to shed light on the various cooperative phenomena taking place in MOFs, spanning the different length scales from the sub-nanometre to the micrometre regime.

2 The micromechanical concept

While coarse-graining techniques have already been used extensively for biomolecular and polymer systems,[49–51] specific challenges arise when trying to adopt these techniques for periodic network materials such as MOFs.[29,52] Section 2.1 outlines how these traditional techniques pose non-trivial limitations for the coarse-grained description of MOFs, leading to the formulation of the micromechanical model. Similar to conventional coarse-graining procedures, the computational speed-up of the micromechanical model is achieved by reducing the number of interaction beads on the one hand and approximating the interactions between these beads by relatively simple analytical functions on the other hand. As shown schematically in Fig. 2, the micromechanical model consists of three steps. The first step consists of mapping the atomistic representation of the MOF on a suitable coarse-grained representation that exploits the natural partitioning of the material in similar unit cells, as outlined in Section 2.2. In the second step, atomistic simulations are performed, either at the *ab initio* or the force field level, to parametrise the coarse-grained interactions. Finally, in the third step, the coarse-grained material is propagated in time using the equations of motion derived in Sections 2.3 and 2.4 for systems that can be described by a single phase, *e.g.*, to derive the properties near equilibrium, and for systems that exhibit multiple phases, respectively.

2.1 Challenges in coarse-graining MOFs

Martini-like coarse-graining approaches, in which up to four non-hydrogen atoms are collected into a single bead, are traditionally adopted when coarse-graining biomolecules or polymer systems.[53] While this procedure has proven effective for isolated systems and has been used to coarse-grain guests in MOFs, it is not

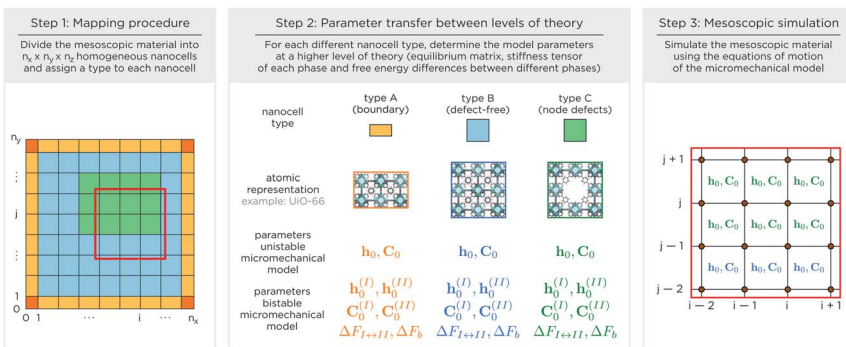

Fig. 2 The three steps in the micromechanical model, illustrated for UiO-66 containing nodal defect regions (green), defect-free regions (blue) and surface regions (orange). Step 3 shows a close-up of the model for the region defined by the red rectangle in step 1.

ART ■ C9FD00148D

straightforward to extend this approach to the MOF network itself. Specifically, four challenges may be identified when trying to construct a Martini-like coarse-graining mapping procedure for extended network materials such as MOFs.

The first challenge results from the often highly symmetric organic and inorganic building blocks of MOFs, which restrict the freedom in symmetry-preserving coarse-grained mapping procedures. For instance, consider the $Zr_6(\mu_3\text{-}OH)_4(\mu_3\text{-}O)_4$ inorganic node present in the hydroxylated form of UiO-66(Zr),[56] visualised in the inset of Fig. 3. When neglecting the highly disordered hydrogen atoms in the node, this building block satisfies the octahedral O_h point group containing 48 symmetry elements. Collecting the atoms of this node into coarse-grained beads necessarily reduces this symmetry or requires atoms to be present in multiple beads, which would lead to inconsistent momentum distributions in the atomistic and coarse-grained representations.[57] The only trivial exceptions are those in which each atom defines its own bead or in which the bead contains the complete inorganic node. A similar observation holds when coarse-graining the phenyl moieties of the organic ligands. As a result, the four-to-one mapping in Martini-like coarse-graining is often not attainable for MOFs. Instead, in the first coarse-grained MOF force field developed by Dürholt *et al.* for HKUST-1,[29,55] a reduction in degrees of freedom of about one order of magnitude was proposed by replacing each of the inorganic nodes and organic ligands by one bead, corresponding to the topology of the material.

The second challenge arises when considering MOFs in which the building blocks are not isolated moieties but rather extend along chains, such as the $[Al(\mu_2\text{-}OH)]_n$ chain of MIL-53(Al) (see inset of Fig. 3).[54] In such a case, it is non-trivial to partition the atoms into coarse-grained beads. In MIL-53(Al), for instance, the μ_2-OH group is connected to two equivalent aluminium atoms. As a result, when assigning this hydroxyl group to either one of the neighbouring aluminium atoms, the symmetry would be reduced, similar to the first challenge for highly symmetric nodes such as in UiO-66. However, while this could be circumvented in UiO-66 by considering the whole node as a single bead, this is not possible for MIL-53(Al) as the bead would have to extend along the whole $[Al(\mu_2\text{-}OH)]_n$ chain.

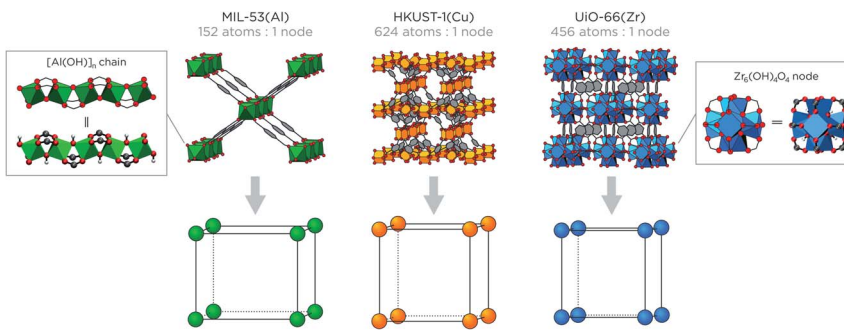

Fig. 3 The micromechanical procedure to map the atomistic model onto the nanocells for three representative MOFs, MIL-53(Al),[54] HKUST-1(Cu),[55] and UiO-66(Zr),[56] with the corresponding reduction in the number of degrees of freedom. Insets show the atomistic representations of the inorganic moieties in MIL-53(Al) (left) and UiO-66(Zr) (right). Colour code: zirconium (blue), copper (orange), aluminium (green), oxygen (red), carbon (grey) and hydrogen (white). Hydrogen atoms are omitted from the periodic materials for clarity.

The third challenge is rooted in the different types of spatial disorder present in MOFs. As spatial disorder results in regions of the material that are similar but not identical, it limits the transferability of traditional mapping procedures. For instance, UiO-66 is prone to linker and node defects, affecting the coordination of the inorganic nodes that remain in the material.[30–32,35] Even when considering minimally defective UiO-66 MOFs, with an average node coordination number of eleven, and assuming no capping molecules are present to replace the missing ligands, up to seven different inorganic nodes that give rise to this average coordination number can be constructed.[58] While these nodes all contain six zirconium atoms, their direct atomistic environments differ. Despite the chemical similarity between these nodes, coarse-grained mapping procedures that define *a priori* how many atoms should be collected in coarse-grained beads would give rise to distinct mappings. Even when the mapping procedure would allow for flexibility in the number of atoms per bead, the interactions between these beads would need to be defined for each similar node separately. In both cases, the transferability of the coarse-grained model would be hampered.

The fourth and final challenge, which is the main impetus for the micromechanical model, is that the length scale attainable by state-of-the-art coarse-grained models for MOFs is still limited to a few tens of nanometres.[29] This results from the fact that even the coarsest MOF models used up to now achieve a reduction in the number of beads of about one order of magnitude.[29,52] To describe cooperative phenomena or correlated disorder that go beyond a few tens of nanometres, however, a fundamentally different coarse-graining procedure with a further reduction in the number of beads is necessary.[14]

2.2 The nodal micromechanical mapping procedure

To address the four challenges mentioned above, the first step in the micromechanical model is to define a mapping that reduces the number of interaction beads by two to three orders of magnitude (see step 1 in Fig. 2). This is achieved by observing that mesoscopic MOF crystals, with dimensions of several hundreds of nanometres and containing several millions of atoms, can be easily partitioned into smaller unit cells with dimensions of about one nanometre given the MOF's building block structure. These nanosized unit cells, which will be further referred to as nanocells, are defined by the position of their eight corners (in 3D). In the micromechanical model, the position of these corners, which define the coarse-grained nodes of the model, will be simulated. As indicated in Fig. 3 for three representative MOFs, the mapping of the atomistic unit cells to coarse-grained nodes achieves the targeted reduction in degrees of freedom of more than two orders of magnitude.

To illustrate this mapping procedure, consider the mesoscopic material shown in step 1 of Fig. 2. For this 2D material, the nodes are indexed with a couple of integers (i,j), ranging from $(0, 0)$ to (n_x, n_y). These nodes are characterised by their position $\boldsymbol{r}_{ij}$ and mass m_{ij}, which is determined based on the average mass of the surrounding nanocells. In turn, these nodes uniquely define the positions of the different nanocells $\mathbf{h}_{\mu\nu}$, as outlined in Section S1.1 of the ESI.† In the model, the nodes at the boundaries of the mesoscopic material can either be free, mimicking finite materials, or they can be coupled through periodic boundary conditions, mimicking the bulk region of an even larger material.

ART ■ C9FD00148D

Next, a nanocell type is assigned to each nanocell in the material, indicated with the different colors in Fig. 2. This nanocell type is uniquely defined by the spatial disorder present in or at the surface of the nanocell. The nanocell type will remain unaltered during the simulation, given that classical simulations do not allow for bonds to be broken or formed. However, as outlined in more detail in Section 2.4, these nanocell types can dynamically switch between multiple phases as long as all bonds remain intact during the transition. For instance, different nanocell types could be assigned to the different defective nanoregions in UiO-66, such as the single green nanodefect region in Fig. 2. Likewise, surfaces can be described by identifying surface nanocell types, such as those indicated by the two shades of orange in Fig. 2. These surfaces can be external, to describe the finite crystal size, or internal, to describe mesopores. The number of nanocell types, typically smaller than ten, determines the complexity of the micromechanical model and the number of atomistic simulations needed to parametrise the model, as outlined in Section 2.3.

2.3 The micromechanical equations of motion for unistable nanocells

Atomistically, external stimuli and spatial disorder in MOFs result in distorted nanocells. The assumption made in the micromechanical model is that this altered performance at the atomistic level can be used to characterise the nodal interactions near equilibrium. Consequently, the parameters of the micromechanical model are the 3×3 equilibrium cell matrices $\mathbf{h}_{\mu\nu\kappa,0}$ and the fourth-order $3 \times 3 \times 3 \times 3$ stiffness tensors $\mathbf{C}_{\mu\nu\kappa,0}$ for each of the nanocells in the model. Both the equilibrium cell matrices and the stiffness tensors can be *a priori* determined from atomistic simulations,[59] which need to be performed for each different nanocell type (step 2 in Fig. 2). These parameters can be used to define the 3×3 finite Lagrangian strain tensor $\boldsymbol{\varepsilon}_{\mu\nu\kappa}$ experienced by the nanocell $\mathbf{h}_{\mu\nu\kappa}$ as

$$\boldsymbol{\varepsilon}_{\mu\nu\kappa} = \frac{1}{2}\left[\mathbf{h}_{\mu\nu\kappa,0}^{-\mathrm{T}}\mathbf{h}_{\mu\nu\kappa}^{\mathrm{T}}\mathbf{h}_{\mu\nu\kappa}\mathbf{h}_{\mu\nu\kappa,0}^{-1} - \mathbf{1}\right], \tag{1}$$

in which $\mathbf{1}$ is the 3×3 unit tensor.[60] In turn, this leads to the following elastic potential energy associated with each of the nanocells:

$$\mathscr{U}_{\mu\nu\kappa} = \frac{1}{2}\det(\mathbf{h}_{\mu\nu\kappa})\boldsymbol{\varepsilon}_{\mu\nu\kappa}^{\mathrm{T}} : \mathbf{C}_{\mu\nu\kappa,0} : \boldsymbol{\varepsilon}_{\mu\nu\kappa}. \tag{2}$$

In this expression, ':' denotes the matrix inner product:

$$\left[\boldsymbol{\varepsilon}^{\mathrm{T}} : \mathbf{C}\right]_{k\ell} = \sum_{i=1}^{3}\sum_{j=1}^{3}\varepsilon_{ji}C_{ijk\ell} \text{ and } \left[\mathbf{C} : \boldsymbol{\varepsilon}\right]_{k\ell} = \sum_{i=1}^{3}\sum_{j=1}^{3}C_{k\ell ij}\varepsilon_{ij}. \tag{3}$$

As outlined in Section S1.2 of the ESI,† this elastic deformation energy naturally leads to the following Hamiltonian for the micromechanical model:

$$\mathscr{H}(\boldsymbol{r},\boldsymbol{p}) = \sum_{ijk}\frac{\boldsymbol{p}_{ijk}{}^{2}}{2m_{ijk}} + \sum_{\mu\nu\kappa}\mathscr{U}_{\mu\nu\kappa}(\boldsymbol{r}), \tag{4}$$

where $\boldsymbol{p}_{ijk}$ is the conjugated momentum of the node at position $\boldsymbol{r}_{ijk}$.

From this Hamiltonian, the equations of motion can be derived as

$$\dot{\boldsymbol{r}}_{ijk} = \nabla_{\boldsymbol{p}_{ijk}} \mathscr{H} = \frac{\boldsymbol{p}_{ijk}}{m_{ijk}} = \boldsymbol{v}_{ijk}, \tag{5}$$

$$\dot{\boldsymbol{p}}_{ijk} = -\nabla_{\boldsymbol{r}_{ijk}} \mathscr{H} = -\sum_{\mu=i-1}^{i} \sum_{\nu=j-1}^{j} \sum_{\kappa=k-1}^{k} \nabla_{\boldsymbol{r}_{ijk}} \mathscr{U}_{\mu\nu\kappa}(\boldsymbol{r}). \tag{6}$$

As outlined in Sections S1.3 and S1.4 of the ESI,† eqn (6) can be written out explicitly, yielding for instance for the x-component of the conjugated momentum of the node at position (i, j, k):

$$\dot{p}_{ijk,x} = -\frac{1}{2} \sum_{\mu=i-1}^{i} \sum_{\nu=j-1}^{j} \sum_{\kappa=k-1}^{k} \det(\mathbf{h}_{\mu\nu\kappa}) \times \left[\mathrm{Tr}\left\{ \mathbf{h}_{\mu\nu\kappa}^{-1} \frac{\partial}{\partial x_{ijk}} \mathbf{h}_{\mu\nu\kappa} \right\} \boldsymbol{\varepsilon}_{\mu\nu\kappa}^{\mathrm{T}} : \mathbf{C}_{\mu\nu\kappa,0} : \boldsymbol{\varepsilon}_{\mu\nu\kappa} \right.$$
$$\left. + \frac{1}{32} \left(\mathbf{h}_{\mu\nu\kappa,0}^{-\mathrm{T}} \mathbf{F}_{n_{\mu\nu\kappa},x} \mathbf{h}_{\mu\nu\kappa,0}^{-1} \right) : \mathbf{C}_{\mu\nu\kappa,0} : \boldsymbol{\varepsilon}_{\mu\nu\kappa} + \frac{1}{32} \boldsymbol{\varepsilon}_{\mu\nu\kappa}^{\mathrm{T}} : \mathbf{C}_{\mu\nu\kappa,0} : \left(\mathbf{h}_{\mu\nu\kappa,0}^{-\mathrm{T}} \mathbf{F}_{n_{\mu\nu\kappa},x} \mathbf{h}_{\mu\nu\kappa,0}^{-1} \right) \right]. \tag{7}$$

In this expression, $\mathrm{Tr}\{\mathbf{A}\}$, $\mathbf{A}^{-1}$, and $\mathbf{A}^{\mathrm{T}}$ are the trace, the inverse, and the transpose of matrix $\mathbf{A}$, respectively, and $\mathbf{A}^{-\mathrm{T}} = (\mathbf{A}^{-1})^{\mathrm{T}}$. The matrix $\mathbf{F}_{n_{\mu\nu\kappa},x}$, with elements

$$\mathbf{F}_{n_{\mu\nu\kappa},x} = \begin{bmatrix} 2f_{n_{\mu\nu\kappa}} & f_{n_{\mu\nu\kappa}} & f_{n_{\mu\nu\kappa}} \\ f_{n_{\mu\nu\kappa}} & 0 & 0 \\ f_{n_{\mu\nu\kappa}} & 0 & 0 \end{bmatrix}, \tag{8}$$

contains one of the functions f_1 to f_8, corresponding to the contribution of each of the eight neighbouring nanocells $\mathbf{h}_{\mu\nu\kappa}$ that have the node in position (i, j, k) on one of their corners, as expressed by the summation in eqn (6). As outlined in Section S1.3 of the ESI,† f_1 to f_8 are simple linear functions of the coordinates of the 27 nodes that form these eight nanocells, with the node in position (i, j, k) as the central node.

The here obtained equations of motion can be used to dynamically propagate the mesoscale material using the equilibrium cell matrix and the equilibrium stiffness tensor as input parameters (step 3 in Fig. 2), and can be supplemented by thermostats and barostats to achieve temperature and pressure control, respectively, similar to the atomistic equations of motion.[61]

2.4 Extension of the micromechanical model towards bistable nanocells

The micromechanical equations of motion derived in Section 2.3 only take into account the elastic deformation of the material through the elastic deformation energy of eqn (2). While this is sufficient to extract the properties of the mesoscopic material near equilibrium, such as its equilibrium volume, bulk modulus, or thermal expansion, there is growing attention to the anharmonic, out-of-equilibrium responses of MOFs, such as their transition or amorphization pressures. Essential in these out-of-equilibrium phenomena is that the material can undergo a transition between two phases. To capture these effects, the bistability of these materials needs to be directly incorporated in the micromechanical model by considering bistable instead of unistable nanocells.

To describe nanocells that have two (meta)stable phases, information about the deformation energy of the two phases and their relative stability needs to be provided instead of the single deformation energy of eqn (2). As shown in Fig. 4,

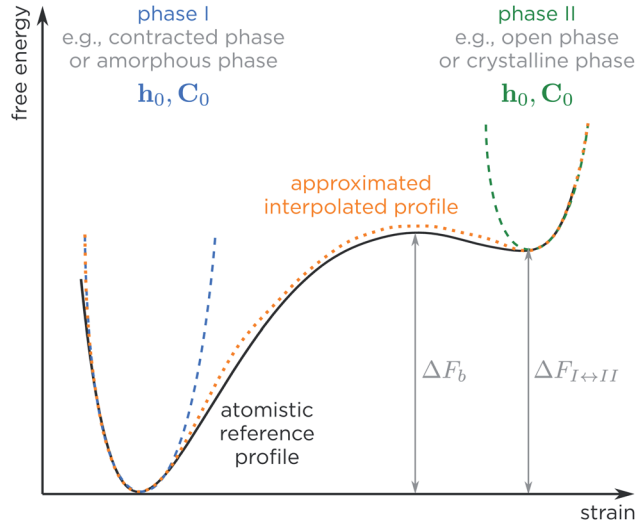

Fig. 4 Visual representation of the procedure to extend the micromechanical model to systems with multiple metastable phases. The two dashed parabolas indicate the harmonic responses of the two phases, I and II, separately, while the orange dotted line is the interpolation obtained according to the procedure in ref. 62.

this information encompasses the equilibrium matrices $\mathbf{h}_{\mu\nu\kappa,0}$ and the stiffness tensors $\mathbf{C}_{\mu\nu\kappa,0}$ of the two phases, I and II, as well as their relative difference in free energy $\Delta F_{\mathrm{I}\leftrightarrow\mathrm{II},\mu\nu\kappa}$ and finally the height of the barrier between the two phases $\Delta F_{\mathrm{b},\mu\nu\kappa}$. Based on this information, the deformation energies $\mathscr{U}^{(\mathrm{I})}_{\mu\nu\kappa}$ and $\mathscr{U}^{(\mathrm{II})}_{\mu\nu\kappa}$ of the two phases can be determined separately *via* eqn (1), yielding the harmonic equilibrium response for both phases as shown in Fig. 4. To combine these two potential energies into an interpolated potential energy that spans both phases of the bistable nanocell, the approach of Christ and van Gunsteren is adopted,[62] yielding the following potential energy surface for the bistable nanocell $\mathbf{h}_{\mu\nu\kappa}$:

$$\mathscr{U}_{\mu\nu\kappa} = -k_{\mathrm{B}} T^*_{\mu\nu\kappa} \ln\left[\exp\left(-\frac{\mathscr{U}^{(\mathrm{I})}_{\mu\nu\kappa}}{k_{\mathrm{B}} T^*_{\mu\nu\kappa}}\right) + \exp\left(-\frac{\mathscr{U}^{(\mathrm{II})}_{\mu\nu\kappa} + \Delta F_{\mathrm{I}\leftrightarrow\mathrm{II},\mu\nu\kappa}}{k_{\mathrm{B}} T^*_{\mu\nu\kappa}}\right)\right]. \quad (9)$$

In this expression, k_{B} is the Boltzmann constant and $T^*_{\mu\nu\kappa}$ is an effective temperature that determines the smoothness of the interpolation. In practice, the parameter $T^*_{\mu\nu\kappa}$ should be fitted to best reproduce the barrier $\Delta F_{\mathrm{b},\mu\nu\kappa}$ obtained from atomistic simulations.

The updated equations for the positions of the nodes of unistable nanocells, eqn (5), remain unaltered when considering bistable nanocells. For the momenta of the nodes, eqn (6), the derivatives $-\nabla_{\boldsymbol{r}_{ijk}} \mathscr{U}_{\mu\nu\kappa}(\boldsymbol{r})$ depend on whether the nanocell $\mathbf{h}_{\mu\nu\kappa}$ is unistable, as in Section 2.3, or bistable. As outlined in Section S2 of the ESI,† the derivative of the bistable potential energy is a weighted linear combination of the derivatives of the two single-phase deformation potential energies:

$$\nabla_{\boldsymbol{r}_{ijk}} \mathscr{U}_{\mu\nu\kappa}(\boldsymbol{r}) = w^{(\mathrm{I})}_{\mu\nu\kappa}(\boldsymbol{r}) \nabla_{\boldsymbol{r}_{ijk}} \mathscr{U}^{(\mathrm{I})}_{\mu\nu\kappa}(\boldsymbol{r}) + w^{(\mathrm{II})}_{\mu\nu\kappa}(\boldsymbol{r}) \nabla_{\boldsymbol{r}_{ijk}} \mathscr{U}^{(\mathrm{II})}_{\mu\nu\kappa}(\boldsymbol{r}), \quad (10)$$

with weight factors

$$w_{\mu\nu\kappa}^{(\mathrm{I})}(\boldsymbol{r}) = \frac{\exp\left(-\dfrac{\mathscr{U}_{\mu\nu\kappa}^{(\mathrm{I})}(\boldsymbol{r})}{k_{\mathrm{B}}T_{\mu\nu\kappa}^{*}}\right)}{\exp\left(-\dfrac{\mathscr{U}_{\mu\nu\kappa}^{(\mathrm{I})}(\boldsymbol{r})}{k_{\mathrm{B}}T_{\mu\nu\kappa}^{*}}\right) + \exp\left(-\dfrac{\mathscr{U}_{\mu\nu\kappa}^{(\mathrm{II})}(\boldsymbol{r}) + \Delta F_{I\leftrightarrow II,\mu\nu\kappa}}{k_{\mathrm{B}}T_{\mu\nu\kappa}^{*}}\right)}; \tag{11}$$

$$w_{\mu\nu\kappa}^{(\mathrm{II})}(\boldsymbol{r}) = \frac{\exp\left(-\dfrac{\mathscr{U}_{\mu\nu\kappa}^{(\mathrm{II})}(\boldsymbol{r}) + \Delta F_{\mathrm{I}\leftrightarrow\mathrm{II},\mu\nu\kappa}}{k_{\mathrm{B}}T_{\mu\nu\kappa}^{*}}\right)}{\exp\left(-\dfrac{\mathscr{U}_{\mu\nu\kappa}^{(\mathrm{I})}(\boldsymbol{r})}{k_{\mathrm{B}}T_{\mu\nu\kappa}^{*}}\right) + \exp\left(-\dfrac{\mathscr{U}_{\mu\nu\kappa}^{(\mathrm{II})}(\boldsymbol{r}) + \Delta F_{\mathrm{I}\leftrightarrow\mathrm{II},\mu\nu\kappa}}{k_{\mathrm{B}}T_{\mu\nu\kappa}^{*}}\right)}. \tag{12}$$

Compared to the unistable case, bistable nanocells will hence require two evaluations of the derivative of the potential energy, $\nabla_{\boldsymbol{r}_{ijk}}\mathscr{U}_{\mu\nu\kappa}^{(\mathrm{I})}(\boldsymbol{r})$ and $\nabla_{\boldsymbol{r}_{ijk}}\mathscr{U}_{\mu\nu\kappa}^{(\mathrm{II})}(\boldsymbol{r})$, at every time step. As in the unistable case, however, all required input parameters—the equilibrium cell matrices, the stiffness tensors, the relative free energy difference, and the free energy barrier between the phases—are obtained from *a priori* atomistic simulations and need to be derived only for the different nanocell types, again limiting the complexity of the model.

3 Discussion

The micromechanical model introduced here follows a fundamentally different approach to coarse-graining MOFs compared to traditional coarse-graining techniques, exploiting the natural partitioning of the MOF material in similar nanocells. The three main differences between the micromechanical model and conventional coarse-grained force fields are highlighted by the equations of motion derived in Sections 2.3 and 2.4.

First, even though the micromechanical model adopts a coarse mapping procedure that is very similar for all MOFs, information about the topology of the atomistic material is still partially contained in the equilibrium cell matrices and the stiffness tensors. This is a deliberate choice, as the topology of the material was found to be an indispensable factor to accurately predict the structural and mechanical responses of MOFs to external stimuli.[63,64]

Second, the interactions in the micromechanical model are not restricted to nearest-neighbour beads, but include *via* eqn (8) interactions with all neighbouring beads that share at least one nanocell. This increases the complexity of the model compared to conventional coarse-graining techniques, although the functional form of the interactions remains simple and the mapping procedure already introduces a substantial reduction in complexity.

Third, the parameters that are used as input for the micromechanical model—equilibrium cell matrices and equilibrium stiffness tensors, possibly extended by differences in free energy in the case of bistable nanocells—are well-defined variables that can, to a large extent, be obtained experimentally. This contrasts with the often arbitrary analytical interaction terms used in conventional coarse-grained force fields, for which the accuracy of the interaction terms can only be determined *a posteriori* by comparing the results predicted by the coarse-grained model with experimental results. Even then, if a mismatch with experiment is

obtained, it is often not trivial to pinpoint which interaction terms are missing or which terms need to be refined to improve the accuracy of conventional coarse-graining procedures. In contrast, in the micromechanical model, the input parameters can be *a priori* compared with experiment. Furthermore, if higher-level force field or quantum mechanical information would be challenging to obtain, these input parameters can also be directly extracted from experiment.

As a result of the specific approach followed in the micromechanical model, the four challenges outlined in Section 2.1 can be addressed. As visualised in Fig. 3, the micromechanical model maps the unit cell of the material, with a given space group, on its crystal system instead of mapping the different atoms inside the cell onto arbitrary coarse-grained beads as in conventional coarse-graining techniques. Conceptually, the reduction of the unit cell to its crystal system can be regarded as the periodic analogon of reducing the isolated building blocks in the material to their point group. As a result of this specific mapping procedure, the micromechanical model does not require the atomistic building blocks to be partitioned in different beads, circumventing the challenges related to highly symmetric building blocks, such as the $Zr_6(\mu_3\text{-}OH)_4(\mu_3\text{-}O)_4$ inorganic node in UiO-66(Zr), and building blocks that extend along chains, such as the $[Al(\mu_2\text{-}OH)]_n$ chain in MIL-53(Al). Moreover, as the different nodes in the micromechanical model can move independently, the crystal system of any given nanocell can change during the simulation, which is a prerequisite in modelling phase transitions.

Furthermore, nanocells that are structurally and mechanically similar will be characterised by nanocell types that have similar equilibrium cell matrices and equilibrium stiffness tensors. Combined with the straightforward mapping procedure in Fig. 3, this ensures that the micromechanical model is easily transferable between different MOFs or between MOFs containing various types of spatial disorder, overcoming the third challenge in Section 2.1. As a result, the micromechanical model can be adopted to investigate possible cooperative effects that arise from multiple types of spatial disorder being present in the material at the same time, such as the combination of node defects and boundary effects present in the hypothetical UiO-66 material in Fig. 2. In addition, the model can also describe hybrid materials in which a given MOF is dispersed into a different MOF matrix, such as the recently synthesised MIL-53/ZIF-62 hybrid.[65]

Finally, the gain in attainable length scale in the micromechanical model is expected to be substantially larger than for atomistic or conventional coarse-grained MOF models, due to three factors. First, the mapping procedure results in a reduction in degrees of freedom of two to three orders of magnitude with respect to atomistic models, thereby going beyond the reductions achieved by state-of-the-art coarse-grained MOF models.[29,52] In addition, the Hamiltonian of the micromechanical model, expressed in eqn (4), is smoother than the atomistic Hamiltonian, as it no longer contains atomistic high-frequency modes such as O–H and C–H stretches. As a result, the time step used during a molecular dynamics simulation with the micromechanical model can be about one order of magnitude larger than in the atomistic case without violating the Nyquist theorem. Finally, due to the absence of long-range interactions, the force evaluations in the micromechanical model will be faster than in the atomistic case. As a result, the micromechanical model has the potential to computationally describe

ART ■ C9FD00148D

cooperative phenomena and correlated spatial disorder at length scales beyond the few tens of nanometres achievable today.

The micromechanical model relies on the partitioning of the material in nanocells and the determination of the equilibrium cell matrices and stiffness tensors of these nanocells. While this is a natural approach for largely crystalline MOFs, it becomes less straightforward to define these parameters when considering glassy or amorphous materials.[44] This is for instance the case when describing the amorphization of UiO-66(Zr), in which phase I in Fig. 4 corresponds to an amorphous phase next to the crystalline phase II. If we are only interested in the amorphization pressure, *i.e.*, the pressure required to go from phase II to phase I, the exact parametrisation of the amorphous phase can be expected to be less important, as an accurate reproduction of the amorphization pressure of the nanocell only requires information on the crystalline phase and the point at which the structural response of the crystalline material becomes highly anharmonic.[58] As a result, the amorphization pressure of the different nanocells can be captured by fitting the parameters $\Delta F_{\mathrm{I}\leftrightarrow\mathrm{II}}$ and T^* of the model to atomistic data obtained for the nanocell. In addition, given that the input parameters of the model can be determined experimentally, the amorphous phase can also be parametrised based on experiment. In this sense, the micromechanical model may also form a complementary computational tool to help refine the experimental structures of these amorphous or glassy phases based on the experimentally observed macroscopic behaviour of the MOF.[14]

4 Conclusions

Spatially extended computational models are necessary to understand on a fundamental level how the variety of interactions and various types of spatial disorder in MOFs lead to the experimentally observed cooperative phenomena in these materials. However, conventional computational techniques are often inadequate for coarse-graining periodic network materials such as MOFs as they lead to an insufficient increase in length scale that can be described in the model. Therefore, the micromechanical model is introduced here as a fundamentally different coarse-graining approach that exploits the natural partitioning of MOFs into nanometre-sized cells. This model consists of two ingredients: a systematic procedure to map the atomistic unit cells onto coarse-grained nanocells, leading to a reduction in the number of degrees of freedom of about two to three orders of magnitude, and a description of the nodal Hamiltonian that defines the equations of motion to propagate the micromechanical model in time.

Herein, the concept of the micromechanical model is outlined and the equations of motion for both unistable and bistable materials are derived. In contrast to conventional coarse-graining techniques, the model is only based on experimentally verifiable input parameters, which can be determined from higher-level quantum mechanical or force field simulations. As a result, the here proposed micromechanical model can be considered as a hierarchical method that builds upon atomic-level information to predict how cooperative phenomena and correlated spatial disorder affect the performance of mesoscale MOF materials under experimental conditions.

Conflicts of interest

There are no conflicts to declare.

Acknowledgements

This work is supported by the Fund for Scientific Research Flanders (FWO) through a postdoctoral fellowship (grant no. 12T3519N). Fruitful discussions on the concept and the scope of the micromechanical model with Prof. Veronique Van Speybroeck and Prof. Toon Verstraelen are gratefully acknowledged.

References

1 H. Li, M. Eddaoudi, M. O'Keeffe and O. M. Yaghi, *Nature*, 1999, **402**, 276–279.
2 G. Férey, *Chem. Mater.*, 2001, **13**, 3084–3098.
3 S. Kitagawa, R. Kitaura and S.-i. Noro, *Angew. Chem., Int. Ed.*, 2004, **43**, 2334–2375.
4 O. M. Yaghi, M. O'Keeffe, N. W. Ockwig, H. K. Chae, M. Eddaoudi and J. Kim, *Nature*, 2003, **423**, 705–714.
5 F.-X. Coudert, *Chem. Mater.*, 2015, **27**, 1905–1916.
6 S. Krause, V. Bon, I. Senkovska, U. Stoeck, D. Wallacher, D. M. Többens, S. Zander, R. S. Pillai, G. Maurin, F.-X. Coudert and S. Kaskel, *Nature*, 2016, **532**, 348–352.
7 A. U. Ortiz, A. Boutin, A. H. Fuchs and F.-X. Coudert, *Phys. Rev. Lett.*, 2012, **109**, 195502.
8 S. Horike, S. Shimomura and S. Kitagawa, *Nat. Chem.*, 2009, **1**, 695–704.
9 A. Schneemann, V. Bon, I. Schwedler, I. Senkovska, S. Kaskel and R. A. Fischer, *Chem. Soc. Rev.*, 2014, **43**, 6062–6096.
10 L. Vanduyfhuys, S. M. J. Rogge, J. Wieme, S. Vandenbrande, G. Maurin, M. Waroquier and V. Van Speybroeck, *Nat. Commun.*, 2018, **9**, 204.
11 K. T. Butler, A. Walsh, A. K. Cheetham and G. Kieslich, *Chem. Sci.*, 2016, **7**, 6316–6324.
12 K. T. Butler, J. M. Frost, J. M. Skelton, K. L. Svane and A. Walsh, *Chem. Soc. Rev.*, 2016, **45**, 6138–6146.
13 F.-X. Coudert and A. H. Fuchs, *Coord. Chem. Rev.*, 2016, **307**, 211–236.
14 A. L. Goodwin, *Nat. Commun.*, 2019, **10**, 4461.
15 Y. Sakata, S. Furukawa, M. Kondo, K. Hirai, N. Horike, Y. Takashima, H. Uehara, N. Louvain, M. Meilikhov, T. Tsuruoka, S. Isoda, W. Kosaka, O. Sakata and S. Kitagawa, *Science*, 2013, **339**, 193–196.
16 H. Miura, V. Bon, I. Senkovska, S. Ehrling, S. Watanabe, M. Ohba and S. Kaskel, *Dalton Trans.*, 2017, **46**, 14002–14011.
17 S. Krause, V. Bon, I. Senkovska, D. M. Többens, D. Wallacher, R. S. Pillai, G. Maurin and S. Kaskel, *Nat. Commun.*, 2018, **9**, 1573.
18 S. Wannapaiboon, A. Schneemann, I. Hante, M. Tu, K. Epp, A. L. Semrau, C. Sternemann, M. Paulus, S. J. Baxter, G. Kieslich and R. A. Fischer, *Nat. Commun.*, 2019, **10**, 346.
19 T. Kundu, M. Wahiduzzaman, B. B. Shah, G. Maurin and D. Zhao, *Angew. Chem., Int. Ed.*, 2019, **58**, 8073–8077.

20 S. Ehrling, I. Senkovska, V. Bon, J. D. Evans, P. Petkov, Y. Krupskaya, V. Kataev, T. Wulf, A. Krylov, A. Vtyurin, S. Krylova, S. Adichtchev, E. Slyusareva, M. S. Weiss, B. Büchner, T. Heine and S. Kaskel, *J. Mater. Chem. A*, 2019, **7**, 21459–21475.
21 S. O. Odoh, C. J. Cramer, D. G. Truhlar and L. Gagliardi, *Chem. Rev.*, 2015, **115**, 6051–6111.
22 S. M. J. Rogge, A. Bavykina, J. Hajek, H. Garcia, A. I. Olivos-Suarez, A. Sepúlveda-Escribano, A. Vimont, G. Clet, P. Bazin, F. Kapteijn, M. Daturi, E. V. Ramos-Fernandez, F. X. Llabrés i Xamena, V. Van Speybroeck and J. Gascon, *Chem. Soc. Rev.*, 2017, **46**, 3134–3184.
23 S. Bureekaew, S. Amirjalayer, M. Tafipolsky, C. Spickermann, T. K. Roy and R. Schmid, *Phys. Status Solidi B*, 2013, **250**, 1128–1141.
24 H. Fang, H. Demir, P. Kamakoti and D. S. Sholl, *J. Mater. Chem. A*, 2014, **2**, 274–291.
25 L. Vanduyfhuys, S. Vandenbrande, T. Verstraelen, R. Schmid, M. Waroquier and V. Van Speybroeck, *J. Comput. Chem.*, 2015, **36**, 1015–1027.
26 J. Heinen and D. Dubbeldam, *Wiley Interdiscip. Rev.: Comput. Mol. Sci.*, 2018, **8**, e1363.
27 J. Keupp and R. Schmid, *Adv. Theory Simul.*, 2019, **2**, 1900117.
28 S. M. J. Rogge, M. Waroquier and V. Van Speybroeck, *Nat. Commun.*, 2019, **10**, 4842.
29 J. P. Dürholt, R. Galvelis and R. Schmid, *Dalton Trans.*, 2016, **45**, 4370–4379.
30 L. Valenzano, B. Civalleri, S. Chavan, S. Bordiga, M. H. Nilsen, S. Jakobsen, K. P. Lillerud and C. Lamberti, *Chem. Mater.*, 2011, **23**, 1700–1718.
31 C. A. Trickett, K. J. Gagnon, S. Lee, F. Gándara, H.-B. Bürgi and O. M. Yaghi, *Angew. Chem., Int. Ed.*, 2015, **54**, 11162–11167.
32 G. C. Shearer, S. Chavan, S. Bordiga, S. Svelle, U. Olsbye and K. P. Lillerud, *Chem. Mater.*, 2016, **28**, 3749–3761.
33 W. Zhang, M. Kauer, P. Guo, S. Kunze, S. Cwik, M. Muhler, Y. Wang, K. Epp, G. Kieslich and R. A. Fischer, *Eur. J. Inorg. Chem.*, 2017, **2017**, 925–931.
34 O. Kozachuk, M. Meilikhov, K. Yusenko, A. Schneemann, B. Jee, A. V. Kuttatheyil, M. Bertmer, C. Sternemann, A. Pöppl and R. A. Fischer, *Eur. J. Inorg. Chem.*, 2013, **2013**, 4546–4557.
35 M. J. Cliffe, W. Wan, X. Zou, P. A. Chater, A. K. Kleppe, M. G. Tucker, H. Wilhelm, N. P. Funnell, F.-X. Coudert and A. L. Goodwin, *Nat. Commun.*, 2014, **5**, 4176.
36 S. Diring, S. Furukawa, Y. Takashima, T. Tsuruoka and S. Kitagawa, *Chem. Mater.*, 2010, **22**, 4531–4538.
37 Z. Fang, J. P. Dürholt, M. Kauer, W. Zhang, C. Lochenie, B. Jee, B. Albada, N. Metzler-Nolte, A. Pöppl, B. Weber, M. Muhler, Y. Wang, R. Schmid and R. A. Fischer, *J. Am. Chem. Soc.*, 2014, **136**, 9627–9636.
38 Y. Liu, J.-H. Her, A. Dailly, A. J. Ramirez-Cuesta, D. A. Neumann and C. M. Brown, *J. Am. Chem. Soc.*, 2008, **130**, 11813–11818.
39 N. Kavoosi, V. Bon, I. Senkovska, S. Krause, C. Atzori, F. Bonino, J. Pallmann, S. Paasch, E. Brunner and S. Kaskel, *Dalton Trans.*, 2017, **46**, 4685–4695.
40 T. D. Bennett, T. K. Todorova, E. F. Baxter, D. G. Reid, C. Gervais, B. Bueken, B. Van de Voorde, D. De Vos, D. A. Keen and C. Mellot-Draznieks, *Phys. Chem. Chem. Phys.*, 2016, **18**, 2192–2201.

41 K. W. Chapman, G. J. Halder and P. J. Chupas, *J. Am. Chem. Soc.*, 2009, **131**, 17546–17547.
42 T. D. Bennett and A. K. Cheetham, *Acc. Chem. Res.*, 2014, **47**, 1555–1562.
43 R. Gaillac, P. Pullumbi, K. A. Beyer, K. W. Chapman, D. A. Keen, T. D. Bennett and F.-X. Coudert, *Nat. Mater.*, 2017, **16**, 1149–1154.
44 J. M. Tuffnell, C. W. Ashling, J. Hou, S. Li, L. Longley, M. L. Ríos Gómez and T. D. Bennett, *Chem. Commun.*, 2019, **55**, 8705–8715.
45 R. Ameloot, F. Vermoortele, J. Hofkens, F. C. De Schryver, D. E. De Vos and M. B. J. Roeffaers, *Angew. Chem., Int. Ed.*, 2013, **52**, 401–405.
46 Z. Fang, B. Bueken, D. E. De Vos and R. A. Fischer, *Angew. Chem., Int. Ed.*, 2015, **54**, 7234–7254.
47 M. J. Cliffe, J. A. Hill, C. A. Murray, F.-X. Coudert and A. L. Goodwin, *Phys. Chem. Chem. Phys.*, 2015, **17**, 11586–11592.
48 J. Ren, M. Ledwaba, N. M. Musyoka, H. W. Langmi, M. Mathe, S. Liao and W. Pang, *Coord. Chem. Rev.*, 2017, **349**, 169–197.
49 W. G. Noid, *J. Chem. Phys.*, 2013, **139**, 090901.
50 H. I. Ingólfsson, C. A. Lopez, J. J. Uusitalo, D. H. de Jong, S. M. Gopal, X. Periole and S. J. Marrink, *Wiley Interdiscip. Rev.: Comput. Mol. Sci.*, 2014, **4**, 225–248.
51 N. Singh and W. Li, *Int. J. Mol. Sci.*, 2019, **20**, 3774.
52 R. Semino, J. P. Dürholt, R. Schmid and G. Maurin, *J. Phys. Chem. C*, 2017, **121**, 21491–21496.
53 S. J. Marrink and D. P. Tieleman, *Chem. Soc. Rev.*, 2013, **42**, 6801–6822.
54 T. Loiseau, C. Serre, C. Huguenard, G. Fink, F. Taulelle, M. Henry, T. Bataille and G. Férey, *Chem.–Eur. J.*, 2004, **10**, 1373–1382.
55 S. S.-Y. Chui, S. M.-F. Lo, J. P. H. Charmant, A. G. Orpen and I. D. Williams, *Science*, 1999, **283**, 1148–1150.
56 J. H. Cavka, S. Jakobsen, U. Olsbye, N. Guillou, C. Lamberti, S. Bordiga and K. P. Lillerud, *J. Am. Chem. Soc.*, 2008, **130**, 13850–13851.
57 W. G. Noid, J.-W. Chu, G. S. Ayton, V. Krishna, S. Izvekov, G. A. Voth, A. Das and H. C. Andersen, *J. Chem. Phys.*, 2008, **128**, 244114.
58 S. M. J. Rogge, J. Wieme, L. Vanduyfhuys, S. Vandenbrande, G. Maurin, T. Verstraelen, M. Waroquier and V. Van Speybroeck, *Chem. Mater.*, 2016, **28**, 5721–5732.
59 S. M. J. Rogge, M. Waroquier and V. Van Speybroeck, *Acc. Chem. Res.*, 2018, **51**, 138–148.
60 E. B. Tadmor and R. E. Miller, *Modeling Materials: Continuum, Atomistic and Multiscale Techniques*, Cambridge University Press, New York, 2011.
61 S. M. J. Rogge, L. Vanduyfhuys, A. Ghysels, M. Waroquier, T. Verstraelen, G. Maurin and V. Van Speybroeck, *J. Chem. Theory Comput.*, 2015, **11**, 5583–5597.
62 C. D. Christ and W. F. van Gunsteren, *J. Chem. Phys.*, 2007, **126**, 184110.
63 J. C. Tan, T. D. Bennett and A. K. Cheetham, *Proc. Natl. Acad. Sci. U. S. A.*, 2010, **107**, 9938–9943.
64 P. Z. Moghadam, S. M. J. Rogge, A. Li, C.-M. Chow, J. Wieme, N. Moharrami, M. Aragones-Anglada, G. Conduit, D. A. Gomez-Gualdron, V. Van Speybroeck and D. Fairen-Jimenez, *Matter*, 2019, **1**, 219–234.
65 J. Hou, C. W. Ashling, S. M. Collins, A. Krajnc, C. Zhou, L. Longley, D. N. Johnstone, P. A. Chater, S. Li, M.-V. Coulet, P. L. Llewellyn, F.-X. Coudert, D. A. Keen, P. A. Midgley, G. Mali, V. Chen and T. D. Bennett, *Nat. Commun.*, 2019, **10**, 2580.

Faraday Discussions

Cite this: DOI: 10.1039/d0fd00016g

PAPER

Cooperative and synchronized rotation in motorized porous frameworks: impact on local and global transport properties of confined fluids†

Jack D. Evans, *[a] Simon Krause [b] and Ben L. Feringa [b]

Received 24th January 2020, Accepted 9th March 2020
DOI: 10.1039/d0fd00016g

Molecules in gas and liquid states, as well as in solution, exhibit significant and random Brownian motion. Molecules in the solid-state, although strongly immobilized, can still exhibit significant intramolecular dynamics. However, in most framework materials, these intramolecular dynamics are driven by temperature, and therefore are neither controlled nor spatially or temporarily aligned. In recent years, several examples of molecular machines that allow for a stimuli-responsive control of dynamical motion, such as rotation, have been reported. In this contribution, we investigate the local and global properties of a Lennard-Jones (LJ) fluid surrounding a molecular motor and consider the influence of cooperative and non-directional rotation for a molecular motor-containing pore system. This study uses classical molecular dynamics simulations to describe a minimal model, which was developed to resemble known molecular motors. The properties of an LJ liquid surrounding an isolated molecular motor remain mostly unaffected by the introduced rotation. We then considered an arrangement of motors within a one-dimensional pore. Changes in diffusivity for pore sizes approaching the length of the rotor were observed, resulting from rotation of the motors. We also considered the influence of cooperative motor directionality on the directional transport properties of this confined fluid. Importantly, we discovered that specific unidirectional rotation of altitudinal motors can produce directed diffusion. This study provides an essential insight into molecular machine-containing frameworks, highlighting the specific structural arrangements that can produce directional mass transport.

[a]Department of Inorganic Chemistry, Technische Universität Dresden, Bergstraße 66, 01062 Dresden, Germany. E-mail: jack.evans@tu-dresden.de

[b]Centre for Systems Chemistry, Stratingh Institute for Chemistry, University of Groningen, Groningen, The Netherlands

† Electronic supplementary information (ESI) available. See DOI: 10.1039/d0fd00016g

Introduction

Transport properties of fluids in confinement are essential for both biological and artificial systems. Enhancement of diffusion with the preservation of selectivity is essential for the improvement of separation technologies,[1] particularly for membrane-based systems.[2,3] In biological systems, diffusion enhancement is primarily facilitated by pore shape agitation of the channels embedded in soft matter.[4–8] However, similar effects can also be found in artificial porous media such as carbon nanotubes in which phonon-induced oscillating friction is found to enhance diffusion of fluids.[9–11] In both cases the nanoscopic oscillation of pore contraction and expansion propagates cooperatively through the lattice allowing for accelerated transport properties on a larger length scale.

Recently, Marbach *et al.* established a general model to describe the "transport and dispersion across wiggling nanopores", which is primarily activated by thermal processes and occurs in a variety of different materials, with differing effects on diffusion properties.[12] Although this global vibration-induced diffusion enhancement in nanochannels might in principle also allow for separation of solutes as a function of their own Peclet number,[13] diffusion enhancement dictated by local stimuli-responsive dynamic molecular species in artificial systems remains largely unexplored. In fact, biological systems frequently manipulate transport properties by local dynamic mechanisms beyond the activated processes of pore shape agitation.[14–16] Transmembrane diffusion is often facilitated by enzymatic molecular machines (MMs) that allow transport against a concentration gradient with unprecedented efficiency and selectivity.[17,18]

The combination of local and global dynamic mechanisms to impact transport properties, as employed in biological systems, is expected to drastically enhance properties of artificial nanomaterials.[19] Inspired by natural systems, chemists have successfully produced artificial MMs that can act as artificial muscles[20] and also be bound to and open membranes for diffusion of guest species.[21,22] However, only a few examples show that these dynamic molecular systems can enhance diffusion in solution[23,24] and the actual effects, as well as their origin, are currently controversially discussed.[25] Similarly, for the dynamics of nanoscopic swimmers.[26] Instead, controlled rotational motion by MMs in porous systems is expected to enhance diffusion due to confinement effects.[27,28] Recently, Danowski *et al.* reported on the incorporation of 2nd generation light-driven MMs in the backbone of a porous metal–organic framework.[29] They demonstrated that the unidirectionality of rotation is maintained and that the immobilized motors exhibit rotational frequencies similar to the motors in solution. This is one of the few examples of artificial MMs employed in ordered porous solids[30] and the only example that illustrates regular spatial organization of unidirectionally rotating molecules in a porous crystal. Although rotational intramolecular motion is well known[31] also in crystalline solids,[32] stimuli-driven unidirectional rotation in light driven molecular motors represents the ability to control the frequency and directionality by molecular design.[33] Using *E*–*Z* photoisomerization of an overcrowded alkene, the rotor can be switched into a metastable state. A subsequent thermal relaxation step produces 180° rotation, where the stereocenter adjacent to the double bond dictates the directionality. Successive photoisomerisation and thermal relaxation steps lead to unidirectional 360° rotation of the rotor around

ART ■ D0FD00016G

the double bond axis (Fig. 1).[34] A broad variety of artificial light driven molecular motors with different structures, properties and functionalities were established by changing the molecular design.[35]

In this contribution, we demonstrate the interactions and transport properties of fluids in motorized porous frameworks and investigate the influence of cooperative synchronized and non-cooperative rotation of molecular motors. This study is performed by molecular dynamics simulations using a minimal toy-model, which resembles known molecular rotors. The molecular machine design incorporates elements of existing molecular motors including their geometry and hypothetical orientations in a one-dimensional pore, in an effort to establish a close representation of a real-world system. Initially, the result of an isolated motor surrounded by fluid was considered. Subsequently, different pore sizes were investigated so that the effects of confinement on the transport properties of the fluid can be captured. We also probed the influence of cooperativity on the transport properties of the confined fluid by computing systems where the rotation of two rotors are either correlated, in direction, or uncorrelated. This allows us to investigate fundamental scenarios present in materials currently known in literature[29] and compare this to proposed cooperatively working motorized frameworks.

This study provides a physical blueprint for molecular machine-containing frameworks poised as new devices by which external stimuli can act to provide activated diffusion for directional mass transport or nanoscale microfluidic devices, mimicking biological systems. The introduction of MMs into the backbone of periodic framework materials has yielded stimuli-responsive assemblies of controlled dynamics in the solid-state.[29] Although this specially defined arrangement of MMs in the solid-state represents dynamic heterogeneous interfaces, the collective synchronized work of MMs in the solid-state is unprecedented and molecular simulations, like that presented here, provide essential insight for experimental endeavours.

Methodology

MM-systems were investigated using molecular dynamics (MD) simulations, employed by the lammps code.[37] We simulate the motor as Lennard-Jones (LJ)

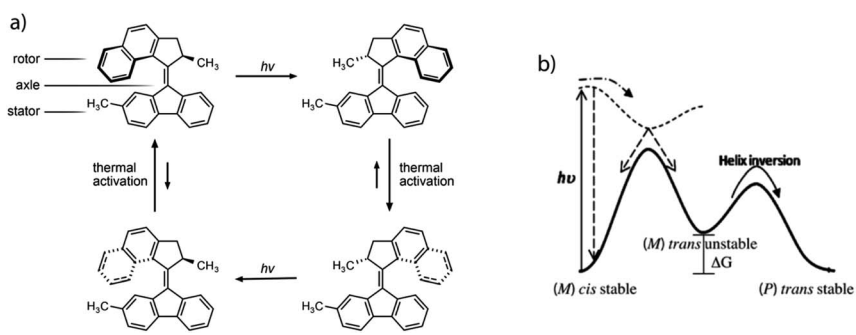

Fig. 1 The prototypical light driven molecular motor, highlighting the steps that provide rotation (a). The underlying potential energy surface for the molecule (solid line) and the excited state potential energy surface (dashed line), which induces the motion (b). Portions of this figure are reprinted from ref. 36.

ART ■ D0FD00016G

particles, which interact with surrounding LJ particles by interatomic interactions described by the classic LJ potential (eqn (1))

$$U(r) = 4\varepsilon\left[\left(\frac{\sigma}{r}\right)^{12} - \left(\frac{\sigma}{r}\right)^{6}\right] \quad (1)$$

where ε is the characteristic energy, σ represents the size of the particle and r the distance between particles. Our simulation truncates this potential at the cut-off distance 2.5σ. The simulation results are described using reduced LJ units. For simplicity, we consider particles of all the same size, mass (m) and characteristic energy for interatomic potentials ($m = 1$, $\sigma = 1$ and $\varepsilon = 1$). Temperature is described by reduced temperature, where $T^* = T\frac{k_B}{\varepsilon}$ and k_B represents the Boltzmann constant. Importantly, time is defined as $\tau = (\varepsilon/m\sigma^2)^{1/2}t$. We have employed these units here for simplicity, as the aim of this study is a qualitative assessment of molecular motor systems in confined fluids. The timestep for simulations was set to 0.005τ. The MMs were modelled by six particles with additional bond, angle and dihedral interactions computed by harmonic potentials (eqn (2)–(4)).

$$E(r) = K_{\text{bond}}(r - r_0)^2 \quad (2)$$

$$E(r) = K_{\text{angle}}(\theta - \theta_0)^2 \quad (3)$$

$$E(r) = K_{\text{dihedral}}[1 + d\cos(n\phi)] \quad (4)$$

The energy coefficients K_{bond}, K_{angle} and K_{dihedral} were set to 500ε, 300ε and 100ε, respectively. The specified geometry and thus equilibrium values of these potentials are discussed in detail later. This provides a robust and customizable framework for modelling molecular motifs.

The dynamics of the fluid, and dynamics of the MMs, were simulated using a Langevin thermostat[38] in the *NVE* ensemble, which effectively performs Brownian dynamics.[39] The temperature of the fluid was controlled to $1.0T^*$ using a damping parameter of 1.0τ. Confinement was achieved using wall potentials that interact with fluid particles using only the repulsive part of the LJ potential (eqn (1)).

Representative input files for the simulation reported in this study are available online in our data repository at https://github.com/jackevansadl/supp-data.

Results

Minimal representation of a molecular rotor

Our model drew inspiration from the prototypical 2$^{\text{nd}}$ generation molecular motor with a rotor that reassembles the structure embedded in the previously discussed motorized framework[29] (Fig. 2a). However, we sought to simplify this molecular motif using the fewest number of particles, bonds and angles and symmetrize the rotor. This led us to our first and generic model displayed in Fig. 2b and c. This model uses six particles arranged such that two particles act as the rotor (A and A′), two as the axle (B and C) and two as the stator (D and D′). Only the particles of the rotor and axle (A, A′, B and C) were chosen to noncovalently interact with surrounding LJ fluid particles with the same strength and particle

ART ■ D0FD00016G

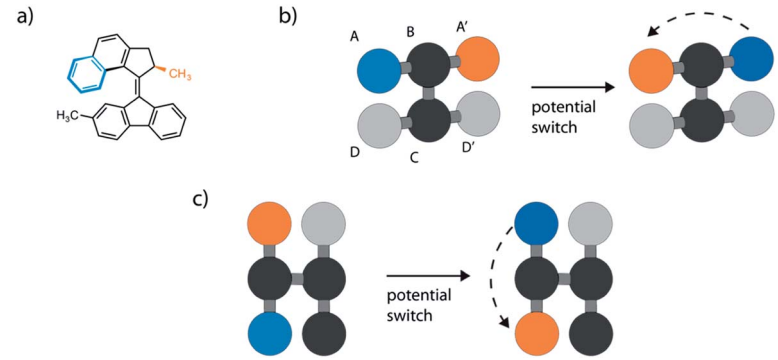

Fig. 2 The prototypical molecular motor used as motivation for this work (a). Description of the azimuthal motor (b), where particles are labelled, and the effect of the potential switch demonstrated. A similar arrangement can also be used to model an altitudinal motor (c).

size parameters as the surrounding LJ fluid, $\sigma = 1$ and $\varepsilon = 1$. These values were chosen as, generally, molecular rotors do not interact strongly with solvents and are of similar relative size. Particles D and D′ have no interactions as they are employed to define the necessary dihedral potential. Moreover, the forces and velocities of B, C, D and D′ particles were set to 0, fixing their position throughout the simulation. The key bond parameter that dictates the size of the rotor, r_0 between particles A–B and A′–B, was set to 1.5σ. Notably, this arrangement can be rotated so that both azimuthal[40] and altitudinal[41] motion can be modelled (Fig. 2c).

Simulations of the prototypical 2nd generation molecular motor have used excited-state MD simulations, where the mechanism for light-driven unidirectional rotation was investigated.[42] These simulations use expensive atomistic descriptions of the MM, which indeed are useful to provide accurate details about the free energy landscape. However, these simulations are difficult to extend in understanding long timescale dynamics. To our knowledge the consistent rotational motion of these systems using classical molecular dynamics has not been described and this is an important development for the investigation of molecular motors.[43] In the literature, the motion of other important stimuli-responsive molecular machines and switches, such as azobenzene, is typical treated by a two potential system.[44] This straightforward approach describes the two long lived states, which these molecules exhibit. Depending on the molecular structure, rotary motion of MMs might involve multiple steps, however for simplicity we will consider a bistable scenario in this work.

To dictate the photoactive motion displayed by this MM we define two potential states of the system. This uses the dihedral potential between the particles A–B–C–D and A′–B–C–D′ noted in eqn (4). This potential has the parameter d, which is set as 1 or -1. This can be changed during the simulation to produce two distinct potential states as demonstrated in Fig. 3. These potential states have a minimum at either 0° or 180°, which effectively switches the stable configuration of particles A and A′ to opposite sides of the molecule. Sequentially switching the potential parameter d during the simulation, after a set number of

ART ■ D0FD00016G

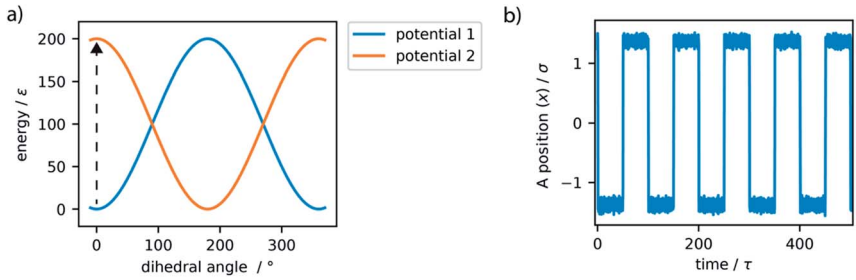

Fig. 3 The potential energy surface for the dihedral interaction in the motor system (a). Potential 1 and potential 2 refer to the two potential states and the arrow depicts the effect of switching between these states. The stepwise periodic rotation observed by switching the potential every 50τ (b). This is demonstrated by the relative x-position of the A particle, where the axle of the rotor is orientated in the z-direction.

time steps, a stepwise periodic rotation is achieved. This stepwise rotation is comparable to the type of motion observed in the experimental system. The motion between the two states occurs over a few simulation steps, which is comparable to the ultrafast dynamics reported for the excited-state photoisomerization rotation found in the experimental system.[45] Throughout this study, the switching period, between the two potentials, was chosen as 50τ. Currently, molecular rotary motors exhibit MHz-scale rotational frequencies.[46,47] If we consider the particles in this study to have similar size and characteristics to argon, the rotation rate is approximately 4.6 GHz. This is currently faster than is observed for MMs but represents the potential for such systems, as with specific functionalisation these systems could in principle function in the GHz regime.[48]

The simple switching of the dihedral potentials can effectively produce a rotation about the axes of the molecule. However, because the potential switch sets this structural configuration atop the symmetric maximum of the dihedral potential energy surface the system can equally relax (by rotation) in either direction. This results in the non-directional rotation of the motor as demonstrated in Fig. 4a. Unidirectional motion is a sought-after characteristic of molecular rotors known to work in porous frameworks.[29] However, as with biological motor systems, directionality is essential to perform mechanical tasks.[49] Synthetically this is achieved by photo-responsive sterically overcrowded alkenes, which results in four distinct steps as outlined in Fig. 1.[50] To achieve unidirectional rotation in our simulations we employ a torsional bias force, orientated in the direction of the axle, thus mimicking the influence of sterically crowded functionalisation. This use of applied torque avoids increasing complex descriptions of the dihedral potential energy surface. While large bias forces result in continued, and uncontrolled, rotation, subsequent to the potential switch event, a bias force of $30\sigma/\varepsilon$ results in singular and unidirectional rotation (Fig. 4b). Notably, the sign of this bias torque dictates the direction of rotation, either clockwise or counter clockwise allowing the control of directionality, similar to the experimental MM for which rotational directionality is dictated by the nature of the stereocentre adjacent to the double bond.[50]

As detailed here, we have demonstrated that a six-particle system can produce a minimal description of a molecular motor for classical molecular dynamics

ART ■ D0FD00016G

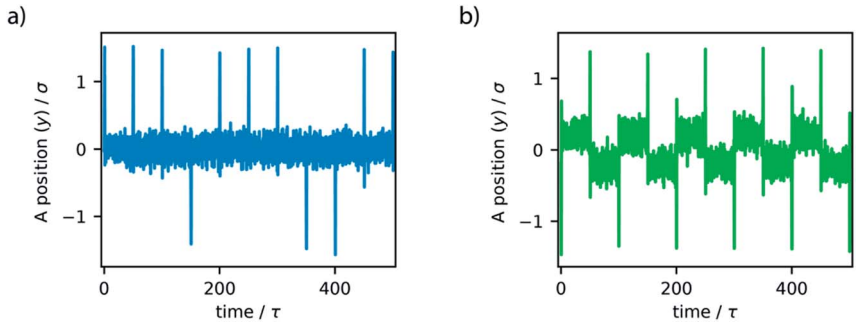

Fig. 4 The direction of rotation observed for the rotor model is demonstrated by the *y*-position of one of the rotor particles (A, for example), perpendicular to the stable orientation of the rotor, which is the *x*-direction. Non-directional rotation is demonstrated for the rotor model (a), however, the application of a bias torque results in unidirectional rotation (b).

simulations. Our model switches between two distinct dihedral potentials and when combined with a bias torque this results in unidirectional rotation. Importantly, the motion we observe is comparable to the ratchet-like rotation designed in many synthetic molecular motors.[51]

Dynamics of rotor surrounded by fluid

Initially, we investigated the results obtained by surrounding the model motor with LJ particles, which act like a fluid. The motor model, described in the previous section, was placed in a simulation box of $20\sigma \times 20\sigma \times 20\sigma$, with periodic boundary conditions. LJ particles were included in this simulation box with a density of 0.34ρ, which at $1.0T^*$ behave as a liquid.[52] Simulations where the motor remains fixed, by virtue of a consistent dihedral potential, and where the motor rotates unidirectionally were performed and system properties sampled over 4 million steps (equivalent to $20 \times 10^3\tau$). The trajectories show constant temperatures but when the potential is switched there is a spike in total energy, associated with the drastic increase in potential energy of the system. This high energy state quickly subsides as the motor rotates to the new stable configuration.

These simulations demonstrate that the global dynamics of the fluid show no changes resulting from rotation of the motor. In particular, the structure of the fluid, determined by the radial distribution function, and the dynamics of the fluid, revealed by mean-squared displacement, remain unaffected (Fig. S2, ESI†). Given the size of the molecular rotor is equivalent to the size of the fluid particles this is perhaps not surprising. To completely understand the effect of artificial molecular rotation in this system the local properties of the rotor and fluid were investigated. As displayed in Fig. 5a, the rotation produces a lower density of fluid in a spherical area directly surrounding the centre of the rotor (particle B). This local defect in the structure is attributed to the constant reorganisation of the fluid due to rotation. Moreover, the dynamics in this region also appear to be influenced by the motion. The average velocity of spherical slices surrounding the rotor (Fig. 5b) show an increase in absolute velocity. This increase is apparent in the locations where the rotor particles (A and A′) are located, suggesting that the movement of the rotor produces this increase in local velocity of the fluid.

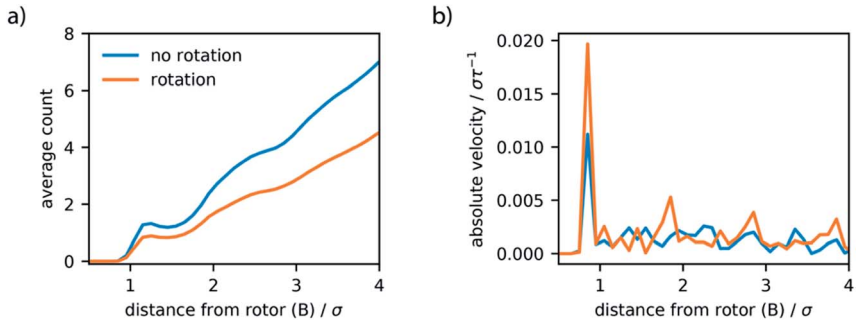

Fig. 5 Local properties of the molecular rotor model surrounded by the LJ liquid for trajectories where the rotor is fixed and rotates. The average number of LJ fluid particles for spherical shell segments, centred at the centre of the rotor particles (a). Absolute velocity for the same spherical shell segments (b).

Clearly the relatively small size of the molecular rotor limits its influence on the properties of a surrounding medium, which is known to influence the rotational speed of light driven motors[52,53] and rotors.[53–55] The effects of the motor rotation and its frequency are neglected in this model but are expected to play an important role in a real world system. By increasing the rotor size the interactions with surrounding fluid could be enhanced, allowing in principle for molecular stirring.[23]

Azimuthal rotor in a one-dimensional pore

One appealing method to increase the effectiveness of molecular machines is their positions within materials.[56] Especially confining a reaction media in close proximity to the motion of rotors is expected to enhance dynamic effects.[27] We consider the effect of this by arranging our motor system on the walls of a one-dimensional pore (Fig. 6a). The pore is constructed using repulsive wall potentials that interact with only fluid particles. This confinement arrangement is analogous to simulations of nanoconfined water, and

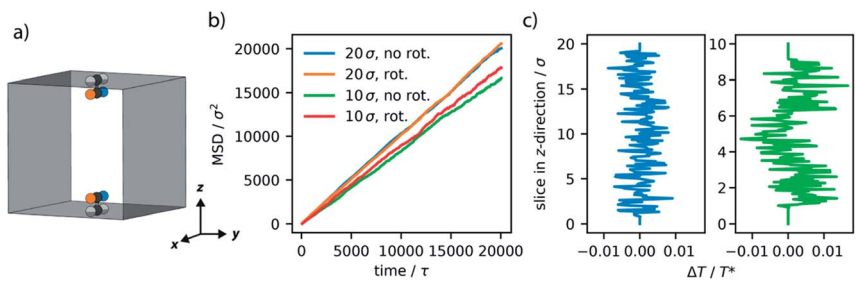

Fig. 6 One-dimensional pore system with azimuthal rotors (a). Mean-squared displacement (MSD) of the confined fluid for the large and small pores (b) with the motors fixed (no rot.) or with unidirectional rotation (rot.). Average change in temperature for the trajectories with and without rotation (c) for the large pore (blue) and small pore (green) computed for one-dimensional slices of the simulation box in the z-direction (perpendicular to the direction of the pore).

these repulsive walls are suggested to act like hydrophobic walls.[57] Two azimuthal rotors were positioned on opposite walls and arranged such that the stable configuration of the rotor is aligned with the one-dimensional pore. Unidirectional rotation is directed with the bias torque in the same direction for each rotor. The LJ fluid was added to this system at a density of 0.09ρ. A lower density was employed to avoid over saturation. Importantly, two distinct pore sizes were investigated, a larger pore of $20\sigma \times 20\sigma$ and a smaller pore of $10\sigma \times 10\sigma$. The axis of the one-dimensional pore was 20σ and includes periodic boundary conditions, only in this dimension. Simulation results are presented as averaged observations from 10 unique samples, each included 4 million steps, as described in the previous section.

We find that for the large pore system the global and local properties of the confined fluid (Fig. 6b and c) show little influence from rotation. The transport of the fluid is observed as the slope of the mean-squared displacement, also referred to as diffusivity (Fig. 6b). There appears to be little influence on the transport of the fluid for this larger pore structure. Similarly, there are no local increases in the average motion (temperature) observed (Fig. 6c).

In contrast to the larger pore, the smaller pore structure of $10\sigma \times 10\sigma$, which approaches the length of the rotor (3σ), demonstrated a considerable effect from the set motion of the molecular motor. As a result of the increased confinement the diffusivity of the fluid decreases by approximately 15%, in agreement with our understanding of diffusion in porous media.[58] However, if the motors rotate there is an evident increase in diffusivity where the smaller pores now only result in a 10% decrease in diffusivity. The greater confinement provided by the smaller pore size greatly enhances the effect of the motor's rotation on the LJ fluid. Particularly, the analysis of the average local properties of the fluid demonstrates an increase in local temperature at the location of the rotors. This enhanced temperature in the area directly surrounding the rotor is representative of the convection-like processes that have been experimentally observed to produce enhanced diffusion in molecular catalysts.[25]

Altitudinal rotor in a one-dimensional pore

The synthetic design of molecular motors can hypothetically produce rotors that rotate in distinctive directions. When immobilized on a surface these motors can exhibit different orientations.[59] As a result, we also have considered if rotation of the motor is arranged in an altitudinal fashion,[60] as illustrated in Fig. 2c. This arrangement can localize the specified motion towards the centre of a porous structure where it may have a greater influence on the transport properties. An equivalent one-dimensional pore system was constructed for investigating the use of altitudinal rotors (Fig. 7a) which includes two motors orientated perpendicular to the pore direction, such that the rotation is orientated in the direction of diffusion. The unidirectional rotation for this case is also arranged with the bias torque in the same direction for each rotor. The sampling and simulation details are analogous to that discussed for the azimuthal case.

Similar to the system containing azimuthal motors, we observe no discernible influence from the motor rotation in the large pore structures. Moreover, for the small pore structures, where the positions of the rotor particles are in close proximity there is also the same relative decrease in diffusion.

ART ■ D0FD00016G

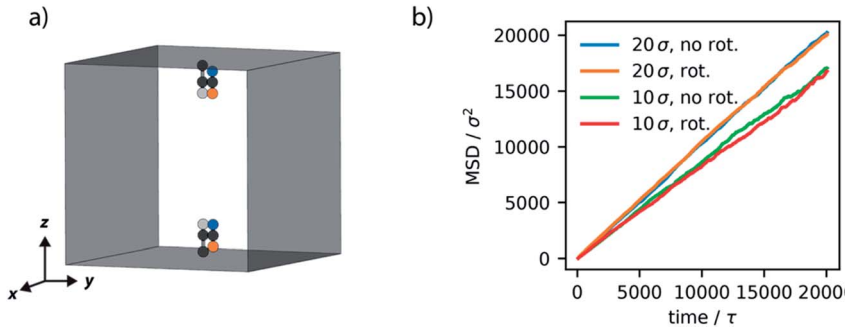

Fig. 7 One-dimensional pore system with altitudinal rotors (a). Mean-squared displacement (MSD) of the confined fluid for the large and small pores (b) with the motors fixed (no rot.) or with unidirectional rotation (rot.).

When the motors rotate, however, we observe no significant change in diffusivity, in direct contrast to that observed for the azimuthal rotor system. This result suggests that only specific orientations of rotation by molecular motors aligned in pore channels may lead to an increase in transport properties.

Non-directional rotation in a one-dimensional pore

The unidirectional motion of molecular rotors is considered imperative for directing movement at the molecular level. Thus, we sought to consider how non-directional motion manifests and effects diffusion in small pore systems, for both the azimuthal and altitudinal rotors. In fact, such a case resembles the scenario of rotors frequently incorporated in the backbone of porous frameworks but not governed by a stimulus, such as light.[28] To investigate this, we conducted similar simulations as described in the previous two sections, but with the absence of the bias torque. This resulted in non-directional motion of the rotors (Fig. 8).

Without the application of bias force, the rotation is observed to consecutively oscillate in random directions, clockwise or anti-clockwise. The presence and dynamics of the confined LJ liquid is not observed to produce unidirectional or preferred directional rotation of the rotors. Non-directional motion of the azimuthal rotor resulted in equivalent diffusivity as the unidirectional motion previously described. Contrastingly, the altitudinal rotor showed enhanced diffusivity, greater than both the considered unidirectional and fixed rotor dynamics (6% greater than the fixed rotor case). This non-directional motion can provide the altitudinal system with the same diffusivity as the azimuthal system.

The altitudinal rotor system, as it extends into the pore, demonstrates the profound influence of the directionality of the motor. The motion of each rotor can interact like that of a turnstile, where rotation in a cooperative manner, if not directed favourably, can hinder diffusion.

Directional and cooperative rotation

As the directionality, and hence cooperativity, of the motors in this small pore structure can affect the transport properties of the confined fluid we examined different combinations of rotation and their effect on the directionality of the

ART ■ D0FD00016G

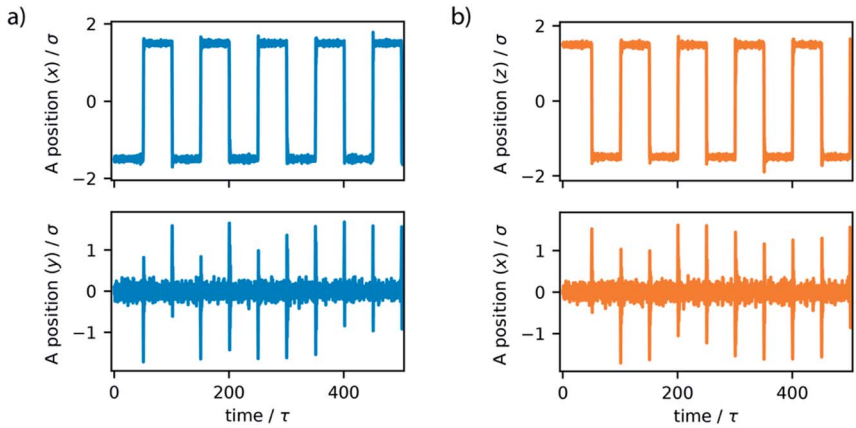

Fig. 8 The direction of rotation observed for the azimuthal (a) and altitudinal (b) rotor models is demonstrated by the *y*-position of one of the rotor particles (A, for example), perpendicular to the stable orientation of the rotor, which is the *x*-direction.

diffusion in the small pore, for both orientations of the motor. Please note the frequencies of rotation are aligned, here we only investigate the direction. We considered six different cases: fixed rotors, non-directional rotors and the four combinations of clockwise or anti-clockwise rotation. We label the direction of rotation by the sign of the bias torque (Fig. 9a).

The alignment of azimuthal motors with the pore walls shows no distinct direction of diffusivity, with the average displacement close to centre, around 0σ. This indicates equal diffusion in either direction of the one-dimensional pore. Notably, this is not affected by different combinations of rotation by the motors. The altitudinal motors, however, exhibit important dependence on the set rotation of the motors. If the rotors have no rotation (fixed), non-directional rotation or aligned rotation the LJ fluid is observed to show no directional preference. The cooperative, and opposite, rotation of each motor, labelled here as "+−" and "−+"

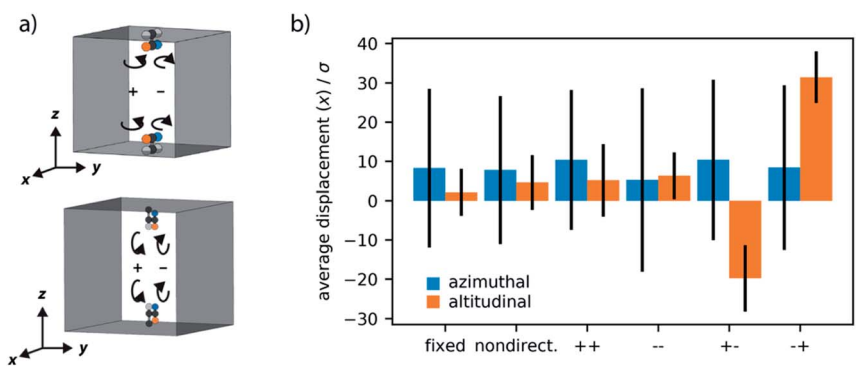

Fig. 9 Illustration of the different rotational directions considered for the azimuthal and altitudinal motors arranged in a one-dimensional pore (a). The average displacement of the LJ fluid in the direction of the pore, *x*-direction, for different combinations of rotational directions for each of the rotors, where the standard deviation is depicted by lines (b).

ART ■ D0FD00016G

can induce a preferential direction to the diffusion of confined fluid. This turnstile-like system can produce a flow of fluid in either direction in the pore dependent on the combination of rotations used.

Although the magnitude of diffusion is only marginally affected by the arrangement of motors, for example we have not demonstrated on/off switchable diffusion, the induction of a preferential diffusion direction is certainly promising. Notably, the rotors used here are of relative size to the diffusing LJ particles and of equal interaction strength. It is the effect of cooperativity and confinement that is responsible for this significant outcome on the global transport properties. Amplification of these effects are expected to occur if the average rotor–fluid interactions as well as the confinement effects are optimized. An increase in motor density per void volume is certainly also expected to enhance the observed diffusion effects.

Discussion

The molecular simulations, described in this study, represents a minimalist and qualitative picture of molecular motors, and the possible consequence of arranging them in confined solid-state. Many approximations are made to describe the motion of rotors in this study. For example, the rotation mechanism is significantly reduced to a two-state motion. Notably, the rotation between the two-states occurs almost instantaneously, when the dihedral potential is switched. In reality molecular motors show complex rotational dynamics with slow and fast movements to produce a full rotation.[49] In future studies, it is possible to use more complex potential energy surfaces and gradual potential changes to more realistically reflect the intricate dynamics of real-world motors. Nevertheless, the potential switching mechanism should provide the foundation to build new atomistic models of molecular machines.

A key observation from considering the combined dynamics of the rotor surrounded by fluid is the impervious nature of the fluid bulk. The small rotor system is a drop in the ocean compared to the stable dynamics of a fluid. This is clear from the global properties remaining unaffected by rotational dynamics, while only the very local properties, for example the particles in the arc of rotation, show some evidence of change. This observation is in line with recent scepticism about diffusion enhancement by dynamic species in diluted solutions.[25] In turn, this demonstrates the importance of regular, defined arrangement with a maximal high motor density of these machines in confinement. It was only when the fluid was confined in a pore of comparable size to the molecular rotor where the applied rotation began to affect the global transport properties of the fluid. Still, in our initial model we find relatively modest changes to diffusivity. However, by considering the orientation of the motor and the effect of different rotations of rotors we find the greatest change. By combination of altitudinal rotors aligned into the pore and synchronization of the rotational directionality we could produce a turnstile-like system able to direct the diffusion in a specified direction of the pore. This illustrates that random orientation and non-directional rotation of molecular motors in the solid-state are unlikely to produce diffusion enhancement on a larger length scale let alone directed diffusion. Cooperative rotation and specific arrangement of unidirectional rotation are required to produce designed transport phenomena.

ART ■ D0FD00016G

Summary and outlook

In this work, we have outlined the influence of rotating molecular species and the importance of their orientation, cooperativity and directionality on the transport properties of confined fluids. Our findings help to understand the influence of local dynamics of molecular motors and rotors on the surrounding fluid. This includes, the nature of pore space functionalized with dynamic groups and potential strategies to manipulate transport properties of confined fluids by this dynamic pore space. Although the applied model drastically simplifies real-world molecular motors, it captures the most important aspects being unidirectional rotation and orientation of the rotor. Our results, however, provide helpful indications about the need for high rotational frequencies in addition to the detection of minor changes in diffusivity locally and globally. We envision the guidelines, presented here, to be crucial for the design of stimuli-responsive dynamic materials, capable of manipulating guest transport properties by dynamic molecular machines. However, the currently reported porous materials that include molecular machines[30] or rotors[28] do not meet the specified criteria defined by this investigation.

As discussed in the introduction, many transport phenomena are supported by activated vibrations of the pore walls,[12] a property neglected in the present work. The combination and alignment of local dynamics from a functional surface, by anchored groups, and global vibrational dynamics of the framework backbone, towards cooperative pore agitation on different length scales, represents an interesting avenue for novel transport phenomena in porous solids and should be further explored.

Conflicts of interest

There are no conflicts to declare.

Acknowledgements

J. D. E. acknowledges the support of the Alexander von Humboldt foundation and HPC platforms provided by a GENCI grant (A0010807069) and the Center for Information Services and High Performance Computing (ZIH) at TU Dresden. We thank Michael Kathan for critical reading and comments on a draft of this paper.

References

1 D. S. Sholl and R. P. Lively, *Nature*, 2016, **532**, 435–437.
2 M. S. Denny, J. C. Moreton, L. Benz and S. M. Cohen, *Nat. Rev. Mater.*, 2016, **1**, 16078.
3 S. Yuan, X. Li, J. Zhu, G. Zhang, P. Van Puyvelde and B. Van der Bruggen, *Chem. Soc. Rev.*, 2019, **48**, 2665–2681.
4 A. J. Wand, *Nat. Struct. Biol.*, 2001, **8**, 926–931.
5 S. Y. Noskov, S. Bernèche and B. Roux, *Nature*, 2004, **431**, 830–834.
6 G. Bhabha, J. Lee, D. C. Ekiert, J. Gam, I. A. Wilson, H. J. Dyson, S. J. Benkovic and P. E. Wright, *Science*, 2011, **332**, 234–238.
7 T. W. Allen, S. Kuyucak and S.-H. Chung, *Biophys. J.*, 1999, **77**, 2502–2516.

8 G. Wei, W. Xi, R. Nussinov and B. Ma, *Chem. Rev.*, 2016, **116**, 6516–6551.
9 M. Ma, G. Tocci, A. Michaelides and G. Aeppli, *Nat. Mater.*, 2016, **15**, 66–71.
10 E. R. Cruz-Chú, E. Papadopoulou, J. H. Walther, A. Popadić, G. Li, M. Praprotnik and P. Koumoutsakos, *Nat. Nanotechnol.*, 2017, **12**, 1106–1108.
11 M. Ma, F. Grey, L. Shen, M. Urbakh, S. Wu, J. Z. Liu, Y. Liu and Q. Zheng, *Nat. Nanotechnol.*, 2015, **10**, 692–695.
12 S. Marbach, D. S. Dean and L. Bocquet, *Nat. Phys.*, 2018, **14**, 1108–1113.
13 S. Marbach and L. Bocquet, *J. Chem. Phys.*, 2017, **147**, 154701.
14 N. Gamper and M. S. Shapiro, *Nat. Rev. Neurosci.*, 2007, **8**, 921–934.
15 S. G. Dahl, I. Sylte and A. W. Ravna, *J. Pharmacol. Exp. Ther.*, 2004, **309**, 853–860.
16 H. F. Lodish, *Molecular cell biology*, W. H. Freeman and Co., New York, 2013.
17 C. R. Sanders and J. M. Hutchison, *Curr. Opin. Struct. Biol.*, 2018, **51**, 80–91.
18 F. M. Goñi, *Biochim. Biophys. Acta, Biomembr.*, 2014, **1838**, 1467–1476.
19 B. A. Grzybowski and W. T. S. Huck, *Nat. Nanotechnol.*, 2016, **11**, 585–592.
20 J. Chen, F. K.-C. Leung, M. C. A. Stuart, T. Kajitani, T. Fukushima, E. van der Giessen and B. L. Feringa, *Nat. Chem.*, 2018, **10**, 132–138.
21 V. García-López, F. Chen, L. G. Nilewski, G. Duret, A. Aliyan, A. B. Kolomeisky, J. T. Robinson, G. Wang, R. Pal and J. M. Tour, *Nature*, 2017, **548**, 567–572.
22 M. A. Watson and S. L. Cockroft, *Chem. Soc. Rev.*, 2016, **45**, 6118–6129.
23 J. Chen, J. C. M. Kistemaker, J. Robertus and B. L. Feringa, *J. Am. Chem. Soc.*, 2014, **136**, 14924–14932.
24 K. K. Dey, F. Y. Pong, J. Breffke, R. Pavlick, E. Hatzakis, C. Pacheco and A. Sen, *Angew. Chem., Int. Ed.*, 2016, **55**, 1113–1117.
25 T. S. C. MacDonald, W. S. Price, R. D. Astumian and J. E. Beves, *Angew. Chem., Int. Ed.*, 2019, **58**, 18864–18867.
26 K. K. Dey, *Angew. Chem., Int. Ed.*, 2019, **58**, 2208–2228.
27 H. Huang and T. Aida, *Nat. Nanotechnol.*, 2019, **14**, 407.
28 A. Gonzalez-Nelson, F.-X. Coudert and M. A. van der Veen, *Nanomaterials*, 2019, **9**, 330.
29 W. Danowski, T. van Leeuwen, S. Abdolahzadeh, D. Roke, W. R. Browne, S. J. Wezenberg and B. L. Feringa, *Nat. Nanotechnol.*, 2019, **14**, 488–494.
30 P. Martinez-Bulit, A. J. Stirk and S. J. Loeb, *Trends in Chemistry*, 2019, **1**, 588–600.
31 G. S. Kottas, L. I. Clarke, D. Horinek and J. Michl, *Chem. Rev.*, 2005, **105**, 1281–1376.
32 C. S. Vogelsberg and M. A. Garcia-Garibay, *Chem. Soc. Rev.*, 2012, **41**, 1892–1910.
33 N. Koumura, R. W. J. Zijlstra, R. A. van Delden, N. Harada and B. L. Feringa, *Nature*, 1999, **401**, 152–155.
34 T. van Leeuwen, A. S. Lubbe, P. Štacko, S. J. Wezenberg and B. L. Feringa, *Nat. Rev. Chem.*, 2017, **1**, 0096.
35 S. Kassem, T. van Leeuwen, A. S. Lubbe, M. R. Wilson, B. L. Feringa and D. A. Leigh, *Chem. Soc. Rev.*, 2017, **46**, 2592–2621.
36 R. D. Astumian, *Chem. Sci.*, 2017, **8**, 840–845.
37 S. Plimpton, *J. Comput. Phys.*, 1995, **117**, 1–19.
38 T. Schneider and E. Stoll, *Phys. Rev. B: Condens. Matter Mater. Phys.*, 1978, **17**, 1302–1322.

ART ■ D0FD00016G

39 M. P. Allen, M. P. Allen, D. J. Tildesley, T. Allen and D. J. Tildesley, *Computer Simulation of Liquids*, Clarendon Press, 1989.

40 R. A. van Delden, M. K. J. ter Wiel, M. M. Pollard, J. Vicario, N. Koumura and B. L. Feringa, *Nature*, 2005, **437**, 1337–1340.

41 G. T. Carroll, G. London, T. F. Landaluce, P. Rudolf and B. L. Feringa, *ACS Nano*, 2011, **5**, 622–630.

42 S. Grimm, C. Bräuchle and I. Frank, *ChemPhysChem*, 2005, **6**, 1943–1947.

43 A. Singharoy and C. Chipot, *J. Phys. Chem. B*, 2017, **121**, 3502–3514.

44 C. Pezzato, C. Cheng, J. F. Stoddart and R. D. Astumian, *Chem. Soc. Rev.*, 2017, **46**, 5491–5507.

45 J. Conyard, K. Addison, I. A. Heisler, A. Cnossen, W. R. Browne, B. L. Feringa and S. R. Meech, *Nat. Chem.*, 2012, **4**, 547–551.

46 M. Klok, N. Boyle, M. T. Pryce, A. Meetsma, W. R. Browne and B. L. Feringa, *J. Am. Chem. Soc.*, 2008, **130**, 10484–10485.

47 M. M. Pollard, M. Klok, D. Pijper and B. L. Feringa, *Adv. Funct. Mater.*, 2007, **17**, 718–729.

48 B. Oruganti, C. Fang and B. Durbeej, *Phys. Chem. Chem. Phys.*, 2015, **17**, 21740–21751.

49 V. García-López, D. Liu and J. M. Tour, *Chem. Rev.*, 2020, **120**, 79–124.

50 D. Roke, S. J. Wezenberg and B. L. Feringa, *Proc. Natl. Acad. Sci. U. S. A.*, 2018, **115**, 9423–9431.

51 S. Erbas-Cakmak, D. A. Leigh, C. T. McTernan and A. L. Nussbaumer, *Chem. Rev.*, 2015, **115**, 10081–10206.

52 B. Smit, *J. Chem. Phys.*, 1992, **96**, 8639–8640.

53 J. C. M. Kistemaker, A. S. Lubbe, E. A. Bloemsma and B. L. Feringa, *ChemPhysChem*, 2016, **17**, 1819–1822.

54 M. Klok, L. P. B. M. Janssen, W. R. Browne and B. L. Feringa, *Faraday Discuss.*, 2009, **143**, 319–334.

55 A. Vyšniauskas and M. K. Kuimova, *Int. Rev. Phys. Chem.*, 2018, **37**, 259–285.

56 E. Moulin, L. Faour, C. C. Carmona-Vargas and N. Giuseppone, *Adv. Mater.*, 1906036.

57 P. Kumar, F. W. Starr, S. V. Buldyrev and H. E. Stanley, *Phys. Rev. E: Stat., Nonlinear, Soft Matter Phys.*, 2007, **75**, 011202.

58 K. Malek and M.-O. Coppens, *J. Chem. Phys.*, 2003, **119**, 2801–2811.

59 V. Balzani, A. Credi and M. Venturi, *ChemPhysChem*, 2008, **9**, 202–220.

60 G. London, G. T. Carroll, T. Fernández Landaluce, M. M. Pollard, P. Rudolf and B. L. Feringa, *Chem. Commun.*, 2009, 1712–1714, DOI: 10.1039/b821755f.

Faraday Discussions

Cite this: DOI: 10.1039/d0fd00025f

PAPER

Atomistic insight into the flexibility and heat transport properties of the stimuli-responsive metal–organic framework MIL-53(Al) for water-adsorption applications using molecular simulations†

Aran Lamaire, ‡ Jelle Wieme, ‡ Alexander E. J. Hoffman and Veronique Van Speybroeck *

Received 23rd February 2020, Accepted 12th March 2020
DOI: 10.1039/d0fd00025f

To exploit the full potential of metal–organic frameworks as solid adsorbents in water-adsorption applications, many challenges remain to be solved. A more fundamental insight into the properties of the host material and the influence that water exerts on them can be obtained by performing molecular simulations. In this work, the prototypical flexible MIL-53(Al) framework is modelled using advanced molecular dynamics simulations. For different water loadings, the presence of water is shown to affect the relative stability of MIL-53(Al), triggering a phase transition from the narrow-pore to the large-pore phase at the highest considered loading. Furthermore, the effect of confinement on the structural organisation of the water molecules is also examined for different pore volumes of MIL-53(Al). For the framework itself, we focus on the thermal conductivity, as this property plays a decisive role in the efficiency of adsorption-based technologies, due to the energy-intensive adsorption and desorption cycles. To this end, the heat transfer characteristics of both phases of MIL-53(Al) are studied, demonstrating a strong directional dependence for the thermal conductivity.

1 Introduction

For more than two decades, metal–organic frameworks (MOFs) have been investigated for their exceptional adsorption properties. Today, these porous, hybrid inorganic–organic crystalline frameworks still hold a lot of potential for a wide range of adsorption technologies in fields related to sustainable energy storage and the reduction of the greenhouse effect.[1–4] Water-adsorption

Center for Molecular Modeling, Ghent University, Tech Lane Ghent Science Park Campus A, Technologiepark 46, 9052 Zwijnaarde, Belgium. E-mail: Veronique.VanSpeybroeck@UGent.be

† Electronic supplementary information (ESI) available: Additional information on the force field and extra figures regarding the molecular dynamics simulations. See DOI: 10.1039/d0fd00025f

‡ Both authors contributed equally to this work.

applications are one of the many promising possibilities for the use of MOFs as advanced solid adsorbents.[5–9] Water-stable MOFs could, for instance, find use in adsorption-driven heat pumps or chillers,[10–15] and in atmospheric water harvesting.[16–19]

However, just as for all applications involving repeated adsorption processes, the heat management in water-adsorption applications poses an important engineering challenge. Insight into the thermal transport characteristics of MOFs is therefore essential, as their efficiency as adsorbents is strongly reduced when the temperature of the system increases, thus requiring proper control over the heat released by adsorption. This not only holds for storage tanks, in which the slow dissipation of heat could hinder the tank-filling cycles, but also for heat pumps, in which heat should be transferred rapidly to the surroundings. External heat exchangers or more conductive MOF composites could be developed to meet these requirements, but this comes at a cost.[20–23] As the thermal conductivity of MOFs is very complicated to measure accurately,[24–28] relatively few experimental studies have discussed the importance of the intrinsic heat dissipation in MOFs, so that mainly computational investigations have provided explanations for their low thermal conductivities.[29–36] Nevertheless, for most MOFs, reference data is still lacking in the literature.[28,36] In this work, the thermal conductivity of MIL-53(Al) was simulated.[37] MIL-53(Al) is a bistable material that possesses a narrow-pore (np) and a large-pore (lp) phase (Fig. 1) and is known for its anisotropic mechanical and thermal properties.[38,39] For practical applications, quantification of the anisotropy in the heat transfer is required as it can affect the design and operation of certain devices.[40] In this proof-of-principle study for the flexible MIL-53(Al) framework, we show that the intrinsic thermal conductivity of the framework differs between its (meta)stable states, which might be exploited in nanoscale applications that require precise control over the thermal conductivity *via* external stimuli, such as temperature and pressure.[41–43]

These stimuli, alongside guest adsorption, can trigger the intrinsic flexibility of MIL-53(Al), resulting in a reversible structural transformation[44–47] that can contribute to the internal heat management during the adsorption process, as the heat of adsorption is partially used to overcome the energetic barrier between the different phases.[48,49] In other words, by carefully selecting a MOF exhibiting a reversible phase transition in the desired adsorption range, it becomes possible

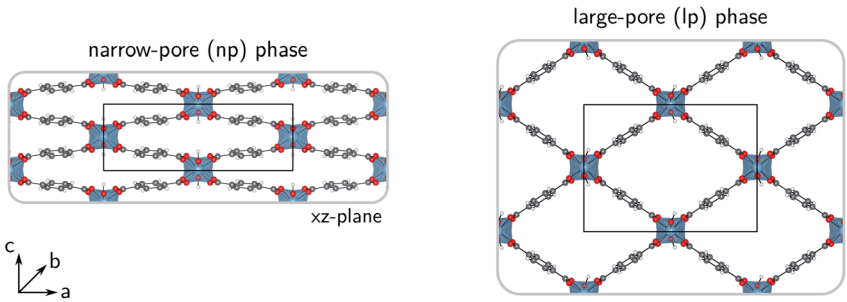

Fig. 1 Molecular representations of the narrow-pore (np) and the large-pore (lp) phases of MIL-53(Al). The *a*-, *b*- and *c*-directions are indicated together with the conventional unit cells in the *ac*-plane.

ART ■ D0FD00025F

to lower the overall amount of heat released in the adsorption process in comparison to a material without a phase transition.

However, designing a MOF with a reversible phase transition in the relevant adsorption window is a nontrivial task. Experimentally, this is accompanied by a high degree of trial and error, as the underlying thermodynamic potential cannot be directly accessed.[46] Despite the abundance of adsorption studies in MOFs, only a limited number of theoretical studies have investigated the critical effect that guest molecules can have on the phase stability.[46,50,51] Some of the present authors recently demonstrated that standard computational considerations typically do not suffice for these complex materials, as long-range dispersion interactions and correlated atomic motion might play an important qualitative and quantitative role in the description of these stimuli-responsive MOFs.[52,53] In this work, the validity of another typical approximation – *i.e.* the neglect of nuclear quantum effects in the simulations[54] – is tested for the modelling of guest-induced phase transitions.

We chose the rather extreme case of water in MIL-53(Al), where large nuclear quantum effects could be expected.[55] This particular framework is known to be moderately stable with respect to water[56,57] and the presence of water in MIL-53 materials has already been computationally explored in the past.[51,58–61] Furthermore, MIL-53(Al) variants with different organic linkers (*e.g.* MOF-303 and A520) have been investigated specifically for water-adsorption applications.[11,19] In this contribution, the phase stability of MIL-53(Al) in the presence of water is discussed, alongside the possible influence of neglecting nuclear quantum effects. Finally, we also try to obtain molecular-level insight into the water structure inside the pores, which is currently an active field of research for water-stable MOFs.[58,60,62–65]

Using advanced molecular simulation tools on the prototypical flexible material MIL-53(Al), this work thus considers two important fundamental issues strongly related to water-adsorption applications of MOFs: (1) the phase stability and the water structure inside the pores of a stimuli-responsive MOF and (2) the anisotropic thermal conductivity properties of the adsorbent.

2 Methodology

2.1 Force field

To model the potential energy surface of MIL-53(Al), a force field is used, as the computational cost of first-principles methods is currently too high to extract the properties under investigation. This force field was generated with our in-house developed QuickFF protocol for deriving force fields from first-principles input.[66,67] In this way, we approximate the quantum mechanical potential energy surface in the neighbourhood of the equilibrium structure – which is defined by the optimized geometry and the Hessian at the PBE+D3(BJ) level of theory[68–70] – using a combination of analytical covalent, electrostatic, and van der Waals force field terms. The covalent interactions are written in terms of bonds, bends, out-of-plane distances, and dihedral angles, and contain both anharmonic terms and cross terms. Minimal Basis Iterative Stockholder (MBIS) charges are used to describe the electrostatic potential between Gaussian charge distributions centered on the nuclei.[71] The van der Waals interactions were modeled by the MM3-Buckingham model[72] up to a finite cutoff of 12 Å and were supplemented with tail corrections.[73] This particular force field was specifically constructed to

ART ■ D0FD00025F

accurately model structural, vibrational, mechanical, and thermal properties, and corresponds with the MCAM force field discussed in ref. 67. More details regarding the force field energy expression can be found in the ESI (Section S1†).

For the simulations of MIL-53(Al) including water, the q-TIP4P/F[74] force field was used to describe the water molecules. This force field was derived by Habershon *et al.* from the well-known TIP4P/2005 model[75] and extended to include both flexibility and anharmonicity. The O–H stretch is described by a quartic potential, whereas the H–O–H bond angle is described by a harmonic potential (see ESI Section S1†). Similar to the rigid TIP4P/2005 model, the non-covalent interactions are modeled using four interaction sites, assigning an additional interaction site M to every water molecule, which is located at the bisector of the H–O–H angle. For the van der Waals interactions, described by a Lennard-Jones potential, only the oxygen atoms yield a non-zero contribution. The interactions between the water molecules and the framework can also be modeled by a Lennard-Jones potential, using the Lorentz–Berthelot mixing rules for the rescaled MM3 parameters of the framework: $\sigma_{LJ} = 2^{5/6}\sigma_{MM3}$, which ensures that the minima of both potentials occur at the same internuclear distance.

Complementary to the van der Waals interactions, only the H atoms and M sites of the water molecules yield contributions to the electrostatic interactions, as the oxygen atoms do not bear a charge. By placing the negative charge on the M site rather than on the oxygen atom, a better mean-field description of the polarization of the water molecules can be obtained. Although a more rigorous inclusion of electronic polarization might enhance the description of the interactions between the framework and the guest molecules, especially when making the framework polarizable as shown by Cirera *et al.*,[59] it is by no means trivial to make the extension to fully polarizable force fields. Therefore, explicit electronic polarization is commonly not taken into account when studying water in confinement.[62,63] In spite of these limitations of a mean-field description of the polarization, this water model does allow us to describe hydrogen bonding effects, as discussed in the ESI (Section S1†).

Finally, the q-TIP4P/F force field was also tailored for use in quantum simulations, making use of path integral molecular dynamics (PIMD)[54] instead of classical molecular dynamics (MD), thereby exchanging the classical treatment of the atomic nuclei with a quantum mechanical one. Given the importance of an accurate description of the low mass protons, as they play a pivotal role in the behaviour of water, proper inclusion of nuclear quantum effects (NQEs), such as the zero-point energy of the nuclei, is required.

2.2 Construction of the Helmholtz free energy profiles

The flexibility of MIL-53(Al) is investigated using the thermodynamic protocol discussed in ref. 46, starting from MD simulations in the (N, V, $\sigma_a = 0$, T) ensemble for a set of volumes. From these simulations, which were carried out at temperatures of 100 K and 300 K, the pressure profile $P(V)$ is extracted (Fig. S2†), from which the Helmholtz free energy profile $F(V)$ can be obtained as a function of the volume V for each temperature *via* thermodynamic integration.

The classical MD simulations are performed with Yaff,[76] using a Verlet time step of 0.5 fs. The temperature is controlled by a Nosé–Hoover chain thermostat[77–79] containing three beads with a relaxation time of 0.1 ps, while the pressure

ART ■ D0FD00025F

is controlled by a Martyna–Tuckerman–Tobias–Klein barostat[80,81] using a relaxation time of 1 ps.

To examine the influence of nuclear quantum effects (NQEs), PIMD simulations[54] are performed on the same volume grid and for the same temperatures. Applying PIMD on large structures such as MOFs is challenging due to the large computational cost that is associated with it, but it is necessary for a correct quantitative description of different properties, such as the thermal expansion and the heat capacity.[82,83] The PIMD simulations were performed with i-PI,[84,85] which delegates the evaluation of the forces to external codes. In this case, the covalent interactions are computed by Yaff[76] and the long-range interactions are evaluated using LAMMPS for ring-polymers containing 32 beads.[86] To control the temperature, a PILE-L thermostat[87] is applied to the system and a white noise Langevin thermostat[88] is applied to the cell. To control the pressure, a modified path-integral version of the Raiteri–Gale–Bussi barostat[84,89] is used to sample the $(N, V, \sigma_a = 0, T)$ ensemble. The time constants of the thermostats and the barostats are respectively 0.1 and 0.25 ps. A BAOAB type[90] scheme is used to integrate the equations of motion.

Both classical and path integral MD simulations were performed with and without water in the pores, considering three different loadings, *i.e.* 2.5, 7.5, and 22.5 water molecules per conventional unit cell. All the simulations related to the calculation of Helmholtz free energy profiles were performed on a $1 \times 2 \times 1$ supercell, containing 152 framework atoms including 8 aluminium atoms.

2.3 Thermal conductivity

The Green–Kubo approach[91,92] was used in combination with classical MD simulations to determine the thermal conductivity. This formalism is based on the fluctuation–dissipation theorem and states that the thermal conductivity κ can be computed by integrating the heat current autocorrelation function (HCACF) over time:

$$\kappa_{ii} = \frac{1}{k_B V T^2} \int_0^{+\infty} \mathrm{d}t \langle J_i(t) J_i(0) \rangle. \quad (1)$$

An advantage of this method is that the heat current J_i ($i = x, y,$ or z) – and thus κ_{ii} – can be simultaneously extracted in all directions from one set of simulations.

This method has been used previously by some of the present authors to compute the thermal conductivity of various well-known MOFs, such as UiO-66, HKUST-1, and MOF-5, at their equilibrium volume.[36] In this work, we computed the thermal conductivity of MIL-53(Al) for different unit cell volumes ranging from 750 Å^3 to 1500 Å^3 in steps of 50 Å^3. To this end, a series of one hundred independent simulations per volume point were conducted. First, a hundred starting structures were extracted from MD snapshots taken every 5 ps from an equilibrated classical MD simulation in the $(N, V, \sigma_a = 0, T)$ ensemble at 300 K using a $1 \times 2 \times 1$ supercell (*i.e.* a conventional cell elongated along the Al(OH) chain) in Yaff.[76] These structures were subsequently converted to $7 \times 8 \times 7$ supercells containing 29 792 atoms, as this is necessary to limit finite size effects.[93] Finally, classical MD simulations are performed with LAMMPS[86] to equilibrate the supercells at 300 K for 375 ps in the (N, V, h_0, T) ensemble and for 125 ps in the (N, V, E) ensemble. The

ART ■ D0FD00025F

HCACF is thereafter collected during one hundred 3 ns runs in the microcanonical ensemble. The heat flux is computed every 2 fs and the HCACF is averaged in blocks of 100 ps, of which an example is shown in Fig. S6.† All classical MD simulations were performed using a 0.5 fs timestep and the system's temperature was verified to be 300 K at the end of the *NVE* simulations.

Afterwards, the thermal conductivity was computed by integrating the HCACF over time (Fig. S6†). As the resulting thermal conductivity can be substantially influenced by slow oscillations in the HCACF, it is necessary to integrate over a sufficiently long time interval.[93] These slow oscillations in the tail of the auto-correlation function mix with numerical noise, which contaminates the HCACF and cumulates a considerable integration error for the thermal conductivity.[94,95] For some simulations, this resulted in a slight deviation from zero for the HCACF's tail, which we removed after fitting.[94] Methods that take care of this in a systematic way are to the best of our knowledge not directly applicable to complex systems like MOFs due to a non-monotonic HCACF.[96] Finally, we determined the thermal conductivity by taking the running average of the last 25 ps, similar to previous work.[29,36,96]

An error bar was estimated using bootstrapping. This is done by resampling the thermal conductivity results of the hundred independent trajectories. We find errors between 0.01 and 0.05 W m^{-1} K^{-1}. Note that this error bar only captures sampling effects and does not take into account limitations of the force field and the simulation method.

2.4 Vibrational analysis

To understand the influence of NQEs on the Helmholtz free energy profile of MIL-53(Al), the vibrational frequency spectrum of MIL-53(Al) is also investigated.[97,98] The normal modes and the corresponding frequencies of the np and lp phases are determined *via* diagonalization of the mass-weighted Hessian, obtained from *ab initio* calculations. For more details about the computational settings, we refer to previous work.[98]

These lattice vibrations are furthermore also known to have an impact on the thermal properties of a material. For the specific case of MOFs, it was shown that vibrational modes can be linked with the direction of the heat transfer within the system.[30] The effect of the lattice vibrations on the thermal conductivity can be assessed by constructing the so-called vibrational density of states (VDOS):[30]

$$\mathrm{VDOS}(\sigma) = \int \mathrm{d}t\gamma(t)\ \exp\ (-2\pi j\sigma t), \tag{2}$$

which corresponds with the Fourier transform of the velocity autocorrelation function, $\gamma(t)$, defined as

$$\gamma(t) = \frac{\left\langle \sum_i v_i(0)v_i(t) \right\rangle}{\left\langle \sum_i v_i(0)v_i(0) \right\rangle}. \tag{3}$$

The VDOS spectra of the different atom types in MIL-53(Al) can be calculated from the classical MD simulations on the $1 \times 2 \times 1$ supercells. The integration in

ART ■ D0FD00025F

the VDOS expression is then reduced to a sum, resulting in a discrete Fourier transform that is evaluated using Yaff.[76]

3 Results and discussion

3.1 Flexibility of MIL-53(Al)

As the relative stability of the narrow-pore (np) and large-pore (lp) phases of MIL-53(Al) has already been demonstrated to depend critically on the description of long-range dispersion interactions[52,99] and is altered by the presence of additional metastable phases of coexisting lp and np layers at a mesoscale level,[53,100] we now revert our attention to the influence of NQEs on the phase stability. Given the intention to examine the presence of water molecules in the MIL-53 framework, the archetypal molecules investigated within the context of NQEs, we first assess the effect of including NQEs for the empty framework. Following the thermodynamic protocol outlined in Section 2.2, Helmholtz free energy profiles of MIL-53(Al) are constructed at 100 and 300 K, using both classical MD and PIMD, for which the results are depicted in Fig. 2a. At 300 K, classical MD predicts an lp–np Helmholtz free energy difference of 38.3 kJ mol^{-1}, whereas PIMD yields a difference of 35.2 kJ mol^{-1}. At 100 K, the Helmholtz free energy differences obtained from classical MD and PIMD are respectively 47.3 kJ mol^{-1} and 43.6 kJ mol^{-1}. These moderate differences of about 3 to 4 kJ mol^{-1} in the relative lp–np stability can be explained by considering the vibrational frequencies characterizing the np and lp phases (Fig. 3), obtained from an *ab initio* normal mode analysis of the structures.[98] From these vibrational frequencies, the classical and quantum mechanical partition functions can be calculated using a harmonic

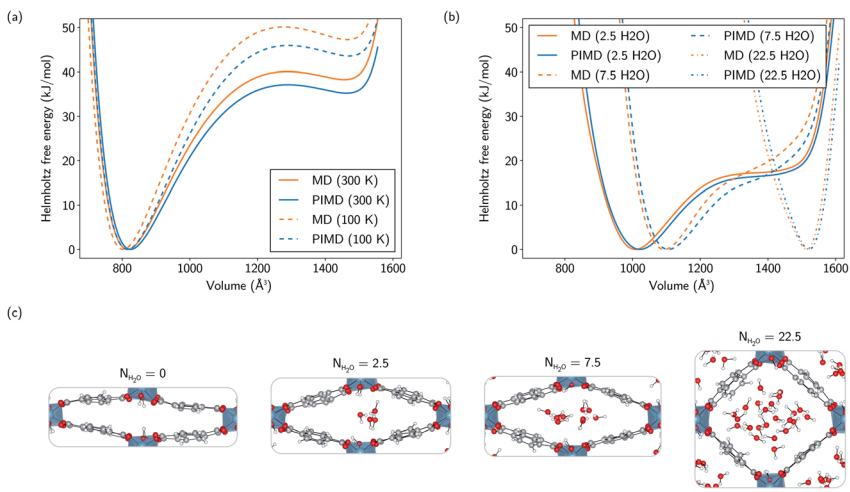

Fig. 2 (a) Helmholtz free energy profiles of MIL-53(Al) as a function of volume at 100 K and 300 K, as calculated using both MD and PIMD simulations. (b) Helmholtz free energy profiles of MIL-53(Al) as a function of volume at 300 K for water loadings of 2.5, 7.5, and 22.5 water molecules per conventional unit cell, as calculated using both MD and PIMD simulations. (c) Molecular representations of an MD snapshot at the equilibrium volume with 0, 2.5, 7.5, and 22.5 water molecules in the pores. All simulations were performed with a 1 × 2 × 1 supercell.

ART ■ D0FD00025F

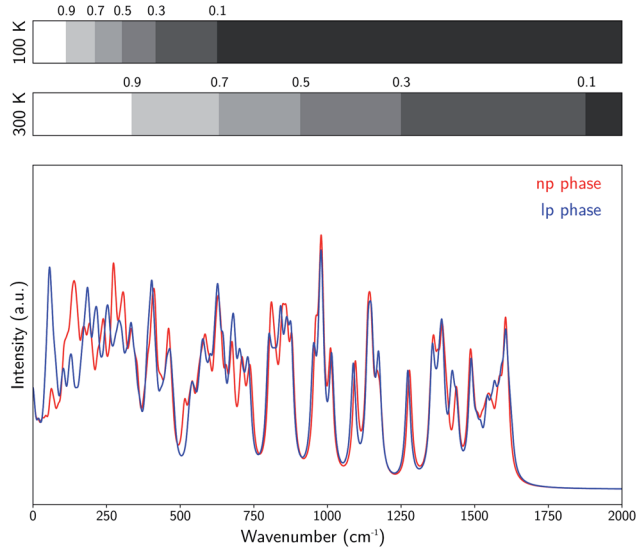

Fig. 3 Visualization of the *ab initio* vibrational frequencies of the np and lp phases of MIL-53(Al). At each vibrational frequency, a Lorentzian curve was generated with a full-width-at-half-maximum of 10 cm^{-1}. The bars on top indicate the wavenumber regions for which the ratio of the quantum mechanical and classical partition functions is larger than respectively 0.9, 0.7, 0.5, 0.3, and 0.1, both at 100 K and 300 K.

approximation. The ratio of both partition functions for a specific set of modes is then to be viewed as a measure of the degree of quantumness of these modes:

$$\frac{Z_{\text{quantum}}}{Z_{\text{classical}}} = \prod_{i=1}^{N} \frac{\exp\left(-\frac{\hbar\omega_i}{2k_B T}\right)}{1-\exp\left(-\frac{\hbar\omega_i}{k_B T}\right)} \prod_{i=1}^{N} \frac{\hbar\omega_i}{k_B T}, \quad (4)$$

where ω_i is the angular frequency of the mode, T is the temperature, and k_B is the Boltzmann constant. As shown in Fig. 3, a quantum mechanical description of the modes is particularly important within a higher frequency range. The lower the temperature, the lower the frequency at which modes start to yield a significant quantum mechanical contribution to the partition function. Since the modes associated with the lp-to-np transition are predominantly located within the low frequency region (*i.e.* below 100 cm^{-1}),[98] the difference in the relative lp–np stability due to the quantum mechanical nature of the atomic nuclei is expected to be relatively moderate, as observed in Fig. 2a. However, the fact that there is a small difference in the relative lp–np stability clearly indicates that the np and lp phases are affected differently by NQEs.

3.2 Water in the pores of MIL-53(Al)

Although a substantial number of MOFs possess poor stability with respect to hydration, the MIL-53 family of soft porous crystals is known to have stable hydrated phases, which have been investigated both experimentally and

computationally, focusing mainly on the chromium- and gallium-based variants.[51,58–61,101–108]

Here, the influence of the presence of water on the Helmholtz free energy profile of MIL-53(Al) is investigated, closely monitoring the changes in behaviour of the adsorbed species along the profile. Three different water loadings are considered: 2.5, 7.5, and 22.5 water molecules per conventional unit cell, varying from a ratio of less than one molecule per aluminium atom to almost six molecules per aluminium atom. For the lowest loading, the metastable lp phase disappears, while the Helmholtz free energy profile retains a shape similar to the profile of the empty framework, but shifted to an equilibrium volume that is about 200 Å^3 larger, thereby stabilizing an intermediate state with a volume in between those of the np and lp phases of the empty framework. On increasing the water loading up to 7.5 molecules per unit cell, the equilibrium volume is further shifted by an additional 85 Å^3 and the Helmholtz free energy profile is no longer reminiscent of the bistable empty material. At the highest water loading, representing a 'superhydrated' state, the Helmholtz free energy profile possesses a sharp minimum which is only shifted towards higher volume by about 55 Å^3 with respect to the lp equilibrium volume.

The differences between the classically and quantum-mechanically calculated Helmholtz free energy profiles are similar to the ones observed for the empty framework, resulting in a Helmholtz free energy difference of the same order of magnitude, *i.e.* generally smaller than about 3 kJ mol^{-1}, at larger volumes.

From these simulations, one can also infer the average adsorption enthalpy by simply conducting one additional simulation on a single water molecule. The average adsorption enthalpy ΔH_{ads} of the sequential adsorption of N gas phase water molecules into the empty framework is then given by

$$\Delta H_{\mathrm{ads}}(0 \rightarrow N;\, T) = \Delta U(0 \rightarrow N;\, T) + P\Delta V(0 \rightarrow N;\, T) - N(U_{\mathrm{H_2O}} + k_{\mathrm{B}}T), \quad (5)$$

where $\Delta U(0 \rightarrow N)$ and $\Delta V(0 \rightarrow N)$ are respectively the change in internal energy and volume of the system on adsorbing N water molecules and $U_{\mathrm{H_2O}}$ is the internal energy of a single water molecule in the gas phase. A derivation of this formula can be found in the ESI of ref. 36. The values of the adsorption enthalpy for the different water loadings, calculated using both MD and PIMD, are reported in Table 1 and are of the same order of magnitude as the experimental isosteric heat of adsorption mentioned in ref. 19 and 28 for other aluminium-based frameworks such as MIL-160(Al) and MOF-303. The differences related to the inclusion of NQEs are once more limited to about 2–3 kJ mol^{-1}. As more water molecules are added to the framework, the increase in the magnitude of the adsorption energy decreases, as demonstrated by the small difference in adsorption enthalpy for 7.5

Table 1 Average adsorption enthalpy $\Delta H_{\mathrm{ads}}/N$ per H_2O molecule at 300 K and 1 bar (in kJ mol^{-1}) for different water loadings of MIL-53(Al) at the equilibrium volume

	$N_{\mathrm{H_2O}} = 2.5$	$N_{\mathrm{H_2O}} = 7.5$	$N_{\mathrm{H_2O}} = 22.5$
Classical MD	−26.9	−45.1	−48.5
PIMD	−24.2	−42.9	−46.6

ART ■ D0FD00025F

and 22.5 water molecules per unit cell. This also implies that the adsorption process of water within MIL-53(Al) cannot be described by means of a simplified mean-field model, which is of course related to the more complex nature of directional hydrogen bonding interactions that are essential in the description of water.

Finally, the molecular organization of the water molecules within the MIL-53 framework can also be considered by means of density plots of the guest

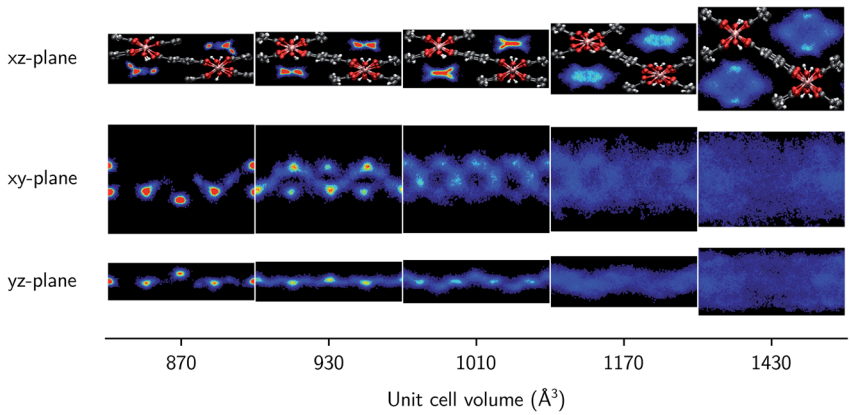

Fig. 4 Symmetrised water density in MIL-53(Al) projected onto the *xz*-plane (perpendicular to the *b*-axis), the *xy*-plane (perpendicular to the *c*-axis), and the *yz*-plane (perpendicular to the *a*-axis) for 2.5 water molecules per unit cell at different volumes. In each figure, a 1 × 2 × 1 supercell is shown, containing 5 water molecules. For the *xy*- and *yz*-planes, only the upper half of the simulation cell is shown, as the bottom half is its symmetrical equivalent.

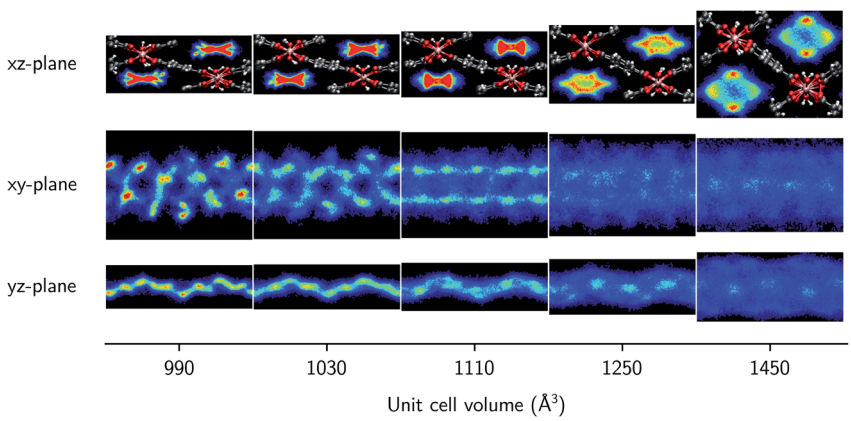

Fig. 5 Symmetrised water density in MIL-53(Al) projected onto the *xz*-plane (perpendicular to the *b*-axis), the *xy*-plane (perpendicular to the *c*-axis), and the *yz*-plane (perpendicular to the *a*-axis) for 7.5 water molecules per unit cell at different volumes. In each figure, a 1 × 2 × 1 supercell is shown, containing 15 water molecules. For the *xy*- and *yz*-planes, only the upper half of the simulation cell is shown, as the bottom half is its symmetrical equivalent.

ART ■ D0FD00025F

molecules, thereby visualizing their spatial probability distribution. These densities are shown in Fig. 4 and 5 for different volumes and for both 2.5 and 7.5 water molecules per unit cell, considering the projections onto the planes perpendicular to each of the three cell axes. The density plots for the case of 22.5 water molecules per unit cell can be found in the ESI (Fig. S3†). While no clear preferential hydrogen bonding is observed with the hydroxyl framework groups, which is most likely related to the lack of an explicit force field description of hydrogen bonding or polarization,[59] Medders *et al.*[104] also reported a disruption of these preferential hydrogen bonds for water loadings exceeding the number of hydroxyl framework groups. Hydrogen bonds are however formed with the oxygen atoms of the carboxylate groups of the linkers of the framework (see ESI Fig. S4†). Furthermore, the typical 1D water wires in the direction of the aluminium-oxide chains, which have been observed in previous studies of MIL-53-type frameworks,[58,102,104] are also present in our simulations at lower volumes (within the np region). At higher volumes, the water molecules take advantage of the additional motional freedom gained through the increase in pore size, leading to a more diffuse picture when compared to the np region. Given that the larger densities are located near the edges of the pore, the presence of the framework is clearly also felt at higher volumes.

3.3 Thermal conductivity

After having investigated the organization of water molecules within the framework of MIL-53(Al), as well as their impact on the flexibility, we now focus again on the framework itself, instead of on the host–guest and guest–guest effects. Insight into the intrinsic heat transfer characteristics of the adsorbent is also essential for a molecular-level understanding of water-adsorption applications. The influence of guest molecules on the thermal conductivity of MOFs is still a topic of debate, but lies beyond the scope of the current study.[26,32,109,110] Some studies have suggested that guest molecules improve the heat transfer (*i.e.* the

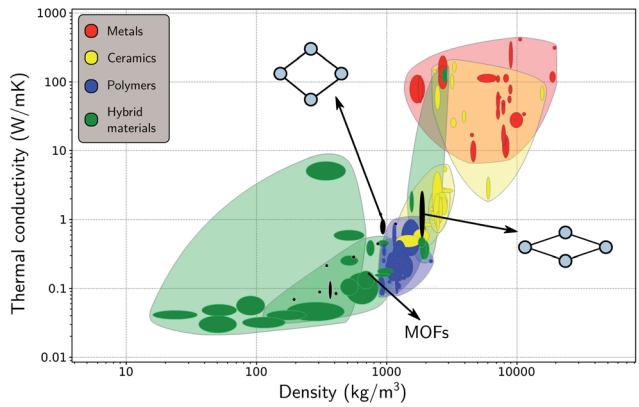

Fig. 6 Materials property chart displaying the thermal conductivity and the density of MOFs alongside other material classes, namely, metals (and alloys), ceramics (glasses and (non-)technical ceramics), polymers, and hybrid materials (composites, foams, and natural materials). The thermal conductivities of the lp and the np phases are indicated with black ovals. Figure adapted from ref. 36 with permission of the American Chemical Society.

ART ■ D0FD00025F

thermal conductivity increases with the loading), while others have reported the opposite.

In general, MOFs are poor heat conductors, especially in comparison with other materials (Fig. 6),[36] which can pose a major technological barrier for practical applications. Therefore, both experimental and theoretical in-depth investigations are required to address this problem. However, apart from an already established relationship between the difficult heat dissipation in MOFs and their inherent porosity,[29,30,33,36,109] the directional dependence of the thermal conductivity has barely been investigated.[31,33,40] Given that flexible MOFs can have a very anisotropic response to different stimuli,[38,111] the heat transfer is also expected to show a directional dependence. For a set of idealized MOFs, Wilmer and co-workers studied the anisotropy of the thermal conductivity,[33] considering frameworks with a simple cubic structure, a triangular-channel structure, and a hexagonal-channel structure, and discussed how the pore shape and size affect the thermal conductivity in different directions. Their study indicated that MOFs with smaller pores are likely to have a better thermal performance, *i.e.* a higher thermal conductivity, which was also demonstrated for the IRMOF series.[36,109]

3.3.1 Volume dependence of the thermal conductivity. As MIL-53(Al) has lozenge-shaped channels (Fig. 1), which differ in size and shape for the np and lp phases, we computed the thermal conductivity along the *a*-, *b*- and *c*-directions as a function of the volume of the conventional unit cell. The results are shown in Fig. 7. In the region where MIL-53(Al) is mechanically unstable (Fig. S2†),[46] a separation of lp and np volume states was observed in agreement with recent findings of Rogge *et al.*[53] These long-range correlation effects impeded an accurate estimation of the thermal conductivity in between the (meta)stable lp and the np phases, as the obtained volume distribution depends on the size of the simulation cell. A snapshot of a structure containing different volume states is displayed in Fig. S7,† together with its volume distribution which shows two distinct maxima. Interestingly, no transitions were observed between the different volume states during the microcanonical simulations used to compute the heat current autocorrelation function. After the equilibration run at 300 K in the canonical ensemble, in which a separation between the lp and np volume states occurs spontaneously, the individual cells remain frozen in the acquired volume states. While local energy fluctuations are still possible in the microcanonical ensemble, transitions between different volume states are expected to be extremely unlikely in a $7 \times 8 \times 7$ supercell, as the energy of the total system is kept constant. These spatially disordered phenomena in flexible materials will have to be taken into account in future heat transfer studies and pose an additional difficulty for the already challenging modelling of these flexible systems.

In the lp region (Fig. 7), the thermal conductivity in the *a*-direction is clearly higher than the thermal conductivity in the *c*-direction. In these directions, the heat is transferred along the bonds of the organic linkers, which are more aligned with the *a*-direction than with the *c*-direction (Fig. 1). As the angle between the organic linkers and the *a*-direction increases from approximately 30 to 40 degrees in the lp region, the alignment with the *a*-direction decreases at larger volumes and so does the thermal conductivity. Consequently, the opposite trend is found for the *c*-direction. For the one-dimensional Al(OH) chains (*i.e.* the *b*-direction), the heat conduction is also observed to be worse than for the *a*-direction.

ART ■ D0FD00025F

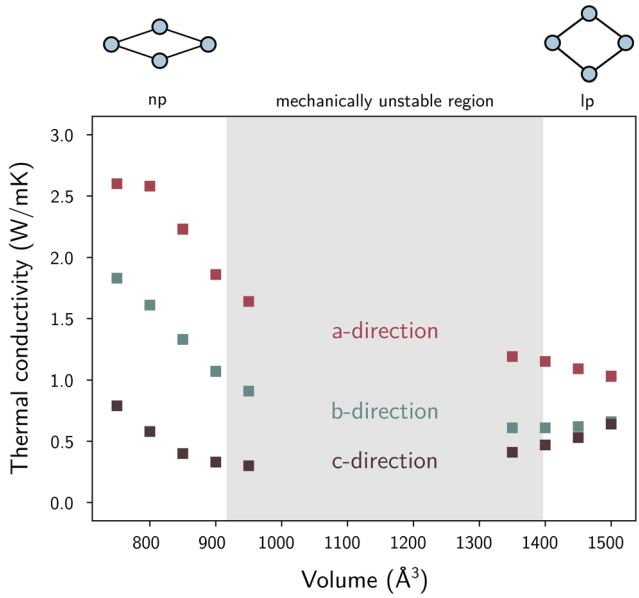

Fig. 7 The thermal conductivity of MIL-53(Al) as a function of the volume at room temperature. The volumes in between the lp and the np phases are mechanically unstable.

The trends in the np region are less intuitive. The thermal conductivity along the *a*-direction generally increases when the volume decreases (Fig. 7). At the lowest volumes, the organic linkers are nearly parallel with this direction due to the knee-cap configuration of MIL-53(Al), and the dominant thermal resistance along this direction will reside in the organic–inorganic connections in between connecting linkers (Fig. 8). A very strong increase in the thermal conductivity

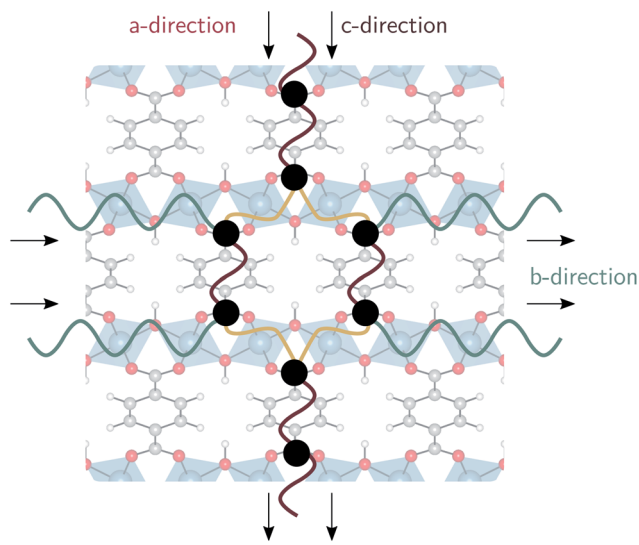

Fig. 8 Schematic illustration of the energy carriers along the *a*-, *b*- and *c*-directions.

ART ■ D0FD00025F

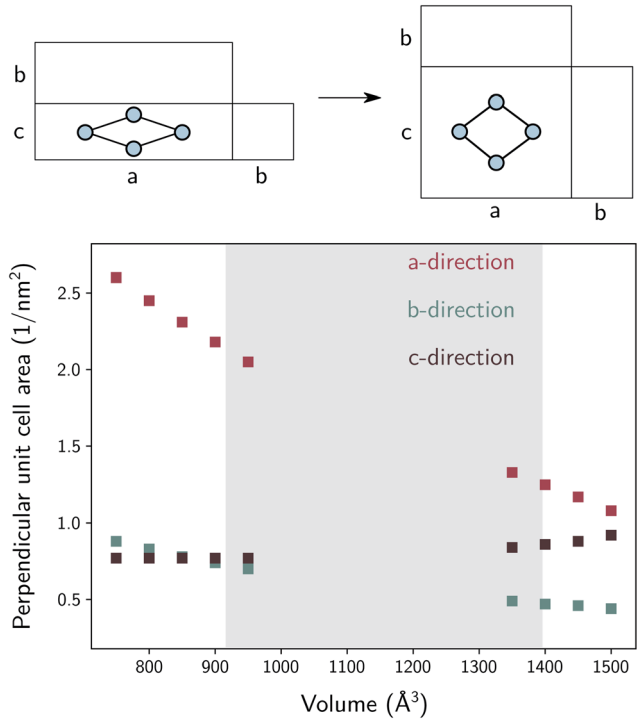

Fig. 9 Inverse of the cross-sectional area in the unit cell perpendicular to the indicated lattice direction as a function of the volume. A schematic representation of the cross-sectional area in the three directions is shown on top.

along the *c*-direction is absent, which shows that although the organic linkers are stacked very closely, not a lot of heat is transported along the pore vacuum.

The thermal conductivity in the *b*-direction strongly increases at the lowest volumes. However, note that the thermal conductivity in a certain direction is defined as the ability of a material with unit length thickness along this direction to transfer heat per unit of cross-sectional surface area in the perpendicular direction (Fig. S5†). In MIL-53(Al), the unit cell surface area perpendicular to the *b*-direction increases substantially during the phase transition towards increasing volume, while the lattice parameter *b* does not, as schematically illustrated in Fig. 9. Hence, the thermal conductivity along this direction follows to some extent the trend in the inverse of the area as a function of the volume (Fig. 9). In other words, per unit of surface area, fewer conducting Al(OH) chains are present, causing the thermal conductivity to decrease. The same reasoning holds for the number of stacked organic linkers in the surface area perpendicular to the *a*-direction.

Furthermore, the sharp increase in the thermal conductivity along the *b*-direction at the lowest volumes is believed to be connected to another phenomenon. As the interchain thermal resistance is heavily reduced by both the close approach of the Al(OH) chains (in the *c*-direction) and the almost parallel stacking of the organic linkers, the heat dissipated along the direction of the Al(OH) chain can spread more easily over multiple chains. This might also explain why the

ART ■ D0FD00025F

volume dependence of the thermal conductivity in the *a*- and *b*-directions roughly follows the same trend.

3.3.2 Specific *vs.* absolute thermal conductivity. When comparing the values of the thermal conductivity near the equilibrium np and lp volumes of MIL-53(Al) (Table 2) to those of other MOFs reported in the literature (Table 3), the lp phase is found to yield a thermal conductivity of the same order of magnitude as other MOFs with a similar mass density (*e.g.* MOF-505 and UiO-66).[36] For the np phase, on the other hand, the thermal conductivity has a much higher value than for other MOFs, especially along the *a*- and *b*-directions. However, given that its mass density is almost doubled with respect to the lp phase and the thermal conductivity strongly correlates with the mass density (Fig. 6), this is to be expected.

Although these values for the specific thermal conductivity seem to imply that heat is conducted much easier in the np phase than in the lp phase, a fair comparison should also take the difference in cell shape of the two phases into account. For practical MOF applications, the required amount of material will play an important role and is expected to remain constant throughout the operation of the device. Therefore, it is instructive to determine the absolute thermal conductivity κ^{abs}, which is an extensive property (with units W K^{-1}):

Table 2 Thermal conductivity of MIL-53(Al) in both phases ($V_{np} = 800$ Å^3, $V_{lp} = 1500$ Å^3) at room temperature. The absolute thermal conductivity is given per conventional unit cell. More information regarding the error bars is given in the Methodology section

	lp	np
κ_{aa} (W m^{-1} K^{-1})	1.03 ± 0.01	2.58 ± 0.04
κ_{bb} (W m^{-1} K^{-1})	0.66 ± 0.01	1.61 ± 0.03
κ_{cc} (W m^{-1} K^{-1})	0.64 ± 0.01	0.58 ± 0.01
ρ (kg m^{-3})	922	1727
κ_{aa}^{abs} (nW K^{-1})	0.6	0.5
κ_{bb}^{abs} (nW K^{-1})	2.2	2.9
κ_{cc}^{abs} (nW K^{-1})	0.5	1.2

Table 3 Overview of the thermal conductivities of MOFs published in the literature

	κ (W m^{-1} K^{-1})	
MOF	Experiment	Simulations
Al-soc-MOF-1	—	0.22 (ref. 36)
HKUST-1	0.27–0.39 (ref. 25 and 27)	0.45–0.58 (ref. 25 and 36)
IRMOF-10	—	0.02–0.09 (ref. 36 and 109)
IRMOF-16	—	0.07 (ref. 36)
MIL-160	0.06 (ref. 28)	—
MOF-5	0.34 (ref. 24)	0.12–0.31 (ref. 25, 29, 36 and 109)
MOF-177	—	0.08–0.09 (ref. 36)
MOF-505	—	1.16–1.26 (ref. 36)
UiO-66	0.11 (ref. 27)	0.87 (ref. 36)
UiO-67	0.19 (ref. 27)	—
UMCM-1	—	0.07–0.13 (ref. 36)
ZIF-8	0.33 (ref. 26)	0.17 (ref. 30 and 110)

ART ■ D0FD00025F

$$\kappa_{ii}^{\mathrm{abs}} = \frac{A}{d}\kappa_{ii}, \tag{6}$$

where A is the cross-sectional area perpendicular to the path of the heat flow (i-direction), d is the thickness along the path of the heat flow, and κ is the thermal conductivity along the path of the heat flow (Fig. S5†). This quantity can be used to compare the heat transfer characteristics of the lp and the np phases for the same amount of matter, correcting for their different physical dimensions. The tabulated values for κ^{abs} (Table 2) indicate that the heat transfer in the a- and b-directions for a given temperature difference is not as different for the lp and np phases as the specific thermal conductivities suggest. The thermal conductivity in the b-direction does, however, slightly increase, which might be related to a decrease in the interchain thermal resistance, as suggested in the previous section. In Fig. S8,† the absolute thermal conductivity is shown as a function of volume for a single unit cell.

A possible strategy to exploit the anisotropy of the thermal conductivity of MOFs was suggested by Wilmer *et al.*[33] Given that structures with large channels are known to be beneficial for rapid gas adsorption, but also give rise to ultra-low thermal conductivities, MOFs could be designed to rapidly dissipate heat along the channel direction to remedy the problem of heat conduction. For MIL-53(Al), the heat transfer per unit cell was shown to behave anisotropically (Table 2), with heat dissipating more easily along the one-dimensional aluminium-oxide chains following the b-direction. This result is in line with the good thermal conductivity of aluminium oxide (Al_2O_3, $\kappa \approx 30$ W m^{-1} K^{-1}).

3.3.3 Vibrational density of states. The difference in heat transfer along the organic linkers (a- and c-directions) and the inorganic chain (b-direction) is also reflected in the overlap of the vibrational density of states (VDOS). A low overlap between the VDOS of neighbouring interfaces, such as a solid–liquid or solid–solid interface, implies a high thermal resistance.[112–114] For ZIF-8, Zhang and Jiang demonstrated that there is little overlap between the atomic VDOS of the main

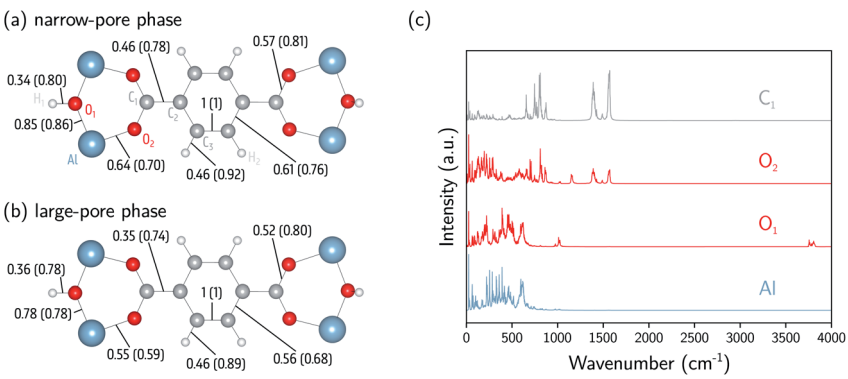

Fig. 10 Analysis of the atomic vibrational density of states (VDOS). (a) The similarity index calculated at 0–4000 cm^{-1} (0–700 cm^{-1}) for the np phase (800 Å^3). (b) The similarity index calculated at 0–4000 cm^{-1} (0–700 cm^{-1}) for the lp phase (1500 Å^3). (c) The atomic VDOS for Al, O_1, O_2 and C_1. The atomic VDOS for other atoms is reported in the ESI (Fig. S9 and S10†). The intensities have been rescaled by dividing the complete spectrum by the square root of the integral of the square of the spectrum.

ART ■ D0FD00025F

energy carriers (Zn and N) in the framework.[30,110] For MIL-53(Al), we quantified the overlap in VDOS along all atomic bonds using a similarity index:[97]

$$\text{Similarity index} = \frac{\int d\sigma f(\sigma) g(\sigma)}{\sqrt{\int d\sigma f^2(\sigma) \int d\sigma g^2(\sigma)}}. \quad (7)$$

It is a measure of the correlation between two spectra $f(\sigma)$ and $g(\sigma)$ in a certain frequency range. We determined this similarity index for all chemically bonded atom pairs by computing the overlap between the VDOS of both atoms in the frequency range 0–4000 cm^{-1} and in the low-frequency range 0–700 cm^{-1}. Using this approach, a large overlap in the VDOS along the aluminium-oxide chain is found, as displayed in Fig. 10. This similarity index is especially large when compared to the similarity indices of the Al–O_2, O_2–C_1, and C_1–C_2 bonds along which the heat needs to transfer for the *a*- and *c*-directions (Fig. 8), so that the similarity index corroborates the absolute thermal conductivity results. Finally, the results in Fig. 10 also show that the overlap is systematically larger in the np phase, which again agrees well with Table 2.

4 Conclusions

Within the past few years, MOFs have gradually gained a more established reputation as promising solid adsorbents in the field of water-adsorption applications. To obtain a more fundamental understanding of their potential performance and shed light on current barriers, such as the slow heat transfer of MOFs, molecular simulations can be performed to theoretically investigate the framework properties and the interactions with water. In this work, the flexible MIL-53(Al) framework was analysed, focusing on the influence of water on the phase stability and the structural properties, as well as on the thermal conductivity of the framework.

To assess the flexibility of the framework, an adequate modelling technique is required, such as the thermodynamic protocol in ref. 46, which allows the construction of Helmholtz free energy profiles to identify the (meta)stable states of the system as a function of the loading. Several studies have already highlighted the importance of the weak dispersion forces[36,99] and structural disorder[53,100] in the description of the flexibility of MIL-53(Al), but the quantum nature of the atoms has not yet been taken into account. However, as evidenced by this study of MIL-53(Al) with and without water in the pores, nuclear quantum effects do not seem to play a major role in the relative phase stability of the material. Both classical and path integral molecular dynamics simulations indicate that the volume of the np phase continuously increases with the water loading until the lp phase becomes the only stable state at a very high loading. For all the considered water loadings, the adsorbed molecules are observed to engage in ordered hydrogen bonded structures resembling 1D water wires along the aluminium-oxide chains for volume states located around the equilibrium volume. If the pore volume, on the contrary, substantially deviates from the equilibrium volume, the water molecules spread more freely inside the pores, although they remain predominantly located near the edges of the pores due to their interaction with the framework.

Furthermore, the thermal conductivity of the framework was also calculated in the three crystal directions as a function of the volume, which allows us to compare the thermal performance of the np and lp phases. To capture the influence of long-range spatial disorder present in experimental samples, new simulation strategies will have to be developed. In this work, the thermal conductivity of MIL-53(Al) was found to be strongly linked to the geometry of the unit cell, and in absolute numbers the heat transfer in the np phase was shown to be more efficient. The aluminium-oxide chain was thereby identified as the best conducting fragment of the material, as confirmed by the overlap in the vibrational density of states of the aluminium and oxygen atoms.

These findings clearly demonstrate that molecular simulations can offer useful insights into the fundamental properties relevant for water-adsorption applications. Promising water-adsorption materials pointed out by experimental studies will be further explored in future studies.

Conflicts of interest

There are no conflicts to declare.

Acknowledgements

This work is supported by the Fund for Scientific Research Flanders (FWO). V. V. S. acknowledges funding from the European Union's Horizon 2020 Research and Innovation Program (consolidator ERC grant agreement No. 647755 - DYNPOR (2015–2020)). The work is furthermore supported by the Research Board of Ghent University (BOF). The computational resources and services used in this work were provided by VSC (Flemish Supercomputer Center), funded by Ghent University, FWO, and the Flemish Government department EWI.

Notes and references

1 A. Schoedel, Z. Ji and O. M. Yaghi, *Nat. Energy*, 2016, **1**, 16034.
2 Y. He, F. Chen, B. Li, G. Qian, W. Zhou and B. Chen, *Coord. Chem. Rev.*, 2018, **373**, 167–198.
3 H. Li, K. Wang, Y. Sun, C. T. Lollar, J. Li and H.-C. Zhou, *Mater. Today*, 2018, **21**, 108–121.
4 M. Ding, R. W. Flaig, H.-L. Jiang and O. M. Yaghi, *Chem. Soc. Rev.*, 2019, **48**, 2783–2828.
5 N. C. Burtch, H. Jasuja and K. S. Walton, *Chem. Rev.*, 2014, **114**, 10575–10612.
6 J. Carnivet, A. Fateeva, Y. Guo, B. Coasne and D. Farrusseng, *Chem. Soc. Rev.*, 2014, **43**, 5594–5617.
7 H. Furukawa, F. Gándara, Y.-B. Zhang, J. Jiang, W. L. Queen, M. R. Hudson and O. M. Yaghi, *J. Am. Chem. Soc.*, 2014, **136**, 4369–4381.
8 C. Wang, X. Liu, N. K. Demir, P. J. Chen and K. Li, *Chem. Soc. Rev.*, 2016, **45**, 5107–5134.
9 J. Duan, W. Jin and S. Kitagawa, *Coord. Chem. Rev.*, 2017, **332**, 48–74.
10 J. Ehrenmann, S. K. Henninger and C. Janiak, *Chem.–Eur. J.*, 2011, **2011**, 471–474.

ART ■ D0FD00025F

11 F. Jeremias, D. Fröhlich, C. Janiak and S. K. Henninger, *RSC Adv.*, 2014, **4**, 24076–24082.

12 A. Cadiau, J. S. Lee, D. B. Borges, P. Fabry, T. Devic, M. T. Wharmby, C. Martineau, D. Foucher, F. Taulelle, C.-H. Jun, Y. K. Hwang, N. Stock, M. F. De Lange, F. Kapteijn, J. Gascon, G. Maurin, J.-S. Chang and C. Serre, *Adv. Mater.*, 2015, **27**, 4775–4780.

13 M. F. de Lange, K. J. F. M. Verouden, T. J. H. Vlugt, J. Gascon and F. Kapteijn, *Chem. Rev.*, 2015, **115**, 12205–12250.

14 S. Wang, J. S. Lee, M. Wahiduzzaman, J. Park, M. Muschi, C. Martineau-Corcos, A. Tissot, K. H. Cho, J. Marrot, W. Shepard, G. Maurin, J.-S. Chang and C. Serre, *Nat. Energy*, 2018, **3**, 985–993.

15 D. Lenzen, J. Zhao, S.-J. Ernst, M. Wahiduzzaman, A. K. Inge, D. Fröhlich, H. Xu, H.-J. Bart, C. Janiak, S. Henninger, G. Maurin, X. Zou and N. Stock, *Nat. Commun.*, 2019, **10**, 3025.

16 H. Kim, S. Yang, S. R. Rao, S. Narayanan, E. A. Kapustin, H. Furukawa, A. S. Umans, O. M. Yaghi and E. N. Wang, *Science*, 2017, **356**, 430–434.

17 A. J. Rieth, S. Yang, E. N. Wang and M. Dinca, *ACS Cent. Sci.*, 2017, **3**, 668–672.

18 M. J. Kalmutzki, C. S. Diercks and O. M. Yaghi, *Adv. Mater.*, 2018, **30**, 1704304.

19 N. Hanikel, M. S. Prévot, F. Fathieh, E. A. Kapustin, H. Lyu, H. Wang, N. J. Diercks, G. T. Glover and O. M. Yaghi, *ACS Cent. Sci.*, 2019, **5**, 1699–1706.

20 J. J. Purewal, D. Liu, J. Yang, A. Sudik, D. J. Siegel, S. Maurer and U. Müller, *Int. J. Hydrogen Energy*, 2012, **37**, 2723–2727.

21 J. Purewal, D. Liu, A. Sudik, M. Veenstra, J. Yang, S. Maurer, U. Müller and D. J. Siegel, *J. Phys. Chem. C*, 2012, **116**, 20199–20212.

22 D. Liu, J. J. Purewal, J. Yang, A. Sudik, S. Maurer, U. Müller, J. Ni and D. J. Siegel, *Int. J. Hydrogen Energy*, 2012, **37**, 6109–6117.

23 Y. Ming, J. Purewal, D. Liu, A. Sudik, C. Xu, J. Yang, M. Veenstra, K. Rhodes, R. Soltis, J. Warner, M. Gaab, U. Müller and D. J. Siegel, *Microporous Mesoporous Mater.*, 2014, **185**, 235–244.

24 B. L. Huang, Z. Ni, A. Millward, A. J. H. McGaughey, C. Uher, M. Kaviany and O. M. Yaghi, *Int. J. Heat Mass Transfer*, 2007, **50**, 405–411.

25 K. J. Erickson, F. Léonard, V. Stavila, M. E. Foster, C. D. Spataru, R. E. Jones, B. M. Foley, P. E. Hopkins, M. D. Allendorf and A. A. Talin, *Adv. Mater.*, 2015, **27**, 3453–3459.

26 B. Cui, C. O. Audu, Y. Liao, S. T. Nguyen, O. K. Farha, J. T. Hupp and M. Grayson, *ACS Appl. Mater. Interfaces*, 2017, **9**, 28139–28143.

27 J. Huang, X. Xia, X. Hu, S. Li and K. Liu, *Int. J. Heat Mass Transfer*, 2019, **138**, 11–16.

28 S. Cui, A. Marandi, G. Lebourleux, M. Thimon, M. Bourdon, C. Chen, M. I. Severino, V. Steggles, F. Nouar and C. Serre, *Appl. Therm. Eng.*, 2019, **161**, 114135.

29 B. L. Huang, A. J. H. McGaughey and M. Kaviany, *Int. J. Heat Mass Transfer*, 2007, **50**, 393–404.

30 X. Zhang and J. Jiang, *J. Phys. Chem. C*, 2013, **117**, 18441–18447.

31 X. Wang, R. Guo, D. Xu, J. Chung, M. Kaviany and B. Huang, *J. Phys. Chem. C*, 2015, **119**, 26000–26008.

32 H. Babaei and C. E. Wilmer, *Phys. Rev. Lett.*, 2016, **116**, 025902.

33 H. Babaei, A. J. H. McGaughey and C. E. Wilmer, *Chem. Sci.*, 2017, **8**, 583–589.

ART ■ D0FD00025F

34 H. Babaei, A. J. H. McGaughey and C. E. Wilmer, *ACS Appl. Mater. Interfaces*, 2018, **10**, 2400–2406.
35 K. B. Sezginel, P. A. Asinger, H. Babaei and C. E. Wilmer, *Chem. Mater.*, 2018, **30**, 2281–2286.
36 J. Wieme, S. Vandenbrande, A. Lamaire, V. Kapil, L. Vanduyfhuys and V. Van Speybroeck, *ACS Appl. Mater. Interfaces*, 2019, **11**, 38697–38707.
37 T. Loiseau, C. Serre, C. Huguenard, G. Fink, F. Taulelle, M. Henry, T. Bataille and G. Férey, *Chem.–Eur. J.*, 2004, **10**, 1373–1382.
38 A. U. Ortiz, A. Boutin, A. H. Fuchs and F.-X. Coudert, *Phys. Rev. Lett.*, 2012, **109**, 195502.
39 C. Nanthamathee, S. Ling, B. Slater and M. P. Attfield, *Chem. Mater.*, 2015, **27**, 85–95.
40 Y. Ming, H. Chi, R. Blaser, C. Xu, J. Yang, M. Veenstra, M. Gaab, U. Müller, C. Uher and D. J. Siegel, *Int. J. Heat Mass Transfer*, 2015, **82**, 250–258.
41 P. D. Shima and J. Philip, *J. Phys. Chem. C*, 2011, **115**, 20097–20104.
42 G. Zhu, J. Liu, Q. Zheng, R. Zhang, D. Li, D. Banerjee and D. G. Cahill, *Nat. Commun.*, 2016, **7**, 13211.
43 J. Shin, J. Sung, M. Kang, X. Xie, B. Lee, K. M. Lee, T. J. White, C. Leal, N. R. Sottos, P. V. Braun and D. G. Cahill, *Proc. Natl. Acad. Sci. U. S. A.*, 2019, **116**, 5973–5978.
44 S. Horike, S. Shimomura and S. Kitagawa, *Nat. Chem.*, 2009, **1**, 695–704.
45 A. Schneemann, I. Schwedler, I. Senkovska, S. Kaskel and R. A. Fischer, *Chem. Soc. Rev.*, 2014, **43**, 6062–6096.
46 L. Vanduyfhuys, S. M. J. Rogge, J. Wieme, S. Vandenbrande, G. Maurin, M. Waroquier and V. Van Speybroeck, *Nat. Commun.*, 2018, **9**, 204.
47 J. H. Lee, S. Jeoung, Y. G. Chung and H. R. Moon, *Coord. Chem. Rev.*, 2019, **389**, 161–188.
48 J. A. Mason, J. Oktawiec, M. K. Taylor, M. R. Hudson, J. Rodriguez, J. E. Bachman, M. I. Gonzalez, A. Cervellino, A. Guagliardi, C. M. Brown, P. L. Llewellyn, N. Masciocchi and J. R. Long, *Nature*, 2015, **527**, 357–361.
49 S. Hiraide, H. Tanaka, N. Ishikawa and M. T. Miyahara, *ACS Appl. Mater. Interfaces*, 2017, **9**, 41066–41077.
50 J. S. Grosch and F. Paesani, *J. Am. Chem. Soc.*, 2012, **134**, 4207–4215.
51 F.-X. Coudert, A. U. Ortiz, V. Haigis, D. Bousquet, A. H. Fuchs, A. Ballandras, G. Weber, I. Bezverkhyy, N. Geoffroy, J.-P. Bellat, G. Ortiz, G. Chaplais, J. Patarin and A. Boutin, *J. Phys. Chem. C*, 2014, **118**, 5397–5405.
52 J. Wieme, K. Lejaeghere, G. Kresse and V. Van Speybroeck, *Nat. Commun.*, 2018, **9**, 4899.
53 S. M. J. Rogge, M. Waroquier and V. Van Speybroeck, *Nat. Commun.*, 2019, **10**, 4842.
54 T. M. Markland and M. Ceriotti, *Nat. Rev. Chem.*, 2018, **2**, 0109.
55 M. Ceriotti, W. Fang, P. G. Kusalik, R. H. McKenzie, A. Michealides, M. A. Morales and T. E. Markland, *Chem. Rev.*, 2016, **116**, 7529.
56 I. J. Kang, N. A. Khan, E. Haque and S. H. Jhung, *Chem.–Eur. J.*, 2011, **17**, 6437–6442.
57 I. Bezverkhyy, G. Ortiz, G. Chaplais, C. Marichal, G. Weber and J.-P. Bellat, *Microporous Mesoporous Mater.*, 2014, **183**, 156–161.
58 F. Paesani, *Mol. Simul.*, 2012, **38**, 631–641.

ART ■ D0FD00025F

59 J. Cirera, J. C. Sung, P. B. Howland and F. Paesani, *J. Chem. Phys.*, 2012, **137**, 054704.
60 F. Paesani, *J. Phys. Chem. C*, 2013, **117**, 19508–19516.
61 J. M. Salazar, G. Weber, J. M. Simon, I. Bezverkhyy and J. P. Bellat, *J. Chem. Phys.*, 2015, **142**, 124702.
62 D. D. Borges, R. Semino, S. Devautour-Vinot, H. Jobic, F. Paesani and G. Maurin, *Chem. Mater.*, 2017, **29**, 1569–1576.
63 A. J. Rieth, K. M. Hunter, M. Dinca and F. Paesani, *Nat. Commun.*, 2019, **10**, 4771.
64 T. Ichii, T. Arikawa, K. Omoto, N. Hosono, H. Sato, S. Kitagawa and K. Tanaka, *Commun. Chem.*, 2020, **3**, 16.
65 N. C. Burtch, I. M. Walton, J. T. Hungerford, C. R. Morelock, Y. Jiao, J. Heinen, Y.-S. Chen, A. A. Yakovenko, W. Xu, D. Dubbeldam and K. S. Walton, *Nat. Chem.*, 2020, **12**, 186–192.
66 L. Vanduyfhuys, S. Vandenbrande, T. Verstraelen, R. Schmid, M. Waroquier and V. Van Speybroeck, *J. Comput. Chem.*, 2015, **36**, 1015–1027.
67 L. Vanduyfhuys, S. Vandenbrande, J. Wieme, M. Waroquier, T. Verstraelen and V. Van Speybroeck, *J. Comput. Chem.*, 2018, **39**, 999–1011.
68 J. P. Perdew, K. Burke and M. Ernzerhof, *Phys. Rev. Lett.*, 1996, **77**, 3865–3868.
69 S. Grimme, J. Antony, S. Ehrlich and H. Krieg, *J. Chem. Phys.*, 2010, **132**, 154104.
70 S. Grimme, S. Ehrlich and L. Goerigk, *J. Comput. Chem.*, 2011, **32**, 1456–1465.
71 T. Verstraelen, S. Vandenbrande, F. Heidar-Zadeh, L. Vanduyfhuys, V. Van Speybroeck, M. Waroquier and P. W. Ayers, *J. Chem. Theory Comput.*, 2016, **12**, 3894–3912.
72 J. H. Lii and N. L. Allinger, *J. Am. Chem. Soc.*, 1989, **111**, 8576–8582.
73 H. Sun, *J. Phys. Chem. B*, 1998, **102**, 7338–7364.
74 S. Habershon, T. E. Markland and D. E. Manolopoulos, *J. Chem. Phys.*, 2009, **131**, 024501.
75 J. L. F. Abascal and C. Vega, *J. Chem. Phys.*, 2005, **123**, 234505.
76 T. Verstraelen, L. Vanduyfhuys, S. Vandenbrande and S. M. J. Rogge, *Yaff 1.4.2*, 2017, http://molmod.github.io/yaff/index.html.
77 W. G. Hoover, *Phys. Rev. A: At., Mol., Opt. Phys.*, 1985, **31**, 1695–1697.
78 S. Nosé, *Mol. Phys.*, 1986, **57**, 187–191.
79 G. J. Martyna, M. L. Klein and M. E. Tuckerman, *J. Chem. Phys.*, 1992, **97**, 2635–2643.
80 G. J. Martyna, D. J. Tobias and M. L. Klein, *J. Chem. Phys.*, 1994, **101**, 4177–4189.
81 G. J. Martyna, M. E. Tuckerman, D. J. Tobias and M. L. Klein, *Mol. Phys.*, 1996, **87**, 1117–1157.
82 A. Lamaire, J. Wieme, S. M. J. Rogge, M. Waroquier and V. Van Speybroeck, *J. Chem. Phys.*, 2019, **150**, 094503.
83 V. Kapil, J. Wieme, S. Vandenbrande, A. Lamaire, V. Van Speybroeck and M. Ceriotti, *J. Chem. Theory Comput.*, 2019, **15**, 3237–3249.
84 M. Ceriotti, J. More and D. E. Manolopoulos, *Comput. Phys. Commun.*, 2014, **185**, 1019–1026.
85 V. Kapil, M. Rossi, O. Marsalek, R. Petraglia, Y. Litman, T. Spura, B. Cheng, A. Cuzzocrea, R. H. Meißner, D. M. Wilkins, P. Juda, S. P. Bienvenue, W. Fang, J. Kessler, I. Poltavsky, S. Vandenbrande, J. Wieme, C. Corminboeuf, T. D. Kühne, D. E. Manolopoulos, T. E. Markland,

J. O. Richardson, A. Tkatchenko, G. A. Tribello, V. Van Speybroeck and M. Ceriotti, *Comput. Phys. Commun.*, 2019, **236**, 214–223.
86 S. Plimpton, *J. Comput. Phys.*, 1995, **117**, 1–19.
87 M. Ceriotti, M. Parrinello, T. E. Markland and D. E. Manolopoulos, *J. Chem. Phys.*, 2010, **133**, 124104.
88 G. Bussi and M. Parrinello, *Phys. Rev. E: Stat., Nonlinear, Soft Matter Phys.*, 2007, **75**, 56707.
89 P. Raiteri, J. D. Gale and G. Bussi, *J. Phys.: Condens. Matter*, 2011, **23**, 334213.
90 B. Leimkuhler and C. Matthews, *J. Chem. Phys.*, 2013, **138**.
91 M. S. Green, *J. Chem. Phys.*, 1954, **22**, 398–413.
92 R. Kubo, *J. Phys. Soc. Jpn.*, 1957, **12**, 570–586.
93 P. K. Schelling, S. R. Phillpot and P. Keblinski, *Phys. Rev. B: Condens. Matter Mater. Phys.*, 2002, **65**, 144306.
94 J. Chen, G. Zhang and B. Li, *Phys. Lett. A*, 2010, **374**, 2392–2396.
95 L. de Sousa Oliveira and A. P. Greaney, *Phys. Rev. E*, 2017, **95**, 023308.
96 A. J. H. McGaughey and M. Kaviany, *Int. J. Heat Mass Transfer*, 2004, **47**, 1799–1816.
97 A. E. J. Hoffman, L. Vanduyfhuys, I. Nevjestic, J. Wieme, S. M. J. Rogge, H. Depauw, P. Van Der Voort, H. Vrielinck and V. Van Speybroeck, *J. Phys. Chem. C*, 2018, **122**, 2734–2746.
98 A. E. J. Hoffman, J. Wieme, S. M. J. Rogge, L. Vanduyfhuys and V. Van Speybroeck, *Z. Kristallogr. - Cryst. Mater.*, 2019, **234**, 529–545.
99 A. M. Walker, B. Civalleri, B. Slater, C. Mellot-Draznieks, F. Corá, C. M. Zicovich-Wilson, G. Román-Pérez, J. M. Soler and J. D. Gale, *Angew. Chem., Int. Ed.*, 2010, **49**, 7501–7503.
100 J. Keupp and R. Schmid, *Adv. Theory Simul.*, 2019, **2**, 1900117.
101 F. Salles, S. Bourrelly, H. Jobic, V. Devic, Guillerm, P. LLewellyn, C. Serre, G. Férey and G. Maurin, *J. Phys. Chem. C*, 2011, **115**, 10764–10776.
102 N. Guillou, F. Millange and R. I. Walton, *Chem. Commun.*, 2011, **47**, 713–715.
103 V. Haigis, F.-X. Coudert, R. Vuilleurmier and A. Boutin, *Phys. Chem. Chem. Phys.*, 2013, **15**, 19049–19056.
104 G. R. Medders and F. Paesani, *J. Phys. Chem. Lett.*, 2014, **5**, 2897–2902.
105 V. Haigis, F.-X. Coudert, R. Vuilleumier, A. Boutin and A. H. Fuchs, *J. Phys. Chem. Lett.*, 2015, **6**, 4365–4370.
106 G. Weber, I. Bezverkhyy, J.-P. Bellat, A. Ballandras, G. Ortiz, G. Chaplais, J. Patarin, F.-X. Coudert, A. H. Fuchs and A. Boutin, *Microporous Mesoporous Mater.*, 2016, **222**, 145–152.
107 L. R. Parent, H. C. Pham, J. P. Patterson, M. S. J. Denny, S. M. Cohen, N. C. Gianneschi and F. Paesani, *J. Am. Chem. Soc.*, 2017, **139**, 13973–13976.
108 E. Cockayne, *Powder Diffr.*, 2019, **34**, 227–232.
109 L. Han, M. Budge and A. P. Greaney, *Comput. Mater. Sci.*, 2014, **94**, 292–297.
110 W. Wei, J. Huang, W. Li, H. Peng and S. Li, *J. Phys. Chem. C*, 2019, **123**, 27369–27374.
111 S. Henke, A. Schneemann and R. A. Fischer, *Adv. Funct. Mater.*, 2013, **23**, 5990–5996.
112 E. T. Swartz and R. O. Pohl, *Rev. Mod. Phys.*, 1989, **61**, 605.
113 M. Hu, Y. Jing and X. Zhang, *Phys. Rev. B: Condens. Matter Mater. Phys.*, 2015, **91**, 155408.
114 A. Giri and P. E. Hopkins, *Adv. Funct. Mater.*, 2019, 1903857.

ART ■ D0FD00025F

Faraday Discussions

Cite this: DOI: 10.1039/d0fd00017e

PAPER

Influence of flexible side-chains on the breathing phase transition of pillared layer MOFs: a force field investigation†

Julian Keupp, Johannes P. Dürholt and Rochus Schmid *

Received 24th January 2020, Accepted 11th May 2020

DOI: 10.1039/d0fd00017e

The prototypical pillared layer MOFs, formed by a square lattice of paddle-wheel units and connected by dinitrogen pillars, can undergo a breathing phase transition by a "wine-rack" type motion of the square lattice. We studied this behavior, which is not yet fully understood, using an accurate first principles parameterized force field (MOF-FF) for larger nanocrystallites on the example of $Zn_2(bdc)_2(dabco)$ [bdc: benzenedicarboxylate, dabco: (1,4-diazabicyclo[2.2.2]octane)], and found clear indications for an interface between a closed and an open pore phase traveling through the system during the phase transformation [J. Keupp and R. Schmid, *Adv. Theory Simul.*, 2019, **2**, 11]. In conventional simulations in small supercells this mechanism is prevented by periodic boundary conditions (PBCs), enforcing a synchronous transformation of the entire crystal. Here, we extend this investigation to pillared layer MOFs with flexible side-chains, attached to the linker. Such functionalized (fu-)MOFs are experimentally known to have different properties with the side-chains acting as fixed guest molecules. First, in order to extend the parameterization for such flexible groups, a new parameterization strategy for MOF-FF had to be developed, using a multi-structure force based fit method. The resulting parameterization for a library of fu-MOFs is then validated with respect to a set of reference systems and shows very good accuracy. In the second step, a series of fu-MOFs with increasing side-chain length is studied with respect to the influence of the side-chains on the breathing behavior. For small supercells in PBCs a systematic trend of the closed pore volume with the chain length is observed. However, for a nanocrystallite model a distinct interface between a closed and an open pore phase is visible only for the short chain length, whereas for longer chains the interface broadens and a nearly concerted transformation is observed. Only by molecular dynamics simulations using accurate force fields can such complex phenomena can be studied on a molecular level.

Computational Materials Chemistry Group, Faculty of Chemistry and Biochemistry, Ruhr-Universität Bochum, Universitätsstr. 150, 44801 Bochum, Germany. E-mail: rochus.schmid@rub.de

† Electronic supplementary information (ESI) available. See DOI: 10.1039/d0fd00017e

1 Introduction

One of the most investigated features of metal–organic frameworks (MOFs) is the so called breathing transformation, where a partly large volume change is triggered by various stimuli like pressure, temperature or guest adsorption.[1] The novel class of porous materials has also been called "soft porous crystals"[2] since they combine an ordered crystalline structure with void space and flexibility to allow for different types of structural transitions. The "wine-rack" type breathing of pillared layer (PL) MOFs[3,4] or the MIL-53 (ref. 5 and 6) family of systems is archetypal for such a motion. Another more recent example is the buckling transformation observed for DUT-49 and related systems, leading to the so called negative gas adsorption in certain cases.[7,8] In order to shed light on the atomistic mechanism and to predict properties like gate opening pressure, the study of such structural transformations has always been accompanied by molecular simulations.[9,10] However, up to now, a general predictive theoretical model is still not available and a large number of details are not well understood: for example the experimentally observed dependence of breathing transformations on crystallite size and morphology.[11–13] Due to the delicate balance of energetic and entropic effects in such transformations a configurational sampling by molecular dynamics or Monte Carlo type simulations is inevitable, which limits the applicability of electronic structure methods like periodic density functional theory.[14–16] Out of this need we have developed a consistent and systematic parameterization strategy for molecular mechanics force fields using first principles computed reference data. The MOF-FF force field has been developed for this purpose and was successfully employed in various scenarios.[17–26]

We recently started to exploit the numerical efficiency of MOF-FF to investigate the "wine-rack" breathing transformation of the prototypical PL-MOF Zn_2(bdc)$_2$(dabco) (bdc = 1,4-benzenedicarboxylic acid; dabco = 1,4-diazabicyclo[2,2,2]octane) for large systems beyond periodic boundary conditions (PBCs).[27] For nanocrystallites (NCs) of different size we observed a first order phase transition with an interface between an open pore (op) and a closed pore (cp) phase moving through the system.[27] Note that similar behavior was found by Rogge *et al.* also using PBCs but for large supercells, where a phase coexistence with two phase boundaries is observed.[28] Noteworthy in our NC simulations, is that distinct size effects were observed due to the different surface to volume ratios. Up to now we have only considered temperature and pressure (*via* a distance constraint forcing the closing of the pore volume) as stimuli to trigger phase transformation, since guest adsorption induced transformation for the NCs is technically difficult to realize. However, both from experimental investigations and theoretical simulations it is known that linkers with flexible side-chains allow tuning of the MOF properties and behave to some extent like tethered guest molecules. In particular, such functionalized systems introduced by Fischer *et al.*,[4] referred to as fu-MOFs, adopt in contrast to the parent DMOF-1 (Zn_2(bdc)$_2$(dabco)), a narrow pore (np) form after activation which thermally opens.[29] This was successfully predicted also in theoretical simulations by us.[20] Due to the fact that these flexible side-chains are covalently attached to the linker no grand canonical simulations are needed, but the peculiar balance between entropy and dispersive interactions of

ART ■ D0FD00017E

these side-chains follows the same tendencies as adsorbed guest molecules. To this end, in this work we have extended our simulations of NCs to these fu-MOFs.

From a conceptional point of view, such side-chains add another degree of flexibility to MOFs, adding to the overall framework softness. Since only a fraction of the available pore space is occupied by these side-chains (depending on length and count) a large conformational phase space is still available for the aliphatic side-chains. By changing the nature of the fu-MOF linker, the adsorption properties can also be tuned. For example, an MOF with a selectivity for acetylene over ethylene has been synthesized by the Fischer group using a triple bond at the end of the fu-MOF side-chain.[30] An accurate force field is needed also for fu-MOFs in order to make theoretical simulations tractable. The free rotating single bond side-chains, however, pose an additional technical problem for the parameterization strategy of MOF-FF. Up to now, MOF-FF parameters have been derived for the single low energy conformation of an unstrained non-periodic model system by fitting parameters to an objective function based on structure and curvature (Hessian) projected into redundant internal coordinates (RICs).[31] For the rather rigid building blocks present in MOFs, this also results in a sufficiently accurate representation of the potential energy surface (PES) for deformed structures as present, *e.g.*, in the cp form of DMOF-1. More recently, this approach was extended to 3D periodic reference systems to fit MOF-FF and also for zeolitic imidazolate frameworks (ZIFs),[26] where chemically reasonable non-periodic clusters are not easy to construct. However, the method tends to predict wrong torsion barriers for rotatable single bonds, since the barriers are only estimated by a Fourier expansion on the basis of the curvature at a single minimum. In order to tackle the targeted fu-MOFs we first had to extend the parameterization strategy of MOF-FF for flexible rotating bonds. A fit using multiple structures needs to be employed here and we derived a force matching methodology,[32] again using RICs in order to be able to select those degrees of freedom with high relevance for the flexibility of the side-chains.

In the following section the RIC based force matching strategy for MOF-FF is explained together with the crucial computational workflow to produce reference data. In Section 3 we then report our results for small periodic fu-MOF simulations in comparison with fu-MOF NCs. We also compare them to our previous results for the unfunctionalized parent DMOF-1. Note that the computational details are given in the ESI.†

2 MOF-FF parameterization for flexible linkers

2.1 Parameterization strategy

The original MOF-FF fitting strategy relied on the structure and curvature (Hessian) of the global minimum of a non-periodic model system computed by electronic structure methods like density functional theory (DFT) as reference data, which will be referred to as single structure Hessian (SSH) fit from herein. By a global minimization of the mean square deviations of structure and curvature for selected RICs between the FF model and reference, an optimal parameter set is determined. This approach, which was shown to be successful for the typical rigid building blocks used in most MOFs,[17,23,31] is, however, likely to fail for the flexible parts of the linkers, where multiple thermally accessible conformers are connected by shallow barriers. In particular, the freely rotating single bonds between

ART ■ D0FD00017E

sp^3-hybridized atoms in our targeted fu-MOF linker library pose a significant problem, since the reference data at the global minimum (elongated chain) does not provide sufficient information concerning other conformers and the transition states between them. In order to quantify this problem, we have first parameterized MOF-FF using the conventional SSH fit in order to test the accuracy, in particular with respect to the higher energy conformers and barriers. As an alternative, we implemented a multi structure force (MSF) fit strategy, using multiple configurations generated by short finite temperature *ab initio* molecular dynamics (MD) simulations.

2.2 Reference systems

From a conceptional point, the MOF-FF approach aims to trade transferability for accuracy by generating parameter sets for each and every reference system, resembling closely the final MOF. However, in order to keep the overall effort tractable we found it useful to start with smaller fragments like for example a simple benzene molecule, and to then keep these parameters fixed in *e.g.* benzoate model systems, used to represent inorganic building blocks or secondary building units (SBUs) (see Fig. 1).[31] In this context we recently developed a hierarchical automated parameter assignment (HAPA) scheme and infrastructure,[33] where the corresponding parameters are automatically assigned *via* a graph based substructure search and an automated query in a relational database hosted at http://www.mofplus.org. In order to exploit this methodology also for the fu-MOFs and the flexible linkers, a similar strategy for the choice of the reference systems was used. Again, predefined parameters of small fragments like benzene rings are first assigned, such that only the remaining parameters have to be reparameterized.

Since the linker library consists of alkyl side-chains (in principle of arbitrary length), we chose to fit a butane molecule as a generic sp^3-carbon reference system, from where parameters of alkyl chains of arbitrary length can be obtained, just like benzene is used as a reference system for all aromatic carboxylate

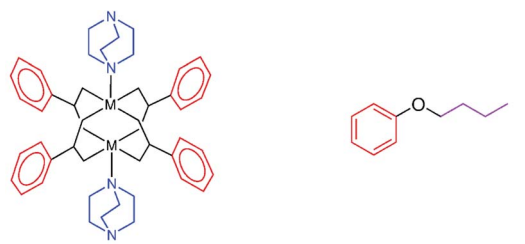

(a) Reference model for the paddle-wheel SBU.

(b) Side-chain reference model: phenyl butyl ether.

Fig. 1 Hierarchical concept behind MOF-FF: larger reference systems utilize predefined parameters from smaller reference systems. (a) For a paddle-wheel SBU (oxygen atom labels omitted for clarity) predefined parameters for benzene (red) and isolated dabco (blue) are kept and only the core (black) parameters are fitted. (b) For a reference system like phenyl butyl ether, benzene (red) and butane (magenta) parameters are kept predefined.

ART ■ D0FD00017E

linkers. In Fig. 2 all reference systems to generate parameters for the fu-MOF linkers are given in black. For side-chains smaller than the phenyl butyl ether, the systems were fitted explicitly.

In order to be consistent with the conventional MOF-FF methodology, the same DFT functional, basis set and dispersion correction were used to compute reference data for the SSH fit as well as for the *ab initio* MD simulations, to sample structure and force for the MSF fit (see ESI† for details). Each reference system shown in Fig. 2 was fully optimized in the all-*trans* configuration, the Hessian matrix of second derivatives was computed for this conformation, and then a 60.5 ps Born Oppenheimer (BO)-MD simulation was performed (50k steps at $\Delta t = 50$ atu $\approx$ 1.21 fs) at a temperature of 500 K. This relatively high temperature was chosen to ensure that also the higher energy conformers are included in the datasets generated from the BOMD simulation. In the case of the small butane reference system, additional OMD simulations at 400 K and 800 K were performed. From the computed Hessians, the normal modes of the optimized structures were computed and the six lowest were confirmed to be zero (within numerical accuracy). In addition to that, constrained optimizations were carried out, where non-hydrogen single bond torsions containing at least two side-chain atoms were constrained to values ranging between 0° and 180° in steps of 5° to obtain an energy profile along these degrees of freedom.

2.3 Force field setup

The HAPA approach relies on atom type labels being derived in a rule-based fashion from the close vicinity of an atom, and a fragment type it belongs to. Each parameter also always refers to the reference system for which it was fitted. The C_{ph}–O_{eth} bond of each reference system for example all have the same atom types of c3_c2o1@ph and o2_c2@eth, but differ in the reference system they were fitted from. HAPA is hierarchical in the sense that larger reference systems are always preferred over smaller ones, if observed in a structure whose force field is about to be assigned. That means, for say a phenyl pentyl ether, all the alkyl ether reference systems are part of it, but only the phenyl butyl parameters are assigned, because this is the largest of the reference systems. For an MOF with DP-bdc linker, consequently the parameters from the phenyl propyl ether are assigned.

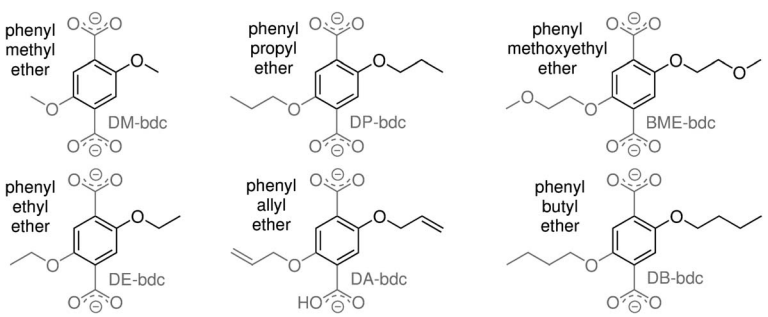

Fig. 2 The reference systems used in this work to extend MOF-FF (black) and the corresponding linkers including their abbreviations (grey). DM: di-methoxy, DE: di-ethoxy, DP: di-propoxy, DB: di-butoxy, DA: di-allyloxy, BME: bis-methoxy-ethoxy.

ART ■ D0FD00017E

This provides us with the flexibility to have unique parameters for each of the reference systems shown in Fig. 2, and thus higher accuracy, but at the same time it implies a larger set of parameters as compared to *e.g.* generic FFs like UFF.[34]

Each single bond, angle and out-of-plane bending that is distinct, based on the above atom type definition, is set up as an individual FF term whose parameters are to be fitted. Torsions in MOF-FF are described as a truncated Fourier series up to a multiplicity of four. In order to reduce the parameter space, the expansion coefficients for certain multiplicities were set to zero, depending on the atom types of the torsion to be described. For example, the aromatic torsions only need a torsion of multiplicity two for a proper description, whereas sp^3 type atoms require only multiplicity one and three. For all torsions in each reference system, not predefined by the benzene parameters, multiplicities of one, two and three were allowed to be used. For torsions terminated by hydrogen atoms (methyl rotations) only a term with multiplicity of three is used. This setting was done manually in a consistent fashion throughout the entire reference system library (for details, see http://github.com/cmc-rub/supporting_data where all FF parameters are listed).

For the coulombic interactions we kept the neutral fragment fixed charge approach of the original MOF-FF scheme together with a representation of the charge density by a single spherical Gaussian.[31] The atomic charges of the phenyl fragment are taken from the parameterized benzene as in the original MOF-FF scheme. For the organic side-chain carbon and hydrogen atoms, having only C and H as neighbors, we use a charge of $q(\mathrm{H}) = 0.06\ \mathrm{e}^{+}$ for hydrogen atoms, and $q(\mathrm{C}) = n_{\mathrm{H}} \times 0.06\ \mathrm{e}^{-}$ for carbon atoms. The remaining charges are derived from a numeric fit to match the electrostatic potential of the global energy optimum, given the already assigned charge parameters as restraints. This RESP fit was performed using the CMA-ES optimizer and the Horton code.[35,36] Charges are assigned before the fitting procedure and kept fixed in the subsequent fitting process.

2.4 Force matching

As an alternative to the SSH fit, the necessary parameters to describe the flexible side-chains were derived by an MSF fit, along the lines originally introduced by Ercolessi *et al.*[32] The aim is to determine the optimal parameter set P^* by parameterizing the potential in a way that it matches the forces supplied by first principles calculations for a large set of different configurations. For this purpose an objective function $\mathscr{L}(P)$ is minimized which measures the difference between the forces computed by the force field and those provided by the reference method by a mean square deviation (MSD). Usually this difference is measured in Cartesian space. In this work we propose a modified approach, where this is performed in a redundant internal coordinate (RIC) space defined by the systems connectivity, analogous to the usual MOF-FF parameterization strategy. First the Cartesian forces $\vec{F}$ are projected into the forces in redundant internal coordinate space $\vec{F}_q$ using Wilson's B-matrix ($B_{ij} = \dfrac{\partial q_i}{\partial x_{\mathrm{j}}}$, where q_i is an RIC, and x_{j} a Cartesian coordinate of atom j).

$$\overrightarrow{F_q} = (B^{+})^{T}\vec{F}, \tag{1}$$

ART ■ D0FD00017E

and then the objective function $\mathscr{L}_{\mathrm{FM}}$ is evaluated as

$$\mathscr{L}_{\mathrm{FM}}(P) = \frac{1}{M}\sum_{k=1}^{M}\sum_{r=1}^{Q_k} w_{kr}\left(F_{q,kr}(P) - F_{q,kr}^{\mathrm{ref}}\right)^2. \quad (2)$$

Here M is the number of molecular configurations, Q_k is the number of RICs per configuration k, w_{kr} is the weight of internal coordinate r in configuration k. The weights are chosen as in the usual SSH fit.[26] If an RIC, r, defined by its atom types occurs n_r times in the system it gets a weight of $w_r = n_r^{-1}$, but only those RICs in which at least one variable parameter is present get a non-zero weight w_{kr}. In this way exactly all those parameters connected to an FF term describing the given RIC r are included in the set of variable parameters P in a balanced way. This MSF fit setup based on the projection of the force into redundant internal coordinates enables us to specifically tune the terms of the force field which are responsible for the dynamics of the flexible side-chains while keeping the parameters on the backbone fixed. The objective function $\mathscr{L}$ was minimized using the covariance matrix evolution strategy (CMA-ES).[26,35,37] The fitting procedure is implemented in our in-house developed FFgen code.

The optimization of both the SSH fit and the MSF was run using the default population size based on the number of parameters, which for example is 15 for a 51 dimensional fit as for the phenyl ethyl ether. An initial sampling aspect ratio of 1.0 and an initial sigma of 0.1 was used for all fits. Each fit was run for 5000 generations, where the optimization was visually confirmed to have reached convergence in all cases.

2.5 Validation for butane

In order to assess the limitations of the SSH fit we first compared the FFs resulting from the two approaches for the smallest reference system butane. First, from the Hessian of the optimized all *trans* configuration the conventional SSH fit was performed. In a second step, forces were taken from 2000 random structures sampled from the 500 K BOMD simulation, and an MSF fit was performed. In order to test the quality of the two obtained force fields, the energy differences $\Delta E_i = E_i(\mathrm{DFT}) - E_i(\mathrm{FF})$ between the DFT reference and the respective FF for 2000 random structures sampled from the BOMD trajectories at 400 K, 500 K and 800 K are shown as histograms in Fig. 3a. The energies were referenced to the minimum energy structure in the BOMD simulation (Table 1).

Whereas the MSF fitted FF results in narrow error distributions, the SSH fitted force field shows a much broader distribution with a second peak at around −0.35 kcal per mol per atom and an error at least twice as large as for the MSF fitted FF. Noteworthy at the lowest temperature of 400 K is that the error distribution of the SSH fit FF still peaks close to zero, but at higher temperatures the number of structures with significant errors increases substantially. This is due to the fact that, at higher temperatures the regions of the potential energy surface further away from the all *trans* structure, considered in the SSH fit, become more and more populated.

In order to further quantify the deviations at conformations further away from the SSH reference structure we performed a series of optimizations of the butane molecule with a constrained central C–C–C–C torsion between zero and 180 degrees in steps of 5 degrees. A comparison of the resulting energies is shown in Fig. 3b.

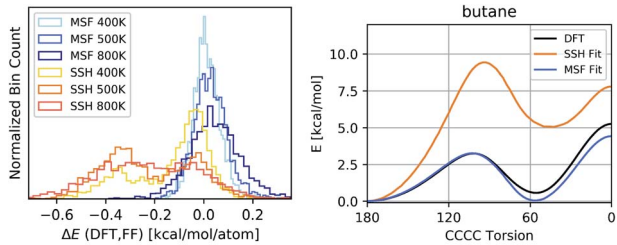

Fig. 3 (a) Errors made by the MSF and SSH fitted force fields with respect to 2000 random structures of each BOMD simulation of butane at 400 K, 500 K and 800 K. (b) C–C–C–C torsion profile of the reference system butane. The DFT energy is shown in blue, the SSH and MSF fitted FF energies are shown in orange and green, respectively.

Table 1 RMSD of the energy differences between the BOMD snapshots at a given temperature comparing DFT with the MSF fitted and SSH fitted FFs

Temperature	400 K	500 K	800 K
RMSD (ΔE^{MSF}) [kcal per mol per atom]	0.0745	0.0828	0.1124
RMSD (ΔE^{SSH}) [kcal per mol per atom]	0.1710	0.2215	0.3572

The MSF fit FF energy profile matches well with the DFT reference results, with only a slight discrepancy in the *gauche* conformation region, which is slightly over-stabilized by the force field. In contrast, the SSH fitted force field deviates notably from the DFT reference. With such a force field, alkyl chains would not be able to enter the *gauche* conformation in any real-world application run of an fu-MOF featuring longer alkyl chains.

2.6 Validation for the fu-MOF reference systems

For the phenyl-ether molecules (see Fig. 2), which served as the reference system for the fu-MOF linkers, a similar comparison between SSH and MSF fit were performed as for the simple butane. Again, the SSH fit was done for the all *trans* configuration, whereas structures sampled from a consecutive BOMD trajectory at 500 K using 2000 random structures off of a 50 ps trajectory served as the input for the MSF fit. In Fig. 4a and b, the distribution of errors of the respective FFs are compared to the energies of the DFT reference structures from the BOMD as a histogram for the case of the shortest and the longest side-chain (a complete set of figures for all systems is given in the ESI†).

For both systems the MSF fit the error peaks nicely around zero with a similar standard deviation for the short and the long chain, indicating that the remaining error most likely stems from the limitations in the potential energy expression of the FF to represent the DFT PES. In contrast, as already observed for butane, the SSH fit deviates systematically giving too high energies. As the side-chain gets longer, the SSH fitted FF gets worse.

As a further test of the two parameterization methods, we compared the torsion scans for the different dihedral angles of the reference systems. For all the parameterized systems, the C_{ph}–C_{ph}–O–C torsion energy profile (see structure in

ART ■ D0FD00017E

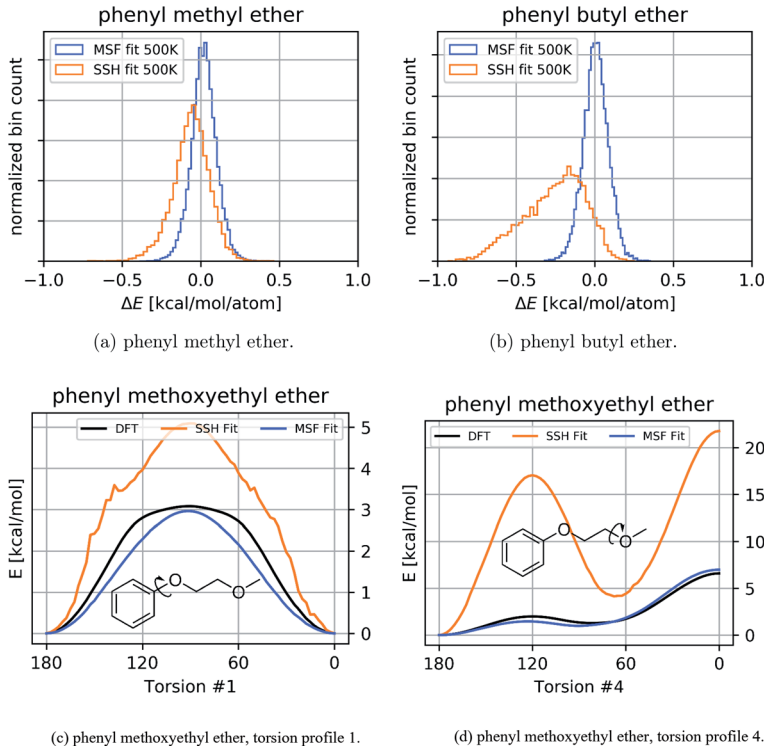

(a) phenyl methyl ether. (b) phenyl butyl ether.

(c) phenyl methoxyethyl ether, torsion profile 1. (d) phenyl methoxyethyl ether, torsion profile 4.

Fig. 4 Errors made by the SSH and MSF fitted force fields with respect to 2000 randomly selected structures of each BOMD simulation, (a) and (b); and selected torsion profiles of the phenyl methoxyethyl ether reference system comparing the two FFs with the DFT reference, (c) and (d).

Fig. 4c) is reproduced very well by the MSF fitted FF. Note, however, that the DFT energy profile does not follow a cosine curve as implied by the FF torsion energy term. As a consequence, the FF can never reproduce both curvature and energy barrier at the same time, which is the reason for the failure of the SSH fit to reproduce the barriers. Interestingly, also the SSH fit captures this particular torsion #1 qualitatively correctly, and is the best compared to the other torsions, which is due to the fact that this torsion possesses only a single barrier for a rotation between 0 and 180° (Fig. 4c). However, the FF from the SSH fits are off in this barrier by a factor of up to three, sometimes overestimating (phenyl methoxyethyl ether), sometimes underestimating (phenyl butyl ether) this barrier (see Fig. 4c and the ESI†).

As shown in Fig. 4d, for the example of the outer ether bond rotation C–C–O–C of the phenyl methoxyethyl ether reference system, the MSF fitted FFs overall show only small deviations in the respective torsion profiles, with errors in the barrier and in the relative energies of less than 1 kcal mol^{-1}. In contrast to that, the SSH fitted FF performs unsatisfactorily for all the other torsional degrees of freedom for all the investigated reference systems, where both barriers and relative energies are sometimes even qualitatively wrong.

A complete overview of the torsion profiles for all reference systems for SSH and MSF are given in the ESI.† The entire set of parameters is publicly available at http://www.github.com/cmc-rub/supporting_data/ under the index 86.

2.7 Validation for periodic fu-MOFs

In order to validate the newly derived force field for the periodic fu-MOF target structures as well, periodic DFT optimizations (including lattice parameters) were carried out for selected configurations of cp and np forms using the cp2k program, starting from the MOF-FF optimized structures. This enables us to compare both lattice parameters and energy differences. In addition, a comparison to the available experimental data can be performed, mainly provided in ref. 4 and 29. A detailed overview of the data is given in the ESI (see Table S2†), whereas herein only the main aspects are briefly discussed. It needs to be pointed out that vdW parameters have not been refitted but taken from the MM3 force field. In contrast to the previous validation steps, depending on the chosen configuration, deviations due to the accuracy of the non-bonded parameters can be quite substantial, making a comparison at this level of the periodic fu-MOF rather difficult.

Overall, the comparison of the cell parameters to experimental data is promising, because all the trends like the a/b cell parameter aspect ratio and deviations of a single angle from 90° are reproduced by the force field. A comparison to the DFT computed cell parameters shows that the op form is well reproduced, whereas the cp form has a slightly larger volume and lower density in the force field calculation. This indicates non-bonded interactions in MOF-FF that are too repulsive, and possibly also deviations due to the simplistic fixed charge model. Due to the different volumes of the cp forms, the relative op–cp energies can not readily be used for validation. In addition, they depend on the side-chain configuration and no clear trends for the op–cp energies can be observed for the static periodic DFT optimized structures (see ESI† for details). In order to compare energetics for different configurations, we compared single point energies for 100 structures sampled from one of the $NV(\sigma_a = 0)T$ trajectories at $V = 4000$ Å^3 (1000 Å^3 for one pore) for the BME system. With an average relative energy deviation below 0.046 kcal per mol per atom between DFT and MOF-FF, good accuracy is observed for a given density (Fig. S7†).

3 Breathing transition in fu-MOFs

3.1 General remarks

In our previous investigation of NCs of the unfunctionalized $Zn_2(bdc)_2(dabco)$ parent system, we observed, in contrast to the simulations constrained in PBCs, a distinct interface between the op and the cp phase moving through the system, clearly indicating first order phase transition behavior.[27] A similar but static "phase coexistence" was observed by Rogge *et al.* for similar MOFs in large PBC supercells.[28] Because of the experimental evidence that fu-MOFs with flexible side-chains behave differently in their breathing and adsorption behavior,[1,4,29,30,38] we performed similar simulations as in ref. 27, for fu-MOFs with side-chains with different lengths using the MOF-FF parameter set described in the previous section. Note that the steric bulk and the dispersive interactions of the side-

ART ■ D0FD00017E

chains force the linker phenyl moieties in the system to deviate from the in-plane arrangement with the neighboring M_2O_2C plane. Furthermore, the 2,5-functionalization of the linkers phenyl backbone allows for two different rotational configurations with a relatively high barrier as compared to the rotational degrees of freedom of the side-chains. Experimentally, there is unfortunately little evidence about the rotational conformation of the linker backbone: even at very low temperatures, the phenyl plane, and even more so the side-chains, are disordered in single crystal diffraction experiments.[29] Only for the di-pentoxy-bdc fu-MOF @ 87 kelvin, is there a crystal structure available where the side-chains are resolved and the linker orientation is not disordered any more.[39]

Due to this lack of evidence about the local conformation, the construction of computational model systems as initial configurations for the simulations poses a significant challenge, since the barrier of rotation for the linker backbone is too high to be observed frequently at ambient temperature simulations in the computationally permissible time frame of a few tenths of a nanosecond. Thus, we can not expect the system to find its free energy minimum by itself, but different areas of the PES need to be explored. As a result, we first assume a random orientation of each of the phenyl linkers and generated an initial set of random structures.

As a starting point we performed simulations in smaller supercells within PBCs in order to compare with the unfunctionalized parent system as well as to the NC simulations. For PBC simulations we can exploit the pressure tensor of the simulation box to trigger phase transitions by ramping up the pressure in an *NPT* simulation. By recording the pressure tensor in the $(NV(\sigma_a = 0)T)$ simulations along the phase transition trajectory sampled from the *NPT* simulations, where the system undergoes a transition, the hydrostatic pressure can be extracted to obtain the pV equation of state (EoS) of the given material.[40] By integrating $p(V)$, the Helmholtz free energy $\Delta A(V)$ can be obtained.

After the construction and equilibration, the open forms of the NCs with different linkers are forced to close using steered molecular dynamics (steeredMD) simulations to obtain a path from the op to the cp form of the NCs. Along all trajectories, the volume elements of each single unit cell polyhedron were calculated by keeping track of the center of mass (COM) positions of all paddlewheel units, followed by calculating the volume using a convex hull of the eight edge points.[27]

3.2 Simulations in periodic boundary conditions

Fig. 5 shows the computed pV equations of state for six different linkers investigated herein. The data for the unfunctionalized (bdc) MOF was taken from our recent investigation.[27] For DM, DE, DP, the data for one single trajectory is shown here, whereas for BME and DB, a total of 18 (BME) and eight (DB) trajectories were averaged to obtain the shown pV curves. The averaging is done because the spread of individual points $p(V)$ were observed to be very noisy in the region 950–1100 Å^3, given the $NV(\sigma_a = 0)T$ simulations started from a single pressure ramp *NPT* trajectory.

There are a couple of trends visible in the data shown in Fig. 5: whereas the position of the op form free energy minimum remains more or less constant for all the investigated linkers, the cp form increases in volume from DM to DE to DP. This trend, together with the fact that the cp forms are the free energy (ΔA)

ART ■ D0FD00017E

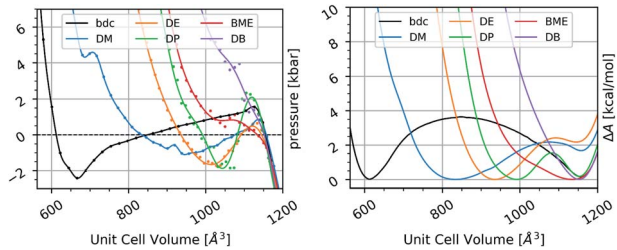

Fig. 5 (Left) pV profiles of six Zn_2(fu-bdc)$_2$(dabco) of six different linkers computed in a small periodic cell. (Right) Free energy profiles of the respective structures.

minimum, nicely reproduces the experimental finding that these MOFs in their dried form feature a narrow pore, and that the volume contraction shrinks with increasing chain length.[4] Also the tendency for the larger CO_2 pressure required to reopen the cp forms found experimentally comparing the DE and DP fu-MOF, might be caused by the larger free energy difference $\Delta\Delta A$(cp − op) of DE compared to the DP fu-MOF based on our simulations.

In BME and DB, the simulation results do not suggest the existence of a cp form any more, since only a single free energy minimum is obtained by integrating pV. This does not match the experimental observations that a closed pore form is present upon activation of these materials. However, in the BME-bdc fu-MOF there is still a shoulder present at a pore volume corresponding to a cp form. In order to elucidate this discrepancy in the prediction, we took a closer look at the individual simulations that altogether add up to the average pV and free energy profile of the BME fu-MOF in the next subsection.

3.2.1 A closeup on the BME-bdc simulations. For the BME-bdc fu-MOF a total of six different structures with a different rotational orientation of the phenyl backbone were generated. For each of them, three different initial velocities were used in the pressure ramp simulations of each of the structures in order to sample different paths from the op to the cp form given a single initial configuration. Fig. 6 shows the average pV EoS and $\Delta A(V)$ also shown in Fig. 5 as the dashed black line. The three curves for each color denote the three different trajectories for a single initial structure. Interestingly, the results for some different initial models behave differently qualitatively, but also trajectories given a single initial model differ substantially.

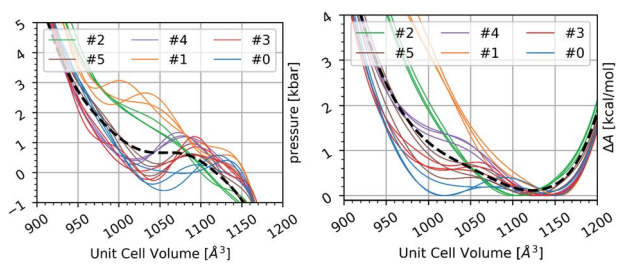

Fig. 6 Simulation results of six structures of Zn_2(BME-bdc)$_2$(dabco) (labeled as #0 to #5), each sampled three times with different initial velocities. (Left) pV Equation of state. (Right) Free energy profiles.

ART ■ D0FD00017E

The only conformers consistent with the experimental observation of a cp state at $T = 300$ K are structures #0 and #3, all the others feature only a single root in $p(V)$, which means that the simulation predicts no metastable cp form for these structures. However, given that the generated models are random with respect to the linker orientation, the results obtained here are not an exhaustive evaluation of possible configurations in this simulation cell. The relevant conclusion here is to note that different linker configurations can give rise to very distinct thermodynamic properties. We are currently working on a scheme to compute the relative free energy stabilization of such different rotational linker conformations. It remains then to be determined, as to whether the configurations sampled herein will occur in real crystallites due to their lower free energy. However, given that our force field predictions are correct, we may still conclude that real crystalline domains are likely to feature preferred orientations with some kind of short/medium range order in the side-chains, which then govern its thermodynamic properties, because the average of random configurations does not fully reproduce the experiment.

3.3 Nanocrystallite simulations

NCs of size $6 \times 6 \times 6$ were constructed in the op form, again using random initial linker orientations. After a rough optimization to remove overlapping atoms that are created occasionally during the construction process, all systems were equilibrated in an *NVT* simulation at $T = 300$ K for 100 ps.

From the last snapshots (positions and velocities) of the equilibration, steered dynamics simulations (steeredMD) were performed using the same collective variable as in our previous investigation:[27] for a $n \times n \times n$ sized crystallite, the average of n paddle-wheel centers of mass of two opposing edges of each crystallite were used as the distance collective variable to enforce a gradual phase transformation from the op to the cp form of the crystallites within 1 ns of simulation time. Snapshots from the trajectory are shown on top of the scatter plots of the same pore volume analysis in Fig. 7. Unit cell volumes averaged in the z direction with respect to the simulation time are shown in Fig. S8.†

Interestingly, the tendency for a layer by layer transformation with an interface between an op and a cp region, as was initially observed for the non-functionalized system,[27] is also observed for the fu-MOF NCs up to a chain length of three carbon atoms (DP-bdc). However, only for the DM system with the smallest chain is a distinct interface with a substantial change of the pore volume visible. For the DE system, two interfaces form during the enforced closing, with a second cp phase forming on the other side of the NC. For DP the cp volume is already much larger and the step in the volume over the interface is again smaller. Also, we see a second cp phase forming on the other side of the crystallite during the switching process. In contrast, fu-MOFs with the DB-bdc and BME-bdc linkers do not show a distinct layer-wise switch to a cp form. Instead, the entire NC converts more or less at once, with only a small tendency for certain layers, either in x or in y, to be in a narrower state as compared to its surroundings (see also Fig. S8†). This can be seen in Fig. 7, where the DB and BME systems at elevated compression levels (columns 4 and 5) feature layers which are noticeably different in V as compared to the neighboring layers. However, some remnants of the tendency to close layer-wise are also preserved for these systems with the longest

ART ■ D0FD00017E

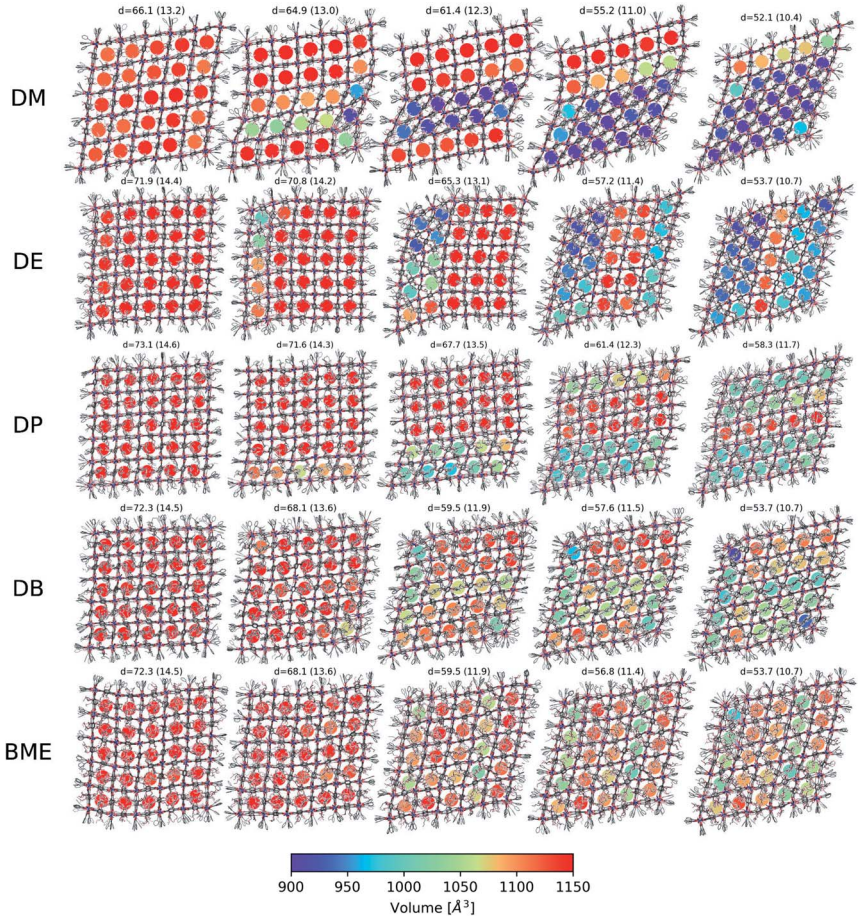

Fig. 7 Snapshots along the steeredMD trajectories overlayed on the volume analysis of the respective frame. The distance printed above is the target restraint distance (normalized per pore in brackets).

chain lengths. If one considers the volume trajectories of the DB and BME system around $t = 0.5$ ns (Fig. S8†), one can see an increase in the spread of the individual V curves as compared to the initial steps of the simulation. This has already been observed in the periodic simulations, where the pV equation of state computed for different structures, shows the largest differences in this particular unit cell volume region.

Overall, a flexible side-chain at the linker reduces the propensity to form a distinct interface between a cp and op phase with increasing length. Due to the increasing pore space used by the side-chains, the difference in volume between cp and op is not so large any more. It also needs to be noted, that the free energy barriers in the PBC simulations are smaller than for the unfunctionalized MOF (see Fig. 5), allowing for an easier transformation for the fu-MOFs. The observed tendencies can be interpreted as easier and easier "flipping" of each pore from the op to the cp state, making the interface more diffuse and broad. It should,

however, be noted that the 6 × 6 × 6 NC is still rather small, and for larger NCs one might still observe a moving interface also for the longer chain linkers. Our fu-MOFs mimic to some extent a guest molecule loaded system and indeed, also Rogge *et al.* observed more smooth phase transformation for a guest molecule loaded system in their PBC calculations with large supercells.[28] In addition to that, it also needs to be kept in mind that we observed a pronounced influence of the rotational orientation of the linkers (see Section 3.2.1 for BME) on the systems behavior. For the numerically demanding NC simulations we have currently focused on a single random oriented system.

4 Conclusion

We have successfully extended our investigations on the breathing transformation of PL-MOFs to fu-MOFs with flexible side-chains of varying length. In order to describe these specific MOFs with the numerical efficiency of a force field together with sufficient accuracy, it was necessary to extend our conventional MOF-FF global parameter fitting methodology, which is based on a single structure and Hessian (SSH) fit, by force matching using a multiple structures (MSF) approach in redundant internal coordinates. This was necessary for reference systems with multiple low energy conformations since the SSH fit was shown to perform poorly for all conformers it was not explicitly fitted for. The MSF fit requires only a relatively short BOMD simulation of small reference systems, and provides an accurate representation of the PES.

The resulting MOF-FF force field was then applied to investigate the differences in the breathing phase transition of the entire series of fu-MOFs in both small PBC simulations and aperiodic NC simulations. In the PBC simulations, for the shorter side-chains, the computed free energy profiles correctly predict the cp phase as the global free energy minimum. Several trends like the shift towards larger volumes of the cp phase with longer linkers are correctly reproduced. For the longer side-chains however, a problem arises: due to the strong sensitivity of the simulated *pV* EoS on the initial linker rotational orientations, different initial configurations resulted in qualitatively different relative free energies, with some structures showing a stable cp form and others not. An averaging of multiple random conformers was found not to be sufficient to predict the experimentally observed cp forms for these fu-MOFs. This leads to the conclusion that there is an energetically preferred orientation dominating in real systems even at room temperature. Such preferred orientations have been observed in single crystal diffraction experiments for even longer side-chains and at low temperatures (87 kelvin).[39] We are now working on a scheme to predict such preferred orientations by molecular dynamics simulations.

Finally, steeredMD simulations were performed for each linker for 6 × 6 × 6 sized NCs, enforcing an op to cp transformation. As in the parent $Zn_2(bdc)_2$(-dabco) system, the smaller side-chains exhibit phase coexistence during the compression, with a layer-wise mechanism, however, with a much less clear interface between the phases. For the longer side-chains, no clear phase coexistence or interface can be observed and the compression – at least for the still small NCs – appears to be concerted including all pores at once. A similar tendency has been reported for guest molecule loaded systems, and we conclude that flexible side-chain linkers behave similarly to loaded guest molecules and

ART ■ D0FD00017E

hamper phase coexistence, or make the phase interface more diffuse. To further unravel the atomistic mechanism of breathing phase transformation it will be necessary to study even larger NCs, but also to determine such preferential rotational linker orientations by computing their relative free energies. Despite these limitations our molecular dynamics simulations using an accurate force field allows us to study these complex cooperative phenomena on a molecular scale with unprecedented accuracy and resolution.

Conflicts of interest

There are no conflicts of interest to declare.

Acknowledgements

This work was funded by the Deutsche Forschungsgemeinschaft (DFG) by the grant (SCHM1389/10-1) within research unit FOR2433.

References

1 A. Schneemann, V. Bon, I. Schwedler, I. Senkovska, S. Kaskel and R. A. Fischer, *Chem. Soc. Rev.*, 2014, **43**, 6062–6096.
2 S. Kitagawa, R. Kitaura and S. Noro, *Angew. Chem., Int. Ed.*, 2004, **43**, 2334–2375.
3 D. N. Dybtsev, H. Chun and K. Kim, *Angew. Chem., Int. Ed.*, 2004, **43**, 5033–5036.
4 S. Henke, A. Schneemann, A. Wütscher and R. A. Fischer, *J. Am. Chem. Soc.*, 2012, **134**, 9464–9474.
5 C. Serre, F. Millange, C. Thouvenot, M. Noguès, G. Marsolier, D. Louër and G. Férey, *J. Am. Chem. Soc.*, 2002, **124**, 13519–13526.
6 T. Loiseau, C. Serre, C. Huguenard, G. Fink, F. Taulelle, M. Henry, T. Bataille and G. Férey, *Chem.–Eur. J.*, 2004, **10**, 1373–1382.
7 S. Krause, V. Bon, I. Senkovska, U. Stoeck, D. Wallacher, D. M. Többens, S. Zander, R. S. Pillai, G. Maurin, F.-X. Coudert and S. Kaskel, *Nature*, 2016, **532**, 348–352.
8 J. D. Evans, L. Bocquet and F.-X. Coudert, *Chem*, 2016, **1**, 873–886.
9 F.-X. Coudert, A. Boutin, M. Jeffroy, C. Mellot-Draznieks and A. H. Fuchs, *ChemPhysChem*, 2011, **12**, 247–258.
10 A. Sturluson, M. T. Huynh, A. R. Kaija, C. Laird, S. Yoon, F. Hou, Z. Feng, C. E. Wilmer, Y. J. Colón, Y. G. Chung, D. W. Siderius and C. M. Simon, *Mol. Simul.*, 2019, **45**, 1082–1121.
11 S. Wannapaiboon, A. Schneemann, I. Hante, M. Tu, K. Epp, A. L. Semrau, C. Sternemann, M. Paulus, S. J. Baxter, G. Kieslich and R. A. Fischer, *Nat. Commun.*, 2019, **10**, 346.
12 Y. Sakata, S. Furukawa, M. Kondo, K. Hirai, N. Horike, Y. Takashima, H. Uehara, N. Louvain, M. Meilikhov, T. Tsuruoka, S. Isoda, W. Kosaka, O. Sakata and S. Kitagawa, *Science*, 2013, **339**, 193–196.
13 S. Krause, V. Bon, I. Senkovska, D. M. Többens, D. Wallacher, R. S. Pillai, G. Maurin and S. Kaskel, *Nat. Commun.*, 2018, **9**, 1573.
14 O. Weser and V. Veryazov, *Front. Chem.*, 2017, **5**, 111.

15 J. Wieme, K. Lejaeghere, G. Kresse and V. Van Speybroeck, *Nat. Commun.*, 2018, **9**, 4899.
16 E. Cockayne, *J. Phys. Chem. C*, 2017, **121**, 4312–4317.
17 S. Bureekaew and R. Schmid, *CrystEngComm*, 2013, **15**, 1551–1562.
18 S. Bureekaew, V. Balwani, S. Amirjalayer and R. Schmid, *CrystEngComm*, 2014, **17**, 344–352.
19 M. Peksa, S. Burrekaew, R. Schmid, J. Lang and F. Stallmach, *Microporous Mesoporous Mater.*, 2015, **216**, 75–81.
20 M. Alaghemandi and R. Schmid, *J. Phys. Chem. C*, 2016, **120**, 6835–6841.
21 J. P. Dürholt, J. Keupp and R. Schmid, *Eur. J. Inorg. Chem.*, 2016, **2016**, 4517–4523.
22 R. Semino, J. P. Dürholt, R. Schmid and G. Maurin, *J. Phys. Chem. C*, 2017, **121**, 21491–21496.
23 J. Keupp and R. Schmid, *Faraday Discuss.*, 2018, **211**, 79–101.
24 S. Impeng, R. Cedeno, J. P. Dürholt, R. Schmid and S. Bureekaew, *Cryst. Growth Des.*, 2018, **18**, 2699–2706.
25 S. Siwaipram, P. A. Bopp, J.-C. Soetens, R. Schmid and S. Bureekaew, *J. Mol. Liq.*, 2019, **285**, 526–534.
26 J. P. Dürholt, G. Fraux, F.-X. Coudert and R. Schmid, *J. Chem. Theory Comput.*, 2019, **15**, 2420–2432.
27 J. Keupp and R. Schmid, *Adv. Theory Simul.*, 2019, **2**, 11.
28 S. M. J. Rogge, M. Waroquier and V. Van Speybroeck, *Nat. Commun.*, 2019, **10**, 4842.
29 S. Henke, A. Schneemann and R. A. Fischer, *Adv. Funct. Mater.*, 2013, **23**, 5990–5996.
30 A. Schneemann, E. D. Bloch, S. Henke, P. L. Llewellyn, J. R. Long and R. A. Fischer, *Chem.–Eur. J.*, 2015, **21**, 18764–18769.
31 S. Bureekaew, S. Amirjalayer, M. Tafipolsky, C. Spickermann, T. K. Roy and R. Schmid, *Phys. Status Solidi B*, 2013, **250**, 1128–1141.
32 F. Ercolessi and J. B. Adams, *Europhys. Lett.*, 1994, **26**, 583–588.
33 J. P. Dürholt, J. Keupp and R. Schmid, 2020, in preparation.
34 A. K. Rappe, C. J. Casewit, K. S. Colwell, W. A. Goddard and W. M. Skiff, *J. Am. Chem. Soc.*, 1992, **114**, 10024–10035.
35 N. Hansen, *Workshop Proceedings of the GECCO Genetic and Evolutionary Computation Conference*, 2009, p. 2389.
36 T. Verstraelen, P. Tecmer, F. Heidar-Zadeh, K. Boguslawski, M. Chan, Y. Zhao, D. K. Taewon, S. Vandenbrande, D. Yang, C. E. González-Espinoza, S. Fias, P. A. Limacher, D. Berrocal, A. Malek and P. W. Ayers, *HORTON 2.0.1*, 2015.
37 G. Shchygol, A. Yakovlev, T. Trnka, A. C. T. van Duin and T. Verstraelen, *J. Chem. Theory Comput.*, 2019, **15**, 6799–6812.
38 A. Schneemann, P. Vervoorts, I. Hante, M. Tu, S. Wannapaiboon, C. Sternemann, M. Paulus, D. F. Wieland, S. Henke and R. A. Fischer, *Chem. Mater.*, 2018, **30**, 1667–1676.
39 I. Schwedler, S. Henke, M. T. Wharmby, S. R. Bajpe, A. K. Cheetham and R. A. Fischer, *Dalton Trans.*, 2016, **45**, 4230–4241.
40 S. Rogge, L. Vanduyfhuys, A. Ghysels, M. Waroquier, T. Verstraelen, G. Maurin and V. Van Speybroeck, *J. Chem. Theory Comput.*, 2015, **11**, 5583–5597.